Plasmonic Cavities for Enhanced Spotaneous Emission

Plasmonic Cavities for Enhanced Spontaneous Emission

A dissertation presented

by

Tsung-li Liu

to

The School of Engineering and Applied Sciences

in partial fulfillment of the requirements

for the degree of

Doctor of Philosophy

in the subject of

Engineering Sciences

Harvard University

Cambridge, Massachusetts

May 2013

Dissertation advisor

Professor Evelyn L. Hu

Author

Tsung-li Liu

Plasmonic Cavities for Enhanced Spontaneous Emission

Abstract

The modification of spontaneous emission, i.e. the Purcell effect, with optical cavities has been highly studied over the past 20 years as one of the most important goals for cavity quantum electrodynamics (cQED). The recent development of using surface plasmon resonances to concentrate optical field into sub-wavelength scale further extended cQED research of into a new regime.

However, although metallic reflectors are used in some of the earliest demonstrations of cQED, the use of metals is not preferable in high Q optical cavities due to the lossy nature of metals. The presence of metals near an optical emitter also strongly alters its radiation dynamics. As a result, the development of plasmonic cavities brings not only new opportunities but also new problems and challenges. In this thesis we describe four different plasmonic cavity designs along with optical simulations and measurements on them to demonstrate: large spontaneous emission

enhancement, controlled mode tuning, and control of the plasmonic band-gap and resonances of high-Q plasmonic cavities for coupling to specific emitters.

We hope that our work can guide and inspire researchers who are moving from traditional cavity designs to novel plasmonic devices, helping them to establish design concepts, fabrication criteria, and baselines for characterizing these devices.

Table of Contents:

Publication of the work in this dissertation

The experiments results of Chapter 3 have been published as:

> Kasey J. Russell, Tsung-Li Liu, Shanying Cui and Evelyn L. Hu, "Large spontaneous emission enhancement in plasmonic nanocavities", Nature Photonics, vol 6, 459-462 (2012)

In addition, the experiment and simulation results of Chapter 4 and 5 are currently being fashioned into three papers:

> Tsung-li Liu, Kasey J. Russell, Shanying Cui and Evelyn L. Hu, "Controlled Mode Tuning in 1-D 'RIM' Plasmonic Crystal Trench Cavities Probed with Coupled Optical Emitters", In preparation.

and

> Tsung-li Liu, Kasey J. Russell, Shanying Cui and Evelyn L. Hu, "Hybird 2-D plasmonic crystal cavities", In preparation.

and

> Tsung-li Liu, Kasey J. Russell, Tina Huang, Marcus Witzany, Robert Roßbach, Michael Jetter, Peter Michler and Evelyn Hu, "Plasmonic WGM cavities for coupling to InP self-assembled quantum dots", In preparation.

These results have also been presented in conference meetings including:

> Tsung-li Liu, Shanying Cui, Kasey Russell, John Joo and Evelyn Hu, "Metallic trench resonator for enhanced spontaneous emission of nano-crystals", 2011 Materials Research Society Fall meeting in Boston, Massachusetts.

and

> Tsung-li Liu, Kasey J. Russell, Shanying Cui, John Joo and Evelyn L. Hu, "Deterministically tuned plasmonic cavities–design and fabrication", 2012 10th International Symposium on Photonic and Electromagnetic Crystal Structures in Santa Fe, New Maxico.

Acknowledgments

I wish to express my deep gratitude for all those who directly or indirectly contributed to this thesis and all the works presented in it. First and foremost, I need to thank my advisor Evelyn Hu who brought me into the field of photonics and provided me all the guidance and resources for research. Her great insights and patience helped me to go though all the hard times in my graduate research. I can deeply feel how much I am changed in a good way under her guidance. I would also like to thank my committee members, Professor Bob Westervelt, Marko Loncar and Kenneth Crozier for their great advice on this thesis.

I would like to thank my colleague Dr. Kasey Russell for his incredible passion in science. His unsatisfying curiosity encouraged and sometimes forced me into tremendous amount of discussions which lead to the birth of the thesis. I would also like to express my appreciation to Shanying Cui who participated greatly in the projects and helped me a lot. Her delightful personality amused all members of the Hu group. I also appreciate all the people who moved from Santa Barbara with me, including John, Jonathan, Alex and Fabian, especially John and Jonathan who shared so much time with me in my graduate school career.

A few collaborators must be mentioned other than the projects described in the thesis. I want to give my thanks to Nan Niu who has been a great friend and collaborator in the project of making GaN photonic devices. It is also a pleasure to work with John and Katie in the formation of ZnO photonic structures. I also need to thank the collaborators from Professor Peter Michler's group in Stuttgart, Germany. It has been a pleasure to work with both Marcus and Fabian for the fabrication of InP microdisks. I would also like to thank Harvard Center for Nanoscale Systems for all the support in fabricating and characterization of all the devices mentioned in the thesis.

As for my family, first I need to give my sincere gratitude to my mother, Chung-chiu Tien. Her unconditional love and care made me who I am. I would also like to thank my brother, Chung-shin Liu who was my first teacher in science and a great role model. Last, but not least, I must thank my wife, Yu-jung Kuo, who moved from Santa Barbara with me and has been taking care of my daily life through all the years in Harvard. This research project would not have been possible without her full-hearted support.

Dedicated to mom who made me,

and my beloved wife who completed me.

Chapter 1
Introduction

1.1 Perspective

The natural spontaneous emission properties of a material have largely governed their suitability for applications including solid state lighting, fluorescence imaging and single photon generation. Spontaneous emission, the generation of photons in a material into an excited state, and their subsequent transition to lower energy states without stimulation, has long been considered an intrinsic material property.

In 1946, Edward Mills Purcell described how the spontaneous emission rate can be modified by altering the local density of optical states around the emitter. The resulting modification has become known as the "Purcell Effect" [Ref. 1]. In this article, he discussed the use of 'optical cavities' to enhance the spontaneous emission rate of excited atoms. The enhancement achieved by perfectly aligning a sharp transition onto a cavity resonance can be expressed as:

$$F_p = \frac{3}{4\pi^2}\left(\frac{\lambda}{n}\right)^3\left(\frac{Q}{V}\right) \qquad (1\text{-}1)$$

This unit-free parameter F_p is the well-known Purcell Factor, where n is the refractive

index of the material, λ is the radiation wavelength, Q is the quality factor of the cavity mode and V is the modal volume. Aside from Q and V, most of these parameters are determined by intrinsic material characteristics. Therefore, the Q/V ratio became an important figure of merit for emission enhancement by cavities.

Let us take a closer look at these two parameters, which will play an important role through out the thesis. The quality factor Q is defined as the ratio between optical energy stored in the cavity and energy loss per-oscillation cycle. It also determines the linewidth in frequency of the resonance. A mathematical expression can be written as:

$$Q \equiv 2\pi \frac{\text{Energy stored in cavity}}{\text{Enegy dessipation per osccilation cycle}} = \frac{\omega_0}{\Delta\omega} = \frac{\lambda_0}{\Delta\lambda} \qquad (1\text{-}2)$$

where ω_0/λ_0 is resonating angular frequency/wavelength of the cavity and $\Delta\omega/\Delta\lambda$ is the line width in frequency/wavelength domain. The modal volume V, simply defined as the volume of an optical mode, can also be expressed as:

$$v \equiv \frac{\int \varepsilon |\mathrm{E(r)}|^2 \mathrm{dv}}{\varepsilon |\mathrm{E_{max}}|^2} \qquad (1\text{-}3)$$

Where E(r) is the electric field intensity at position r, ε is the dielectric constant of the material and the expression $\varepsilon|E|^2$ simply calculates the optical energy density.

Although the theory of enhancing spontaneous emission was introduced in 1940s, it was not demonstrated in cavities until 1983 when a group in France demonstrated alteration of emission life time of Rydberg atoms [Ref. 2]. The cavity used in this work is a Fabry-Perot cavity formed by two spherical niobium mirrors placed roughly 25mm to each

other. It provides a Q as high as $7.5x10^5$, but the mode volume V is also large (~$70mm^3$). Such a high V forbids significant enhancement for emission at optical frequencies.

The rapid development in solid state photonics, material growth and micro-fabrication techniques allowed people to design and fabricate high Q cavities down to micro-meter dimensions. In order to achieve a high Q/V ratio, cavities with extremely high Q and near cubic wavelength modal volume have been published, and significant radiation enhancement was also demonstrated with these devices [Ref. 3, 4]. However, fundamental limits on these two parameters started to hinder the rapid development of the field. On one hand, the quality factor Q is limited by the finite scattering produced by defects and fabrication imperfections. On the other hand, the mode volume V is limited by the diffraction limit of optical fields. Therefore, in principal one cannot concentrate an optical field into a volume much less than the cubic of the wavelength of interest.

Figure 1-1 shows estimated Q and V values for various optical resonator devices. On the top right corner are dielectric microcavities as discussed in the previous paragraph. With careful design and fabrication, an emitter-containing cavity can reach a Q of a few thousands to a millions. This high quality factor provides not only enhanced optical field intensity inside the cavities but also sharp frequency response due to the extremely narrow line width of the resonance mode. Both of these facts enabled a wide range of applications in cavity quantum electro dynamics.

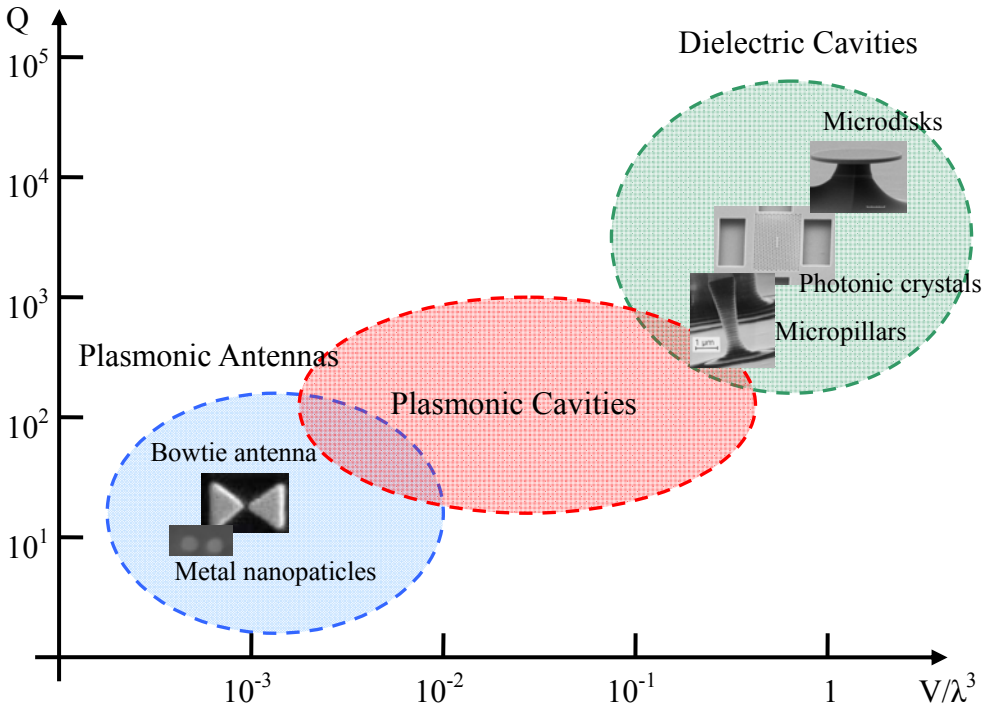

Fig. 1-1: Typical Q and V values for various kinds of optical resonators [Ref. 5-7].

However, it has been well demonstrated within the last decade that the collective resonance between photons and electrons, know as plasmon polaritons, can be concentrated beyond the diffraction limit [Ref. 8]. Sub-wavelength plasmonic cavities, antennas and waveguides have been demonstrated. These works opened up the possibility to break the fundamental limit of mode volume in nano-cavities, hence achieve higher radiative enhancement.

These nano-antennas have the ability to concentrate optical field into a volume as small as 10^{-3} $(\lambda)^3$, hence provide strongly enhanced light-matter interaction at the field

maximum [Ref. 9, 10]. However, the lossy nature of the metal eliminates the possibility for forming extremely high Q plasmonic cavities. Therefore, instead of being designed to confine the fields for a long time, these resonators are usually designed to couple well with radiation modes so they can either concentrate incident fields into a small spot or guide emission from molecules in the device to free space radiation. They usually have relative low Q (<10), as shown in the bottom left corner of Figure 1-1. The fact that the Q is so low for these antennas allows broad band emission enhancement but at the cost of their frequency selectivity.

Besides the great development in both high Q dielectric cavities and low Q plasmonic antennas, there is still a wide area in between the two corners in Figure 1-1. This area denotes plasmonic resonators with slightly higher Q than those antennas but still keep the capability of concentrate optical field into sub-wavelength dimensions. These devices, named plasmonic cavities in Figure 1-1, are designed to aim for Q in the order of tens to hundreds. These numbers provides resonances with band width of a few to tens of nanometers. This ensures sufficient spectral selectivity for emitters with emission line width of the same order. Besides, exploring into this range gives us freedom to combine the properties of plasmon polaritons with various cavity designs to achieve higher spontaneous emission enhancement.

1.2 Focus of the Thesis

The focus of this thesis explores ways to achieve and demonstrate large spontaneous emission enhancement using plasmonic nanocavities. Several important aspects are described, such as: (1) characteristics of surface plasmon polaritons, (2) theoretical and experimental demonstration of radiative enhancement in plasmonic cavities and (3) the design and fabrication of metallic structures as well as hybrid metal-dielectric structures which allow well controlled plasmonic resonances. All of these studies serve to enhance our understanding and guide the design of these metallic structures to manipulate the interaction between plasmonic cavities and embedded emitters.

As described in the first section, these plasmonic cavities allow us to combine the advantages of surface plasmon polaritons while incorporating the well developed design criteria and fabrication techniques for dielectric cavities. One important goal of this work is to highlight the differences and similarities between plasmonic devices and dielectric cavities. Therefore, this thesis is written in a way to guide and inspire researchers who are moving from traditional cavity designs to novel plasmonic devices, helping them to set up design concepts, fabrication criteria and baselines for characterizing these devices.

1.3 Organization

Chapter 2 will be an introduction to theoretical explanation of the research, including

spontaneous emission enhancement, characteristics of surface plasmon polaritons and the complex interaction between metallic structures and emitters. Conceptual descriptions along with limited mathematical expressions will be demonstrated and set up for later chapters.

Chapter 3 shows an experimental demonstration of spontaneous emission enhancement with a silver nanowire plasmonic gap mode cavity. This clever design created by my colleague Dr. Kasey Russell takes advantage of the atomically smooth side walls of chemically synthesized silver nanowires [Ref. 11]. With such a platform, we are able to characterize the emission property of the organic dye embedded within the cavity. This work addresses the difference between emitter dynamics near lossy metallic materials and lossless dielectrics.

Chapter 4 presents designs and fabrication methods for lithographically defined plasmonic trench cavities. These devices provide us precise control over the spatial position and spectral response. Both of these properties are important for manipulating light-mater interactions. Two fabrication method: focused ion beam (FIB) milling and reversed image mold (RIM) were applied to fabricate metallic trenches with width variations. Capabilities and limitations of these fabrication techniques will be compared. Finally, simulations and optical properties of the trench cavities will be discussed.

In Chapter 5, we demonstrate works on hybridizing photonic modes in dielectric

cavities to surface plasmon polaritons. In these works, two hybrid geometries are discussed: first, the coupling of metallic surfaces onto photonic band-gap in dielectric photonic crystals, and second, the coupling of whispering gallery modes (WGM) of semiconductor microdisks to a surrounding silver layer. . The first work presents how plasmonic band-gap can be created by combining dielectric photonic crystals and a metal surface. Design ideas on plasmonic band-gap devices will be discussed. In the second work, we demonstrate coupling epitaxial self-assembled quantum dots (SAQDs) with both dielectric and plasmonic cavities [Ref. 12]. Characteristics of SAQDs and how to couple these emitters to plasmonic modes will be discussed. The whole work will be concluded in Chapter 6 with outlooks for future work in this area.

Chapter 2
Emitter Dynamics in Metallic Structures

2.1 Introduction

Before a detailed discussion on the design, fabrication and measurements of plasmonic cavities, we must first have a fundamental understanding on how radiation properties of emitters can be modified in metallic structures.

Following the introduction of Purcell effect in Chapter 1, a simple, conceptual picture of how a cavity can influence emitter properties will first be provided in Section 2.2. However, this model is not sufficient to explain emitter dynamics in nanometer-scaled metallic cavities owing to the strong near-field coupling between emitter and the metallic surfaces at such a close distance.

Therefore, these near-field effects, including the generation of surface plasmon polaritons and metal-caused quenching, will be discussed in Section 2.3 and 2.4. A reflectivity-based model will be introduced in Section 2.4 to calculate the relative transition rates of each mechanism.

How these effects could affect measurement results in real devices will be discussed

in Section 2.5 as a summary to Section 2.2-4. These background concepts are introduced to prepare one for better understanding of the experiment design and measurement results demonstrated in following chapters.

2.2 Emission Enhancement in Optical Cavities

As discussed in the previous chapter, emitting characteristics of a dipole can be modified and controlled when placed within an appropriately matched optical cavity. Although spontaneous emission cannot be fully described using classical physics, there is a decent model in classical picture to understand the modification of spontaneous emission rate in a cavity.

The emission rate of an excited two level system, described as an electrical dipole, can be estimated as the power consumption of an oscillating charge under an external electric field. In a homogeneous material, this external field is provided by the vacuum fluctuation energy of photon states near the dipole.

As the dipole approaches a reflective interface, the radiation from the dipole may be reflected back and interact with the dipole itself, as shown in Figure 2-1 (a) and (b). The modification of the dipole radiation rate by this self-interaction can be calculated as the energy dissipation rate due to this external electric field. This rate can be estimated by the inner product of the reflected field and the displacement current due to charge oscillation of

the dipole.

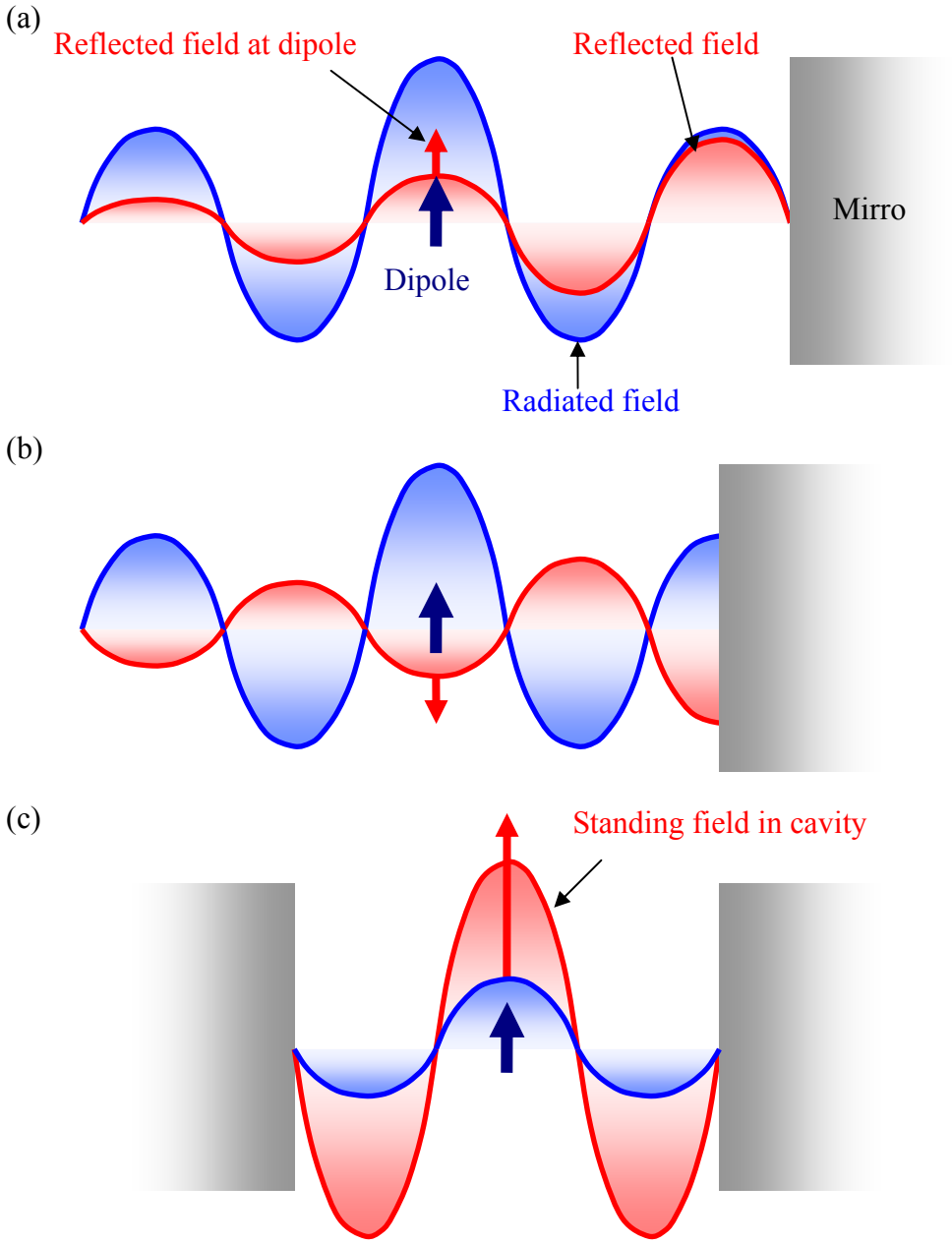

Fig. 2-1: Schematic of how a dipole source interacts with mirrors nearby. (a) When the distance between the dipole of the mirror produces constructive interference. (b) The distance produces destructive interference. (c) The dipole is located in a cavity formed by two mirrors.

In this model, the distance between the dipole and the mirror is critical. As the radiated wave gets reflected and comes back to the dipole, it experiences a phase delay due to the wave traveling time and phase shift during reflection. This reflected radiation will accelerate power consumption of the dipole only if the dot product of the electric field of the radiation and the displacement current of the dipole is positive. Under this condition, there is enhancement of radiation rate of the dipole. On the other hand, as the local electric field oscillates out of phase with the dipole current, the radiation may be suppressed. These effects have been well studied by K. H. Drexhage in 1970 [Ref. 13]. In the work, a layer of europium dibenzoylmethane complex is placed in front of a silver mirror with a well controlled distance as the variable. This europium complex radiates at 612nm with high internal quantum efficiency while in bulk. The radiation life time, which is the inverse of the radiation rate, was measured for various emitter-mirror distances.

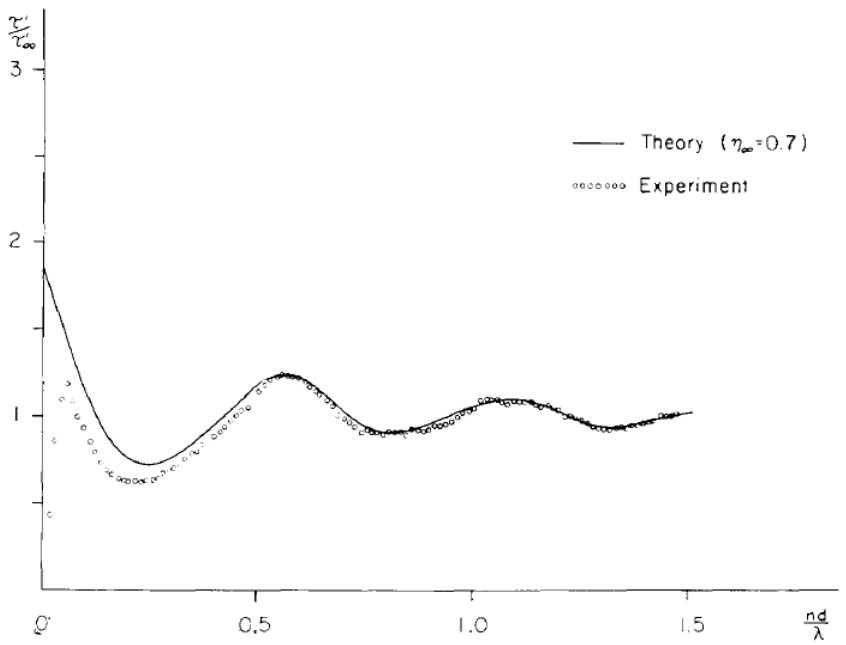

Fig. 2-2: Experimental data and calculated change of the europium complex emission lifetime at different separation to a silver mirror. The lifetime is normalized to the emission lifetime with out the silver mirror [Ref. 13]. (Use of figure permitted by Karl H. Drexhage.)

Figure 2-2 shows the calculated and measured emitter lifetime change of the europium complex vs. separation from a silver mirror. Three important features can be extracted from the data. First, the oscillations on the curve are due to the interference effect introduced in the previous paragraph. Second, this effect becomes weaker and weaker as the distance increases. This could be explained by the reduced radiation intensity farther away from the source. The last feature is the discrepancy between theoretical calculation and experimental data when the Europium complex is very close to the metal surface. This

failure of the radiation model is due to the excitation of a surface plasmon polariton and the induced intra-band transition of the metal. Details of these effects will be discussed in Section 2.3 and 2.4.

As shown in the previous paragraph, the radiation field decays with distance away from the source, which implies that this reflected field intensity can never exceed the field radiated by the dipole. However, this limit can be broken if we introduce another reflector into this system, as shown in Figure 2-1 (c). In this geometry, photons propagating along the axis perpendicular to the mirror pair can be trapped between the mirrors and set up a standing wave, when the round trip distance of the photon is equal to an integer number of wavelengths. The average electric field intensity inside the cavity (I_{ave}) is:

$$I_{ave} = \frac{1+R}{1-R} I_i \tag{2-1}$$

where R is the reflected power from the mirrors and I_i is the intensity of the initial wave [Ref. 14]. This structure now becomes an optical cavity which traps light in between the two mirrors. This kind of 1-D cavity consisting of two opposite reflecting surfaces is a Fabry-Perot cavity. We can then apply the definition of Q for cavities for this structure as:

$$Q \equiv 2\pi \frac{\text{Energy stored in cavity}}{\text{Enegy dessipation per osccilation cycle}} = 2\pi \frac{I_{ave}}{I_{ave}(1-R)/l/c} = \frac{2\pi}{c}\frac{l}{(1-R)} \tag{2-2}$$

where l is the length of the 1D Fabry-Perot cavity. We can then express the field intensity in the cavity as:

$$I_{ave} = \frac{1+R}{1-R} I_i \propto \frac{1}{1-R} = \frac{c}{2\pi} \frac{Q}{l} \propto \frac{Q}{l} \qquad (2\text{-}3).$$

As a result, the radiation rate of the emitter can be greatly enhanced in a high Q and small volume cavity, as described by Purcell's factor discussed in Chapter 1. This model provides a classical picture of this enhancement. In fact, in a quantum picture, the external field is not from radiation of the dipole but from the zero point oscillation of photonic states near the dipole. The field enhancement describe above is equivalent to the increase of the local photon density of states at the resonant frequency.

2.3 Surface Plasmon Polaritons

Metals have been applied to make optical reflectors for centuries. However, these reflective materials have not been materials of choice for photonic devices. A major difference between metals and dielectrics is that the free electron density in metals is much higher than in dielectrics. These free electrons can respond to and screen external electric fields very effectively hence, preclude the penetration of fields into the metal. This is why most metals are good reflectors of light. However, there is always finite energy dissipation during the reflection process due to the finite conductance of metals. This small amount of dissipation is negligible when you are using a silver mirror to look at yourself, but it can play a critical role when you are trying to confine optical energy for thousands of round trips of the beam.

However, under certain condition, which will be discussed later in this section, an oscillating electric field carried by photons can excite and strongly interact with the collective oscillation of electrons near surface of metals. A different type of excitation, named a surface plasmon polariton, can be generated. Like photons, these excitations can be described as electromagnetic waves propagating along the metal surface and can be characterized by their wave number (momentum) and frequency (energy). Unlike photons, these particles are tightly bound to the metal surface and the field can be concentrated into a volume much smaller than cubic wavelength if the metal is shaped in the right way. This opens up a new research field to engineer light at sub-wavelength scales.

To quantitatively understand properties of surface plasmon polariton, we need to first quantify the optical response of metals. This can be well described with Drude's model [Ref. 15] (See appendix A).

For a non-magnetic material, the optical properties are mostly described by the complex dielectric constant. The dielectric constant of a Drude metal (ideal metal described by free electron model) for optical frequencies can be expressed as:

$$\varepsilon_r(\omega) = 1 - \frac{\omega_p^2}{\omega^2} + i\frac{\omega_p^2 \frac{1}{\tau_e}}{\omega^3} \text{; where } \omega_p^2 = \frac{ne^2}{m_e} \qquad (2\text{-}4).$$

Equation 2-4 describes a material with strong frequency-dependent dielectric constant. When the frequency is lower than the plasma frequency, real part of the dielectric constant is negative and electromagnetic waves cannot propagate in the material. The plasmonic

frequency for most metals lie in ultraviolet or short wavelength visible region. That's why most metals look reflective and shiny.

The optical properties of a Drude metal are basically defined by two parameters: the plasma frequency (ω_p) and the electron damping rate ($1/\tau_e$). The plasma frequency determines the highest frequency the free electrons in a metal can respond to, and the damping rate determines how lossy the metal is. Table 2-1 shows these two parameters of some metals. The low damping rate and high material stability are reasons why most plasmonic resonators in the optical region are made with noble metals like silver or gold. Since an inter-band transition in gold makes it absorptive for blue light (that's why it looks "golden"), all the devices demonstrated in this thesis are made with silver for their outstanding properties in the visible spectrum.

Table 2-1: Drude model optical parameters for some metals [Ref. 16]

Material	Ag	Al	Au	Cu	Pt
Plasma frequency (PHz)	2.18	3.57	2.18	1.911	1.24
Damping rate (THz)	4.35	19.79	6.46	8.34	16.73

Now, for frequencies lower than the plasmonic frequency, we can start to describe the metal surface as an interface between materials with positive and negative permittivity and

try to solve for propagating modes along the surface [Ref. 17].

In order for the surface electromagnetic wave to be bounded at the interface, the wave-vector normal to the interface in both materials must be imaginary to prevent the energy from leaving the interface. Field components of such an interface wave in transverse-magnetic polarization are shown in Figure 2-3. Note that the TM polarization is the only possible orientation for surface plasmon polaritons. The reason will be demonstrated later in this section.

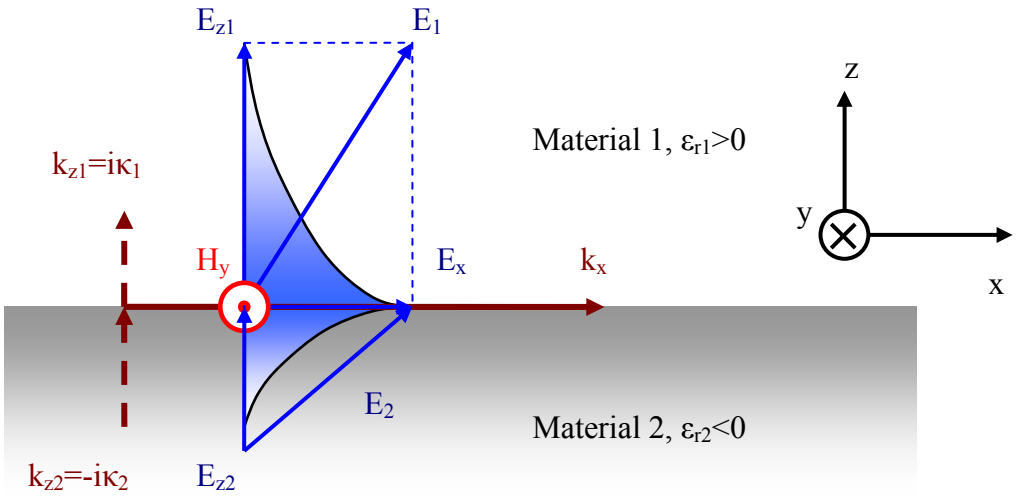

Fig. 2-3: Field and wave-vector components of surface plasmon polaritons.

As mentioned in the previous paragraph, to assure confinement at the interface, the z component of the wave vectors in both materials must be imaginary. We can then define:

$$k_{z1} = i\kappa_1 \text{; and } k_{z2} = -i\kappa_2 \qquad (2\text{-}5)$$

where κ_i is the decay constant in material i. A minus sign is applied only in material 2 to ensure the wave decays away from the interface with a real and positive κ. The fields share the same wave vector in the x direction to ensure phase matching between the two sides.

To satisfy boundary conditions at the interface, the tangential components on each side must be the same. This is why the x component of both E_1 and E_2 share the same value, labeled E_x in the figure, and similarly for the H_y component. Another boundary condition we should use is that the electric flux density perpendicular to the interface must be continuous, that is:

$$\varepsilon_{r1} E_{z1} = \varepsilon_{r2} E_{z2} \qquad \text{(2-6).}$$

The two boundary conditions can then be connected with the Gauss' Law:

$$\nabla \cdot \vec{E} = 0 \quad \text{for a charge neutral system} \qquad \text{(2-7)}$$

Then we get:

$$i\kappa_1 E_{z1} = k_x E_x = -i\kappa_2 E_{z2} \qquad \text{(2-8).}$$

Combining equation 2-6 and 2-8 results in:

$$\frac{\kappa_1}{\varepsilon_{r1}} = -\frac{\kappa_2}{\varepsilon_{r2}} \qquad \text{(2-9).}$$

The equation above explains why this kind of bounded wave occurs only at metal-dielectric interfaces. (Exceptions can happen if one can generate enough free carriers in a non-metallic material and choose a frequency that results in a negative dielectric constant [Ref. 18]). The same observation also explains why the surface plasmon polariton

only exists in TM polarization. If we try to do the same derivation with TE polarization, the dielectric constants will be replaced with relative permeabilities. We will need materials with positive and negative permeabilities to make the solution possible.

To solve for the dispersion relation of such a surface wave, we can then link the propagation constant ($\beta = k_x$) with the decay constants in equation 2-5 as:

$\varepsilon_{ri} k_0^2 = \beta^2 - \kappa_i^2$; where $k_0 = \omega\sqrt{\varepsilon_0 \mu_0}$ is the free space wave-number (2-10).

Combining equation 2-9 and 2-10 results in the dispersion relation of a surface plasmon polariton at a single metal-dielectric interface as:

$$\beta = k_0 \sqrt{\frac{\varepsilon_{r1}\varepsilon_{r2}}{\varepsilon_{r1} + \varepsilon_{r2}}} \quad (2\text{-}11).$$

There are several consequences of this relation. First, the propagation constant is real only when $\varepsilon_{r1} + \varepsilon_{r2} < 0$. There exists a pole when $\varepsilon_{r1} = -\varepsilon_{r2}$. Under this condition, the propagation constant approaches infinity and the wavelength approaches zero. The field is extremely concentrated and the speed of the wave is very slow. This is called a surface plasmon resonance. In real materials, owing to the finite imaginary part of the dielectric constant of metals, this number does not approach infinity but can significantly increase near this condition.

The second important message is that while ε_{r1} and ε_{r2} have opposite signs, the propagation constant is always larger than the free space wave-number in the dielectric material. Therefore we cannot generate surface plasmon polaritons directly with free space

radiation. There are many clever ways of generating surface plasmon polaritons from traveling waves [Ref. 19, 20]. In this thesis, we discuss how to enhance generation of surface plasmon polaritons with coupled to emitters. Therefore, coupling with free space radiation will not be discussed.

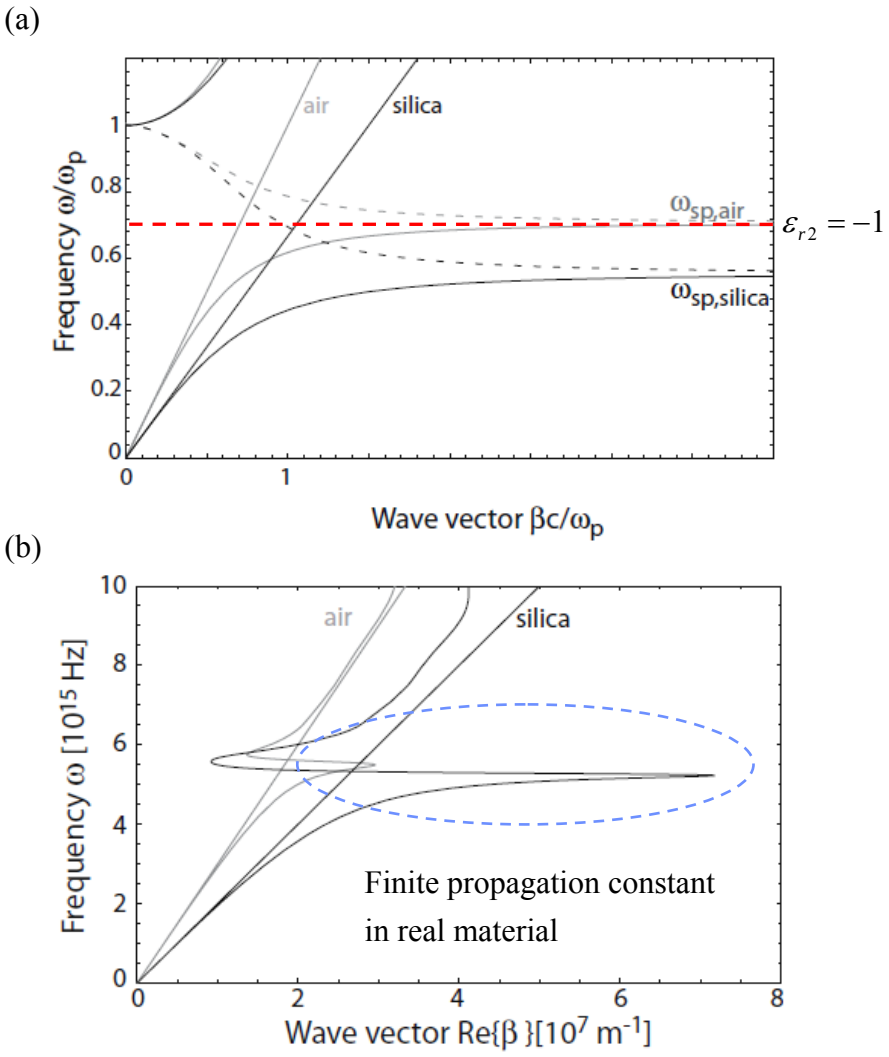

Fig. 2-4: Dispersion relation of surface plasmon polariton at the interface between (a) a perfect Drude metal and air (gray curves)/silica (black curves) and (b) silver/air (gray curves) and silver/silica (black curves). Straight lines display the light lines [Ref. 17] (Use of figures permitted by Stefan A. Maier).

Figure 2-4 shows the calculated dispersion relation for surface plasmon polaritons for both an ideal Drude metal and silver. The surface plasmon resonance condition is labeled in the figure. In Figure 2-4, it is clear that near the surface plasmon resonance frequency, the propagation constant is significantly larger than the wave-number in pure dielectrics. According to equation 2-10, this results in large decay constants and the field decays rapidly, away from the interface. This is when the field is highly concentrated at the interface. However, as the operating frequency decreases, the dispersion curve quickly approaches the light line and the decay constants decrease. The maximum of the electric field intensity drops and the highest possible emission enhancement also decreases. Much research has been carried out to demonstrate improved field concentration near a metal surface at frequencies not at surface plasmon resonances. Some work utilizes shaping the metal into nano-structures [Ref. 21]. Others applied various layers structures. [Ref. 22] Plasmonic cavities introduced in this thesis also serve the same purposes.

2.4 Emitter Dynamics near a Metal Surface

In Section 2.2, we discussed how the transition rate of an emitter can be altered near a metal surface. However, the mechanism introduced in Section 2.2 failed to explain the fast decay rate increase when the emitter is very close to the mirror ($nd/\lambda<0.1$ in Figure 2-2).

The major reason for the discrepancy is that the model used in K.H. Drexhage's work considered only a traveling wave reflected from the metal surface but ignored the evanescent coupling between the dipole and the mirror. The discussion of surface plasmon polaritons introduced in Section 2.3 provides a natural way to describe coupling to evanescent fields. These evanescent waves decay exponentially normal to the reflective surface so the coupling is significant only at very small emitter-metal separation.

In this section, a reflectivity based model considering all wave components will be introduced to provide more physical insights on the emitter dynamics near a metal surface. This method is first derived by R.R. Chance, A. Prock and R. Silbey in 1978 [Ref. 23] and wrapped up for varies metallic structures with non-local response of metals included by G.W. Ford and W.H. Weber in 1984 [Ref. 24]. Basic idea of the modeled geometry is shown in Figure 2-5.

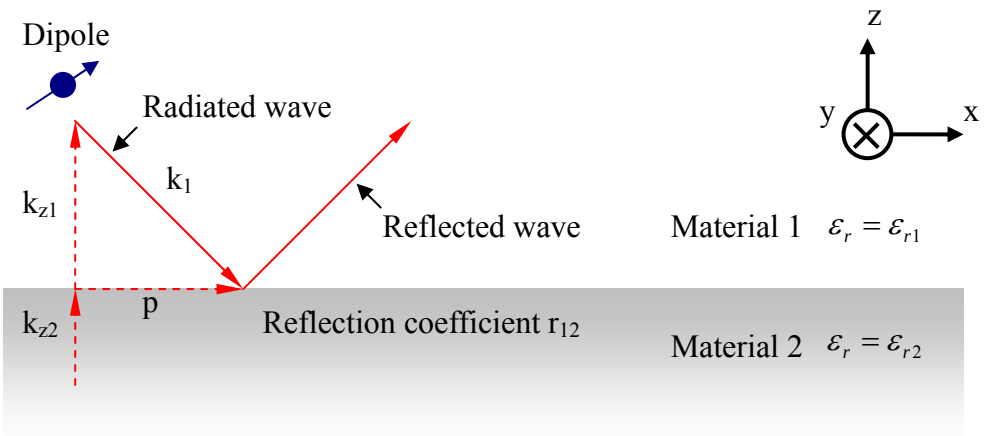

Fig. 2-5: Definition of the wave components used in calculation in this section.

The reflective coefficients, either in TE or TM polarization, can be calculated by the well-know Fresnel equations as:

$$r_{12}^{TE} = \frac{k_{z1} - k_{z2}}{k_{z1} + k_{z2}};\ r_{12}^{TM} = \frac{\varepsilon_{r2} k_{z1} - \varepsilon_{r1} k_{z2}}{\varepsilon_{r2} k_{z1} + \varepsilon_{r1} k_{z2}} \tag{2-12}$$

where k_{ij} denotes amplitudes of wave-vectors in i direction in material j. Similar to our discussion in Section 2.3, all the wave-vector lengths in z direction can be expressed by the length of in-plane wave-vector as:

$$k_{zi} = \sqrt{\frac{\varepsilon_{ri}\omega^2}{c^2} - k_x^2} \tag{2-13}$$

where ω is the angular frequency and c is the speed of light. We can express the field intensity for both polarizations with the reflectivity derived in equation 2-12. For example, the fields for TE polarization have the form:

$$\vec{E}(r) = \vec{E}_s \exp(i\vec{p}\cdot\vec{\rho})(\hat{z}\times\hat{p})\begin{cases} \exp(-ik_{z1}z) + r_{12}^{TE}\exp(ik_{z1}z) & z > 0 \\ t_{12}^{TE}\exp(-ik_{z2}z) & z < 0 \end{cases} \tag{2-14}$$

$$\vec{B}(r) = \frac{c}{\omega}\vec{E}_s \exp(i\vec{p}\cdot\vec{\rho})\begin{cases} (k_{z1}\hat{p} + p\hat{z})\exp(-ik_{z1}z) + (-k_{z1}\hat{p} + p\hat{z})r_{12}^{TE}\exp(ik_{z1}z) & z > 0 \\ (k_{z2}\hat{p} + p\hat{z})t_{12}^{TE}\exp(-ik_{z2}z) & z < 0 \end{cases} \tag{2-15}$$

where $\vec{\rho} = \vec{r} - \vec{z}$ and the in-plane wave-vector is generalized to be $\vec{p}$ instead of $\vec{k}_x$. Similar expressions can be created for Tm polarization.

In these expressions, there are only two unknowns. One is the in-plane wave-number p, which serves as a variable in following calculations. The other one is the source electric

field E_s. In order to find an expression for the source field, we have to use the radiation pattern of a dipole.

Consider a point dipole with dipole moment $\vec{\mu}$ placed at z=d oscillating with an angular frequency ω. The downward radiation form this current source can be expressed as:

$$\vec{E}_{dipole}(r) = \frac{i}{2\pi\varepsilon_{r1}} \int d\vec{p} \frac{\exp(i\vec{p}\cdot\vec{\rho})}{k_{z1}} \{(\vec{p}\hat{z} + k_{z1}\hat{p})\cdot\vec{\mu}(\vec{p}\hat{z} + k_{z1}\hat{p}) + k_1^2 \hat{z}\times(\vec{p}\cdot\vec{\mu})\hat{z}\times\vec{p}\}\exp(-ik_{z1}(z-d)) \quad (2\text{-}16).$$

Combine equation 2-35 with 2-33, the total field induced by the dipole is now:

$$\vec{E}_{total}(r) = \frac{i}{2\pi\varepsilon_{r1}} \int d\vec{p} \frac{\exp[i(\vec{p}\cdot\vec{\rho} + k_{z1}d)]}{k_{z1}} \{\vec{\mu}\cdot(\vec{p}\hat{z} + k_{z1}\hat{p})[(\vec{p}\hat{z} + k_{z1}\hat{p})\exp(-ik_{z1}z)$$

$$+ (\vec{p}\hat{z} - k_{z1}\hat{p}) r_{12}^{TM} \exp(ik_{z1}z)] + k_1^2(\vec{\mu}\cdot\hat{z}\times\vec{p})\hat{z}\times\vec{p}[\exp(-ik_{z1}z) + r_{12}^{TE}\exp(-ik_{z1}z)]\} \quad (2\text{-}17).$$

Our ultimate goal for this calculation is to determine the power dissipation of the dipole, which can be found as:

$$\mathrm{P} = \frac{\omega}{2}\mathrm{Im}(\vec{\mu}^* \cdot \vec{E}) \quad (2\text{-}18).$$

Using the electric field derived in equation 2-36 and integral all directions of $\vec{p}$, we get:

$$\mathrm{P} = \frac{\omega}{2\varepsilon_{r1}}\mathrm{Re}\int dp \frac{p}{k_{z1}} \{\mu_\perp^2 p^2[1 + r_{12}^{TM}\exp(2ik_{z1}d)] + \frac{1}{2}\mu_{//}^2 k_1^2[1 + r_{12}^{TE}\exp(2ik_{z1}d)]$$

$$+ \frac{1}{2}\mu_{//}^2 k_{z1}^2[1 - r_{12}^{TM}\exp(2ik_{z1}d)]\} \quad (2\text{-}19)$$

where $\mu_\perp$ and $\mu_{//}$ are components of $\vec{\mu}$ perpendicular and parallel to the interface. Equation 2-19 calculates the total power dissipation of the dipole near an interface. However, more physics insight could be demonstrated if we don't integrate over all

in-plane wave-numbers (p) but plot the power density versus p instead.

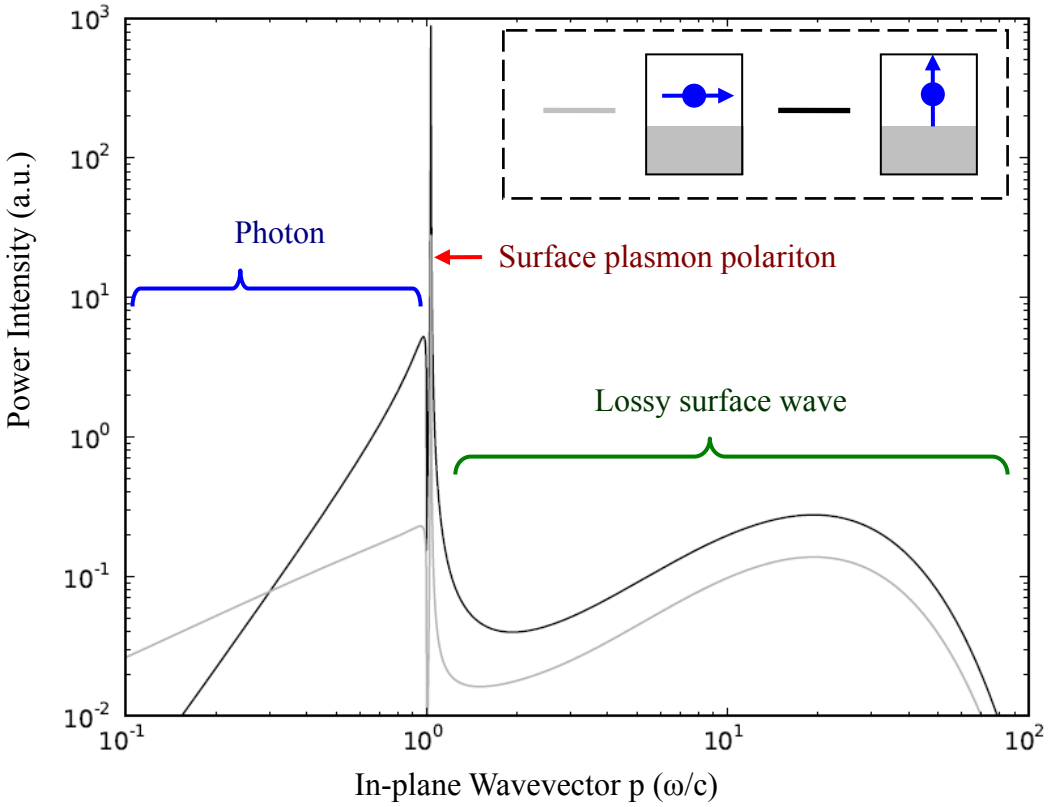

Fig. 2-6: Calculated power dissipation versus in-plane wave-number p of dipoles in air, emitting at 613nm, located 5nm away from a silver surface. The black curve is from a dipole oriented perpendicular to the metal surface; the gray curve is from a parallel-oriented dipole.

Figure 2-6 is an example of the power spectrum with a dipole located 5nm away from a silver/air interface emitting at 613nm in wavelength. The two curves stand for dipoles polarized horizontally (gray curve) and perpendicularly (black curve) to the metal surface.

We can divide the curves into three sections. The first one is the region with an in-plane wave-vector shorter than the free space wave-vector (labeled as photon in figure). In this region the energy is radiated as traveling photons. The difference in these two curves in this region is mostly due to the difference in radiation direction of the two dipole orientation.

The radiation into free space becomes evanescent hence contributes to no energy consumption once p surpasses the free space wave-number. Soon after that, a strong peak shows up in the curve, denoting coupling to surface plasmons. The peak is centered at the surface plasmon polariton propagation constant derived in equation 2-11. The finite width of the peak is from propagation loss of the mode. The longer the propagation length of the surface plasmon polariton, the sharper the peak is. The peak height of the black curve is over an order of magnitude higher than the gray curve. This is because the polarization of the surface plasmon polariton has a higher projection onto the perpendicular direction. Beyond the surface plasmon polariton propagation constant, there is still finite power dissipation into high wave-number components. At this regime, the radiated energy has very short wavelength and cannot propagate for long distances. This is called a “lossy surface wave” which is due to the electrons in the metal oscillating under the influence of the dipole. The power dissipation is due to the resistive loss during electron motion [Ref. 25]. This is a quenching effect that results in no far field radiation. Evanescent coupling at such a high wave-number regime decays quickly for very short distances. Therefore, this is

a short range phenomenon and can substantially decrease the internal quantum efficiency when we bring the dipole very close to the metal surface.

The last concept we want to mention in the section is the non-local response of metals. Unlike dielectrics, electrons in metals can move for longer distances while responding to an external field. Therefore, the presence of the material boundary can affect motion of electrons and hence change the optical properties of metals.

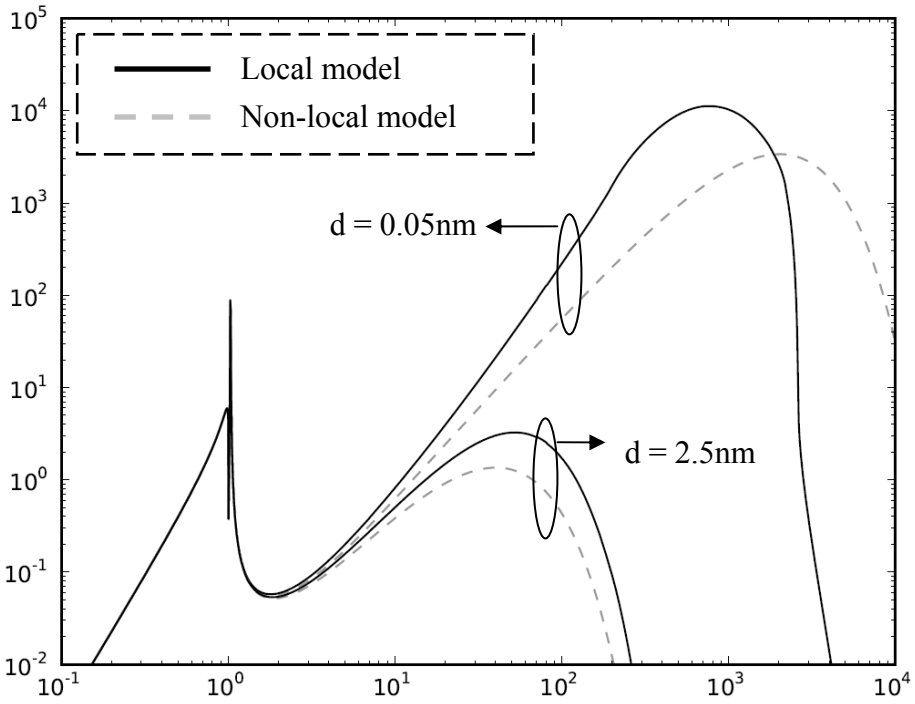

Fig. 2-7: Power dissipation versus in-plane wave-number p of dipoles near silver surfaces calculated with local and non-local models.

Figure 2-7 shows the power spectrum for dipoles 0.5Å and 2.5nm away from a silver

surface calculated for a local and non-local model. Comparing local to non-local models (gray to black curves), it is obvious that the local model underestimates metal quenching rates. This is because the model fails to consider extra electron scattering by the surface. The calculation also demonstrates how metal quenching effects can become much stronger at very short distances, as described in previous paragraphs.

In calculations we used for the work presented in Chapter 3, the non-local response of silver was included. The method we adapted from Ford and Weber [Ref. 24] applies only to planar metal surfaces. Formulations for various geometries have been studied and can be used for more complicated metallic nano-structure [Ref. 26].

2.5 Measurements of Emitters in Optical Cavities

In the previous sections, theoretical calculations of interactions between dipoles and metallic structures were presented. In this section, we will take a more careful look at how we can make experimental observations of a system with a more realistic emitter or emitter ensembles in a lossy cavity.

When a multi-level system (an atom, a molecule, a bulk material or a semiconductor quantum structure) is excited into a higher energy state, there are many ways that this system can release the excess energy and return to its ground state. If the energy difference is emitted as photons or surface plasmon polaritons in a plasmonic cavity, this process is

called a radiative transition. The radiative transition rate (ν_r) can be influenced by an optical cavity in the manner described in Section 2.2. However, sometimes the emitter undergoes a transition and loses the energy without generating photons. This is called a nonradiative transition which includes generation of phonons (heat), energy transfer to nearby sites (defects or similar emitters) and metal-caused quenching effects as introduced in Section 2.4. We can also define a nonradiative transition rate (ν_{nr}), which is the summation of the transition rates of all possible nonradiative channels.

To characterize the emission properties of an emitter, a few important parameters should be considered. The first one is the radiative emission rate, ν_r, as noted above. This parameter denotes how rapidly the emitter can give out a photon. However, since the emitter doesn't always decay with the generation of a photon, it is important to know the likelihood of photon emission. This can be defined as the *quantum efficiency* of the emitter (η_{int}), which can be derived as:

$$\eta_{\text{int}} = \frac{\nu_r}{\nu_r + \nu_{nr}} \qquad (2\text{-}20).$$

As we can see in equation 2-20, if we can increase ν_r, it is possible to increase the quantum efficiency of the emitter. Another important parameter is the frequency/wavelength of the radiation. The color of the light greatly affects the application of the radiation. We will discuss how the emission wavelength can be modified later in this thesis.

How do we obtain these parameters in real measurements? Throughout this thesis, we

use a technique named micro-photoluminescence (PL) to measure these parameters (See appendix B). In a PL measurement, the emitters are brought to their excited state by an external laser source. Radiation from the emitters is then collected and sent for analysis.

The signal collected during the measurement contains information of many different processes. In order to correctly interpret information from the signal, we must understand how these processes affect each other and the characteristics of the signal. Figure 2-8 shows possible energy flow of an emitter-cavity system.

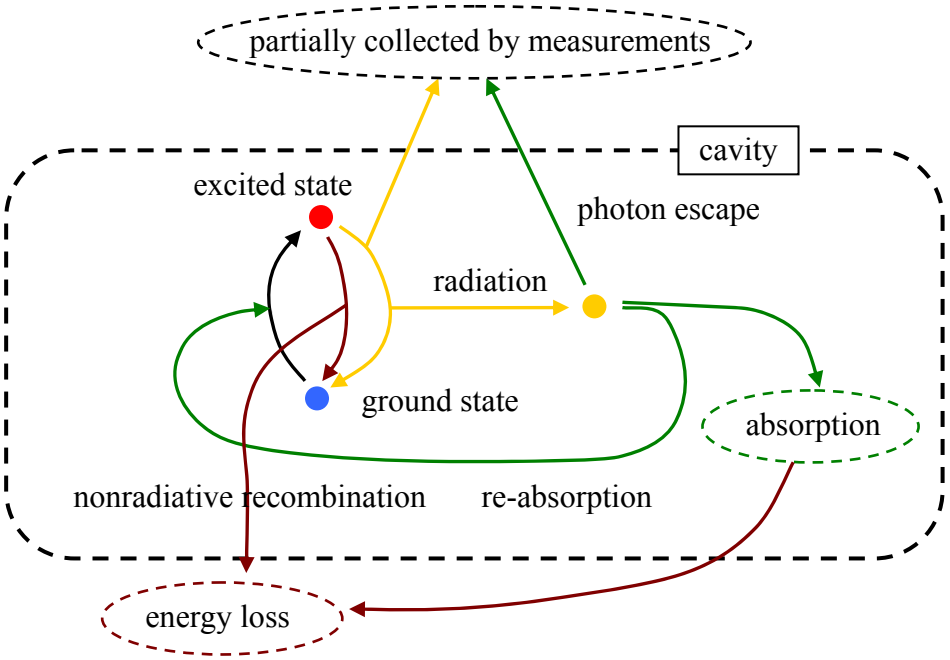

Fig. 2-8: Energy flow diagram of an excited emitter-cavity system.

At the center of the diagram lies the emitter we are interested in. As discussed earlier

in this section, the excited emitter will remain in its excited state for some time and then undergo either a radiative transition and emit photons (or surface plasmon polaritons) or a nonradiative transition and lose the energy without generating photons. The average time it takes before the transition occurs is called the lifetime (τ_{em}) of the emitter. This quantity can be derived as:

$$\tau_{em} = \frac{1}{\nu_r} + \frac{1}{\nu_{nr}} \tag{2-21}$$

When a radiative transition occurs (yellow paths in Figure 2-8), the emitter may either emit a photon into a resonant mode in the cavity or directly couple to a vacuum state as a traveling photon. If the traveling photon gets captured by the measurement system, it becomes background luminescence and may carry no information of the cavity resonance. What happens if the transition is coupled to a cavity resonance and emits a photon into a cavity mode? This photon trapped in the cavity may be re-absorbed by the emitter or be absorbed by the cavity itself and undergo some nonradiative transition. If neither of the above happens, it will eventually leave the cavity and may be captured by the objective into the detection system. The average time a photon can stay in the cavity is the lifetime of the photon (τ_{ph}). The photon lifetime is determined by all possible paths (green paths in Figure 2-8) as:

$$\frac{1}{\tau_{ph}} = \frac{1}{\tau_{escape}} + \frac{1}{\tau_{absorption}} + \frac{1}{\tau_{reabsorption}} + \ldots \tag{2-22}$$

and this number is proportional to the Q of the cavity mode.

The discussion above basically describes three main ideas: First, the average time it takes between excitation and photon collection from a cavity is the addition of τ_{em} and τ_{ph}. In the devices and materials described in this thesis, τ_{ph} is much shorter than τ_{em}. Therefore, the time transient of the emission is dominated by the emitter life time τ_{em}. The emission lifetime τ_{em} is affected by both ν_r and ν_{nr}. Second, the total quantum efficiency (η_{ext}) is a product of the probability that the emitter gives out a photon (η_{int}) and the probability that the photon is captured by the detection system (η_{cap}).

$$\eta_{ext} = \eta_{\text{int}} \cdot \eta_{cap} \qquad (2\text{-}23).$$

The capture efficiency (η_{cap}) is strongly related to cavity geometry and the set-up of the measurement system. In a photoluminescence system, unless well calibrated with a complete angular photon integration capability, it is difficult to determine the detection efficiency. Therefore, the absolute value of the detected intensity is usually not meaningful: we will depend on only the relative intensity change. Last, the detected signal is a combination of both photons escaping from the modes and background radiation. The ability to distinguish enhanced radiation from cavities relative to the background emission is essential in analyzing the signal. Examples of how to analyze the data will be presented later in the thesis.

Chapter 3
Experimental Demonstration of Plasmon Enhancement

3.1 Introduction

Demonstrations of cavity enhanced spontaneous emission using dielectric cavities have been presented [Ref. 27]. In these works, a major piece of evidence is the change of emission time transient in and out of a cavity. As discussed in Section 2.2, this time transient is governed by the lifetime of the emitter, which is affected by both radiative and nonradiative emission rate (γ_r and γ_{nr}). Therefore, these experiments are legitimate only under the assumption that the existence of the cavity only modifies the radiative transition rate. This is generally true for cavities made of lossless materials.

However, this assumption is not valid in metallic cavities. In Section 2.4, we described how the presence of metal can affect dynamics of a dipole. Besides the strong enhancement on surface plasmon emission, the metal structures can suffer from high rates of non-radiative recombination (lossy surface wave generation). The total recombination rate can therefore be modified by this quenching effect even in the

absence of changes to the radiative transition rate.

Increasing the nonradiative transition rate may also affect the internal quantum efficiency of the emitter, as described in equation 2-4. In addition, cavities made of lossy materials like metals having inherently strong absorption loss. This strong absorption can significantly reduce the external quantum efficiency of the structure. The reduction of quantum efficiency, both internal and external, could reduce total emission intensity from the cavity and make the enhancement of radiative transition rate meaningless. All these non-ideal effects together make demonstration of enhanced spontaneous emission in metallic structures ambiguous.

In this chapter, we present a metal gap geometry that can greatly increase surface plasmon emission enhancement to overcome quenching effects. Photo-luminescence measurement results will then be analyzed based on the models shown in Chapter 2 to conclude the decreasing of emitter lifetime as enhancement in spontaneous emission rates.

3.2 Plasmonic gap mode cavities

The experiment described in this chapter characterizes the emission properties of fluorescent organic dye tris-(8-hydroxyquinoline) aluminum (Alq3) in gap mode plasmonics structures. Similar to the model introduced in Section 2.2, after the

incorporated dyes absorbs energy from an incident laser the total transition rate (ν_{tot}) from the excited state back to the low energy state is the combination of the enhanced radiative emission rate (ν_r), the metal induced quenching rate (ν_{nr1}) and the intrinsic non-radiative recombination rate of Alq3 film (ν_{nr2}). Among those parameters, ν_r is proportional to the electric field strength of plasmonic modes, ν_{nr1} depends on the distance between the metal and the emitter and ν_{nr2} is an intrinsic property of Alq3 film that therefore shouldn't be changed by the cavity.

In order to increase the radiative emission rate to overcome the metal quenching, one needs to be able to modify the mode field strength without bringing the emitter closer to the mirror. The idea is to use a metal gap structure, as shown in Figure 3-1. An emitter layer is placed a small distance from a metal surface (mirror A in the plot), then another metal surface (mirror B in the plot) is introduced to the system with a variable distance to the first mirror. As the distance between the two metal surfaces becomes smaller than inverse of the exponential decay constant of the surface plasmon polariton modes of the isolated mirrors, the two plasmonic modes hybridize and form a gap mode plasmon. The electric field intensity could be significantly larger as the gap thickness is much less than the normal decay constant. However, since the metal quenching is a short range effect and should be dominated by the closest metal surface, in this geometry ν_{nr1} is not changed as long as the distance between the emitter and mirror B is

significantly larger than the distance to mirror A.

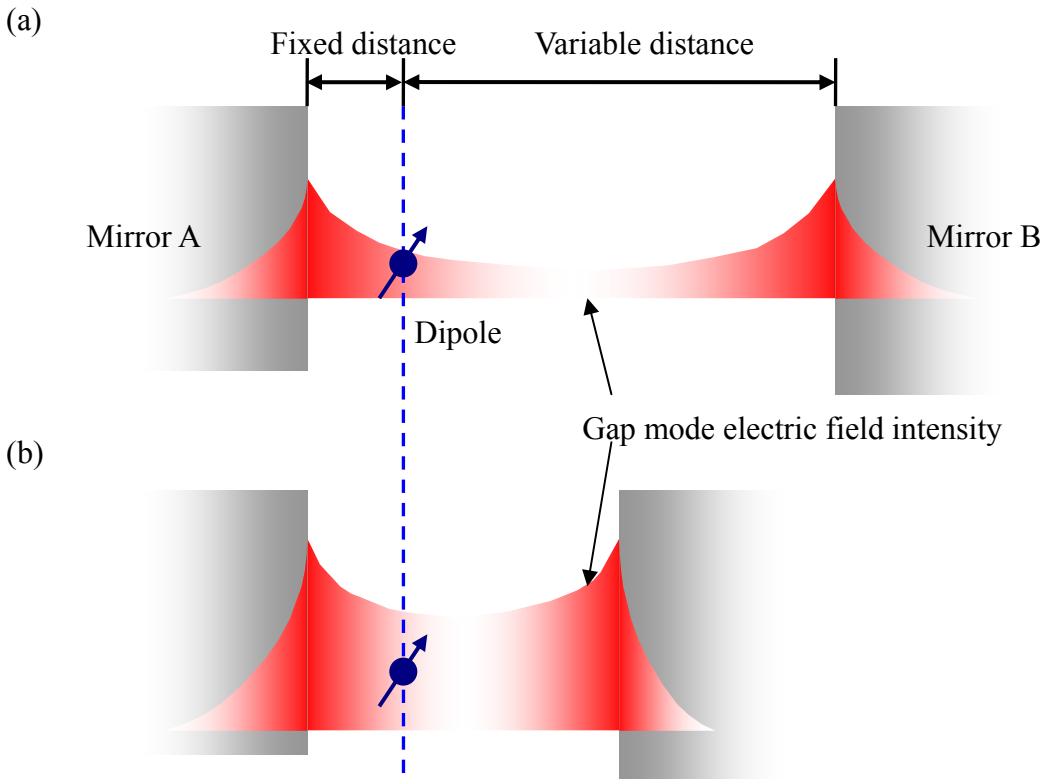

Fig. 3-1: A metallic gap structure containing a dipole with a (a) thicker and (b) thinner gap. This geometry allows us to isolate effects on radiative and nonradiative rates.

How the transition rates could be affected in such geometry can be theoretically calculated based on the model introduced in Section 2.4. In the calculation, a randomly oriented dipole is placed 2nm away from the top silver layer modeled by properties taken by Johnson and Christy [Ref. 28]. This dipole is embedded in a 2.6nm Alq3 film

(refractive index = 1.7). An Al_2O_3 spacer is placed between this film and the bottom silver layer with a refractive index of 1.62. Radiative and nonradiative rates (ν_r^0 and ν_{nr2}) of bulk Alq3 are measured to be $1/46ns^{-1}$ and $1/12ns^{-1}$ (see appendix B). The calculated decay rates and quantum efficiency versus spacer thickness is shown in Figure 3-2.

As described earlier in this section, the gap mode plasmon emission rate (green curve in Figure 3.2 (a)) increases rapidly with decreasing gap thickness as the metal quenching rate remains (red dashed curve in Figure 3.2 (a)) the same for most of the part of the figure. As the gap thickness reduces to ~7nm (spacer thickness ~4.5nm), the gap mission rate catches up with the metal induces nonradiative rate and the radiative efficiency reaches 0.5 in Figure 3.2 (b).

The calculation demonstrates the possibility of using enhanced plasmon emission in a narrow metal gap to overcome metal quenching. However, fabricating such a device is difficult. The major challenge is the smoothness of the silver surfaces. For an interface bounded wave like surface plasmon polaritons, the propagation length is strongly dependent on the smoothness of the interface.

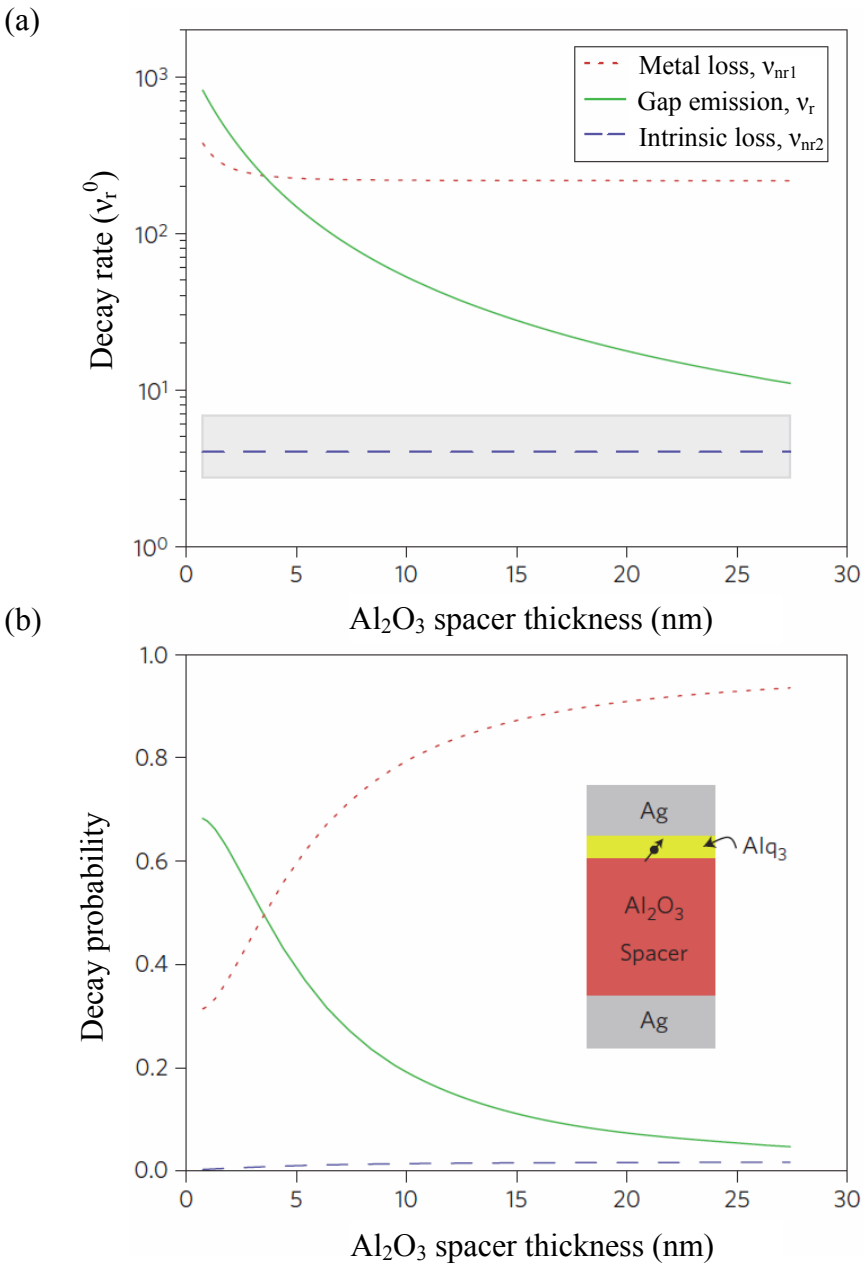

Fig. 3-2: Theoretical emission (a) rate and (b) efficiency versus spacer thickness. Green lines are emission into gap mode plasmons; red dashed lines are quenching due to metal losses and blue dashed lines are intrinsic non-radiative transition in Alq3 film. The gray area denotes the 95% confidence interval from the Alq3 emission rate measurement (appendix B).

In our devices, the silver substrate is fabricated with a template stripping method [Ref. 29]. We evaporated 300nm of silver onto an atomically smooth silicon wafer under a pressure of ~$5x10^{-7}$ Torr. Another silicon wafer piece served as a handle that was attached to the silver surface using epoxy (EPO-TEK 377, Epoxy technology) cured by baking at 150°C for 3hrs. Removing from the template was done by sliding a razor blade under the corner of the handle. With this method, surface of the silver is defined by the atomically smooth silicon "template" and a sub-nanometer root-mean-square (r.m.s.) roughness was obtained. A process flow chart of such a technique is shown in Figure 3-3.

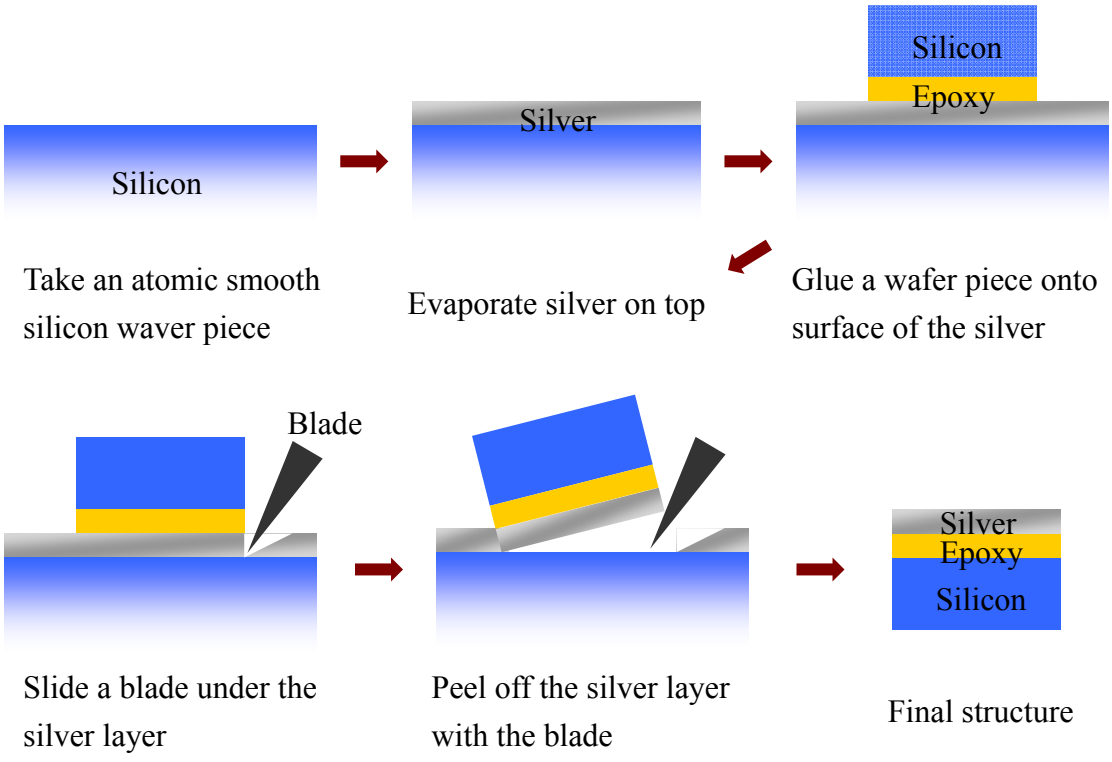

Fig. 3-3: Process flow of template-stripping for making smooth silver surface

The freshly produced silver surface was immediately covered with an Al_2O_3 spacer deposited by atomic layer deposition (ALD). The organic dye Alq3 was then thermally evaporated onto all samples under a pressure of ~$4x10^{-7}$ Torr for ~2.6nm. Applying the top silver layer onto the fabricated structure could be tricky. First, the process used to deposit silver may induce damage onto the Alq3 film. This may change the intrinsic non-radiative transition rate of the dye layer (ν_{nr2}). Second, without a dense oxide as a barrier layer on top of Alq3, silver atoms with high kinetic energy may diffuse into the film without forming a clear interface. Last, performing photoluminescence measurement on devices covered by opaque metal layer is difficult.

A cavity design along with a fabrication method was developed by Kasey J. Russell in 2010 to solve all the three problems mentioned above at once [Ref. 11]. In this structure, the top silver film was replaced with chemically synthesized silver nanowires. These nanowires (made by Blue Nano) of diameters ~100nm and length ~<1-30μm were suspended in ethanol and dropped onto a clean silicon wafer. After the ethanol was dried, a piece of polydimethylsilozane (PDMS) served as a soft stamp was pressed onto the wafer. Some of the nanowires were picked up by the PDMS piece and transferred onto the silver/Al_2O_3/Alq3 substrates.

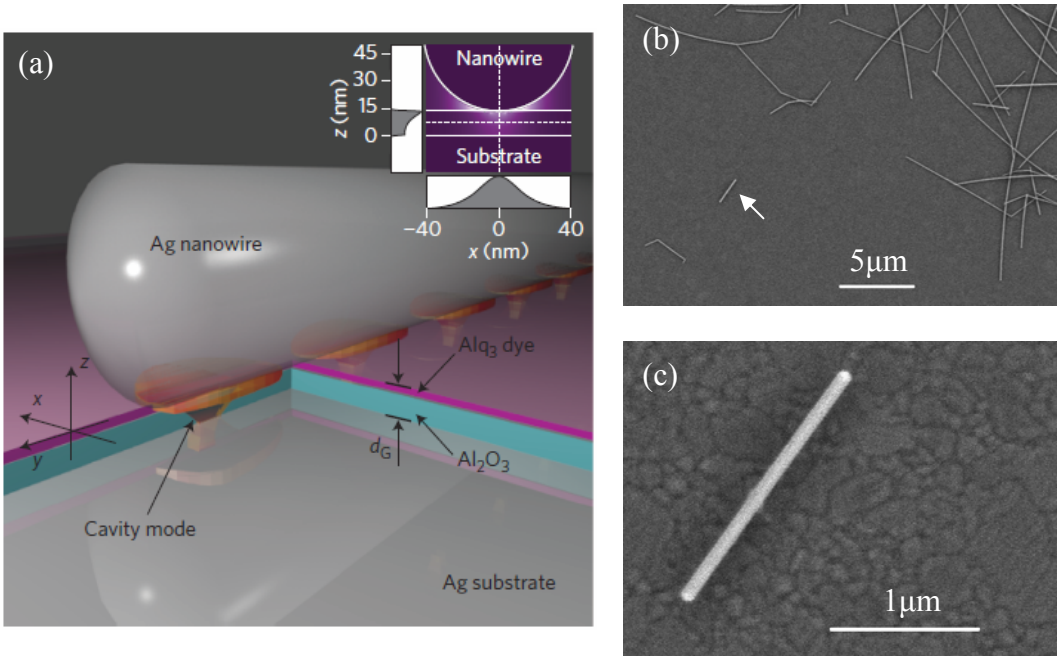

Fig. 3-4: (a) Schematic view of a gap mode plasmonic cavity used in this work. The inset is a cross –section view of electric field distribution in a cavity. (b) SEM image of an area on one sample with multiple nanowires dispersed. (c) SEM image of a single nanowire cavity (marked with arrow in (b)). Patterns on the substrate show silver poly crystalline grains.

An illustrated cavity structure is shown in Figure 3-4 (a). The total gap distance d_G is chosen to be 5-25nm. This distance is determined by the thickness of the Al_2O_3 spacer layer. The ALD technique used to deposit this layer allows very accurate control over the film thickness varied between samples to yield the desired gap spacing with fixed Alq3 thickness. The atomically smooth silver nanowire surface, template stripped

smooth silver substrate and well controlled gap thickness enables strong field concentration within the gap. A finite difference time domain simulated electric field distribution in a 15nm gap device is shown in the inset of Figure 3-4. The electric field is concentrated into a 15nm high, ~60nm wide cross-sectional area underneath the nanowire. The simulated mode volume for ~1μm long nanowire is ~$10^{-5}$$um^3$ in visible-near infrared range.

Figure 3-4 (b) shows a top-down scanning electron microscope image of fabricated cavities. Several nanowires are shown in the image. Only a small amount of dye locating underneath the nanowires can couple to the gap modes. Therefore, dye molecules covering a great area between the nanowires cannot radiate into the cavity modes and become a source of background emission.

The fabricated structure was then characterized with photoluminescence measurement, as mentioned in Section 2.2. The excitation source was a pulsed ti:sapphire laser tuned to 920nm and frequency doubled to 460nm in wavelength. The laser was first depolarized by coupling to a single mode fiber and the focused onto the sample using a 100X, 0.9 NA objective. The spectral response of the dye radiation was analyzed with a grating spectrograph with liquid nitrogen cooled charge-coupled device (CCD) camera. The excitation power was ~40nw and the integration times are 30s for spectra and 2-5min for time traces.

Examples of collected spectra are shown in Figure 3-5 (a). As discussed in the previous section, dye molecules located away from the nanowires emit as background. Therefore, we can characterize these cavities by comparing emission from them to the background. Without coupling to cavity modes, the organic dye Alq3 gives a broad luminescence over the visible range (red curve in Figure 3-5 (a)). In contrast, emission taken with the laser spot on a nanowire (blue curve in Figure 3-5 (a)) showed distinct cavity modes with Q of ~50. These modes are due to Fabry-Perot type resonance of the gap-mode plasmons traveling along the length of the nanowires and reflecting at the end of the gap. The regular presence of these resonant peaks is an important signature of such an interference phenomenon. The Qs are limited by the finite metal loss and strong scattering loss at the nanowire terminations.

In addition to the presence of resonating modes, the intensity and decay rate of the emission are also greatly altered by the cavity. These effects can be observed in time resolved PL intensity as shown in Figure 3-5 (b). Comparing the on-cavity (blue curve) and off-cavity (red curve) traces, one can easily find that both peak and integrated intensity of the on cavity signal is orders of magnitude higher than the off-cavity emission. This increase in signal intensity can be a result of either the increase of internal quantum efficiency of the molecules by radiation enhancement or the improvement of collection efficiency by antenna effects produced by the silver

nanowires.

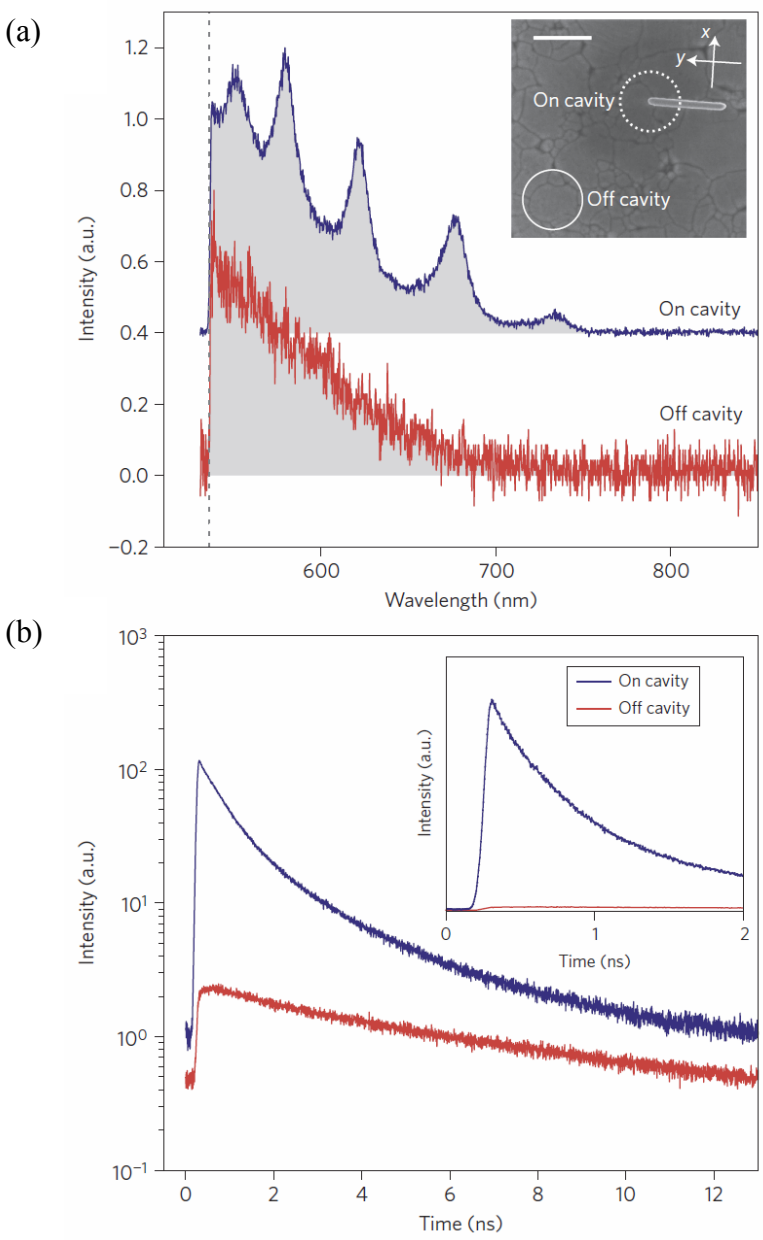

Fig. 3-5: Photoluminescence measurement results from the nanowire cavities. (a) Normalized spectra measured on and off the cavity. (b) Time resolved PL measured on and off cavity, the inset shows the same data in linear scale.

Another major difference between the two time-resolved PL curves lies in the slope of the semi-log curves. It can be found in Figure 3-5 (b) that the on-cavity emission decays much faster than the off-cavity emission. This is an indication of significantly reduced emitter lifetime in cavities. This reduction of lifetime can be a result of modification of either radiative or non-radiative rates. The originality of this reduction remains unclear without fully understanding of the dynamics of the emitter.

3.3 Analysis and Discussion

In order to further analyze the change in intensity and decay time with the calculated mode shown in Figure 3-2, a series of samples were fabricated. As discussed in the previous section, the cavity design allows us to accurately control the gap width by changing the Al_2O_3 spacer layer thickness. Six samples with the spacer thickness ranging from ~2nm to ~ 22nm were made and each of them was dispersed with silver nanowires. Roughly 10 cavities were randomly selected on each sample and probed with our PL measurement.

Accurate interpretation of the data collected relies on quantitative analysis over the curves. In principle, a time dependence of a PL signal can be expressed as:

$$I(t) = I_0 \exp(-\frac{t}{\tau_{em}}) = I_0 \exp(-v_{tot} t) \qquad (3\text{-}1)$$

where τ_{em} is the lifetime of the emitter, as described in equation 2-5. This formulation

describes a linear trace with negative slope in the log(I(t)) versus time plot, as shown in Figure 3-5 (b). Absolute value of the slope of the curve is equal to the decay rate of the excited emitter population (v_{tot}). Using this formulation to analyze the time resolved PL curve, first we must notice that the measured trace does not have a fixed slope in the semi-log plot. This is due to the inhomogeneous distribution of molecules. Since the diffraction limited laser spot is larger than the sub-wavelength structure, each measurement probes a range of emitters within and around the cavity. Therefore, the collected time trace contains signals with various decay constants. To isolate these components, a three exponential model as:

$$I(t) = a_0 \exp(-v_0 t) + a_2 \exp(-v_2 t) + a_3 \exp(-v_3 t) \qquad (3\text{-}2)$$

was used to describe the curves. Each term in equation 3-2 describes the emission characteristics of a group of dye molecules. In our analysis, we only care about behavior of the group dyes that overlaps and interacts with the cavity the most. Therefore, the intensity and lifetime of the emitters used in the following analysis are fitting results from the term with the shortest lifetime.

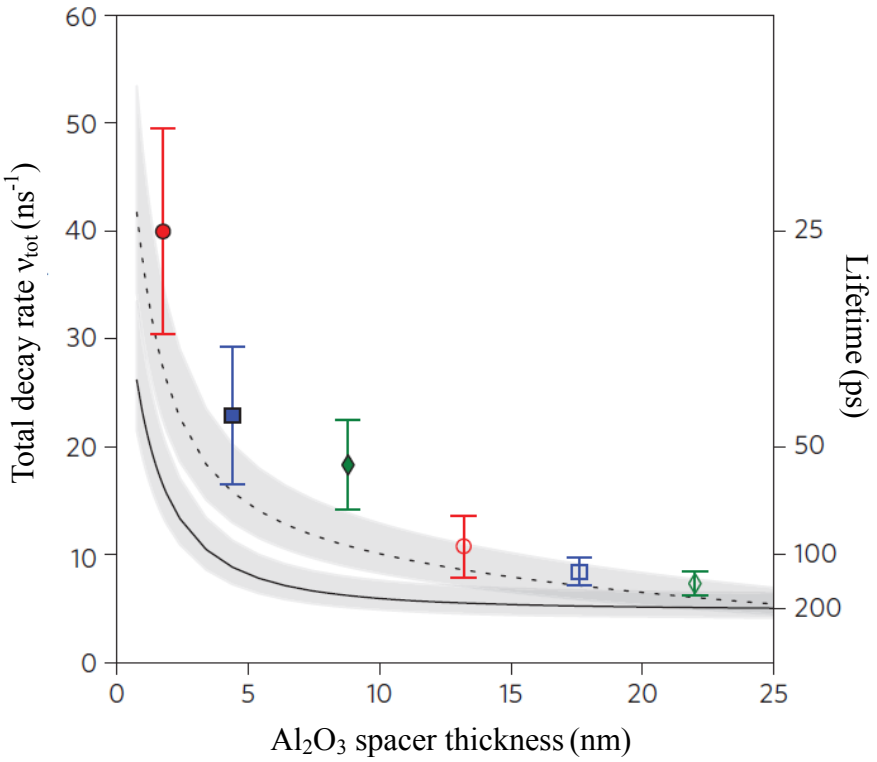

Fig. 3-6: Total decay rate versus Al_2O_3 spacer thickness. Symbols are averaged through measurements on multiple cavities over one sample and the error bars are the standard deviation between these cavities. The solid line is calculated from Figure 3-2 and the dashed line is the same calculation with corrected emitter-metal distance. The shaded areas are 95% confidence interval of the measurement of v_r^0.

The averaged total decay rate (inverse of lifetime) versus spacer thickness is shown in Figure 3-6. Obvious increasing of decay rate with decreasing gap spacing can be found in the plot. Further comparing the data with calculated total decay rate shown

in Figure 3-2 with no fitting parameters, good agreement on the absolute scale of v_{tot} and its dependence on gap spacing is predicted by the model. Note that the model used to produce Figure 3-2 assumes planar metal surfaces on both sides, which is clearly not the case in our geometry. A major difference is that the effective distance from the dipole to the curved nanowire surface is larger than the vertical distance between the two. Therefore, a calculation with a corrected dipole-metal distance estimated by finite difference time domain simulation is also displayed in Figure 3-6 (dashed line) as well as the original calculated results (solid line).

Besides a demonstration of how the total decay rate is affected by the gap thickness, we can further estimate how much the radiation into gap mode plasmons is responsible for the decay rate change by correlating the decay rate with emission intensity. If we integrate over a time transient curve as shown in equation 3-1, we should get the total number of photons acquired. This number should be equal to the total number of emitters times the external quantum efficiency. Combining this idea with the definition of quantum efficiencies described in Chapter 2 gives:

$$\eta_{ext} N = \eta_{cap} (\frac{v_r}{v_{tot}}) n = \int_0^\infty dt I_0 \exp(-v_{tot} t) = \frac{I_0}{v_{tot}} \tag{3-3}$$

where N is the total number of excited molecules. This gives an expression of the peak intensity as:

$$I_o = N \eta_{cap} v_r \tag{3-4}.$$

For constant collection and excitation efficiency, the peak intensity of the curve is proportional to the radiative transition rate. We can use this relation to verify that the observed changes in the total decay rate (v_{tot}) is primarily due to changes in the radiative decay rate (v_r) by plotting I_0 versus v_{tot} for all the cavities we measured.

In Figure 3-7, a strong positive correlation between the total decay rate and the peak intensity is observed, confirming the presence of spontaneous emission enhancement into gap modes. This behavior is in good agreement with the predicted total decay rate dependent on radiative decay rate shown in Figure 3-2 (a). Comparing the data and the calculated dependence allows us to estimate the magnitude of enhancement. Figure 3-7 also shows a result of fitting the data with the calculated curve (black dashed lines) with only one scaling factor $N\eta_{cap}$ as the fitting parameter. Knowing this factor allowed us to map the peak intensity to the radiative transition rate through equation 3-4. The enhancement factor was then estimated by dividing the mapped radiative transition rate by the radiative transition rate of bulk Alq3 (1/46 ns^{-1}, see appendix B). The result is shown as the left y-axis in Figure 3-7. These data indicate that the emission enhancement in our cavities is ~50-1000 and the total decay rate of the brightest cavity approaches 2000 times faster than v_r^0.

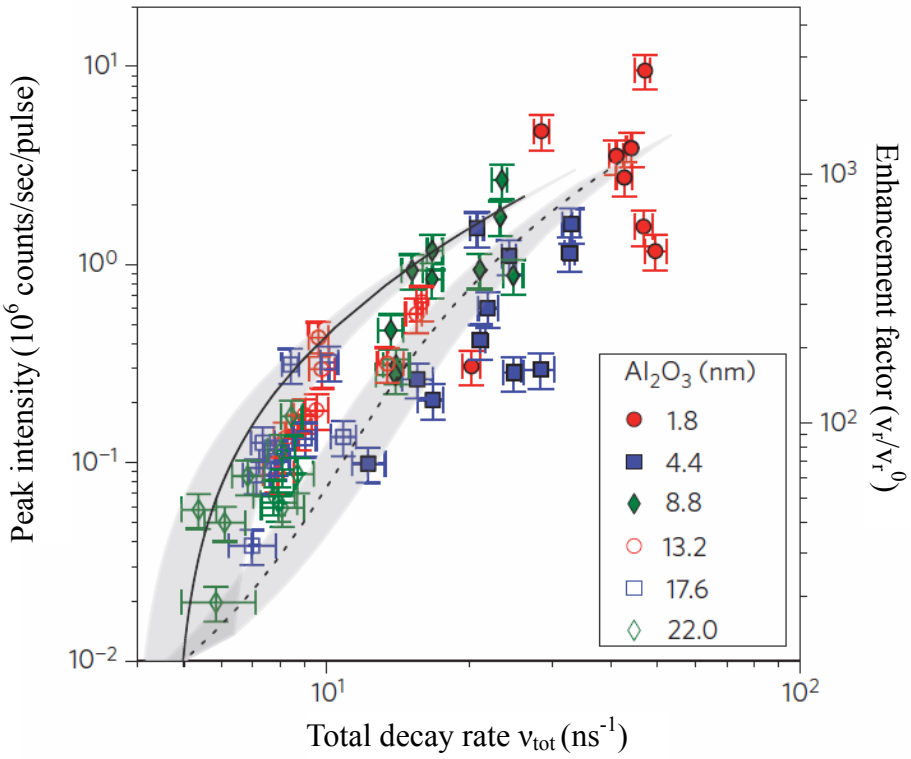

Fig. 3-7: Peak intensity versus total decay rate for all measured cavities. Symbols are experiment data and lines are created by the same calculation as in Figure 3-6.

One must notice that for the analysis to be valid, the scaling factor $N\eta_{cap}$ must not change significantly with various gap thicknesses. Satisfying this requires both the excitation and collection efficiency to not vary with gap thickness. These two conditions cannot be demonstrated by the measurement but can be shown with numerical calculations. In order to verify the change in absorption and collection efficiency of our nanowire cavities with respect to gap spacing. we performed finite difference time domain simulations (FDTD, see appendix D). The cavity simulated

consists of nanowires with length of 800nm and diameter of 100nm with various Al_2O_3 spacer thicknesses.

To simulate absorption, the Alq3 layer is modeled as a 3nm thick slab of lossy dielectric with refractive index 1.76+0.22i. These numbers are combination of our measurement with ellipsometer (real part) and from former published results (imaginary part) [Ref. 30]. The spacer thickness used is 1.6 and the silver optical properties are taken from Johnson and Christy [Ref 28]. During the simulation, an excitation laser at 460nm was focused to the end of the nanowire with a 0.9NA objective. Power dissipation within the absorption layer was recorded, as shown in Figure 3-8.

As shown in Figure 3-8 (a), the structure concentrates the incident laser into the gap and improves absorption under the nanowire. In fact, the small area under the nanowire is responsible for 10-70% of the power absorption while the laser is focused at one end of the nanowire, as one can see by comparing the black and green curve in Figure 3-8 (b). A more significant result shown in Figure 3-8 (b) is that the difference of absorption for cavities with different thickness all lies within one order of magnitude. The variation is small compare to the scale of intensity variation shown in Figure 3-7.

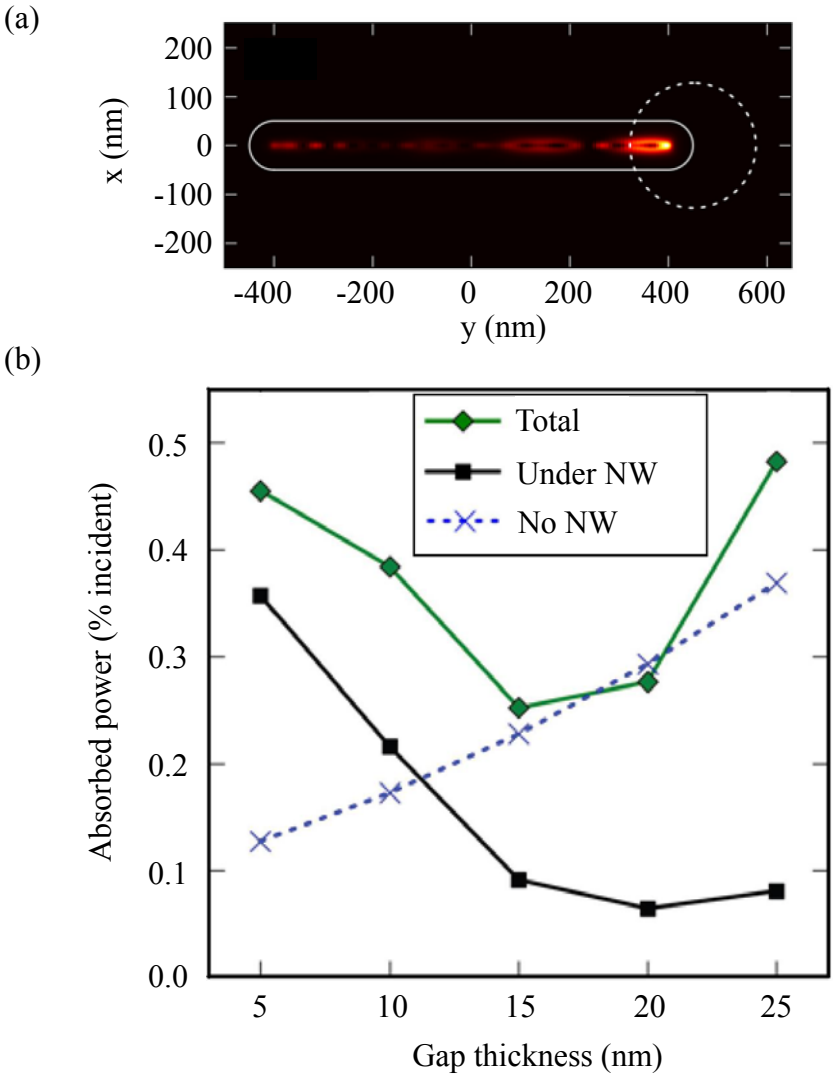

Fig. 3-8: FDTD simulated absorption within nanowire cavities. (a) Power absorption distribution in the plane 2nm below the nanowires for cavities with gap spacing of 5nm, the white broken circle denotes areas covered by the incident beam. (b) Absorbed power normalized to incident power versus gap thickness. Data includes power absorbed by the entire Alq3 layer (Total), areas under the nanowire (area enclosed by solid line in (a), Under NW) and a control geometry with on nanowires (No NW).

Similar simulation can be performed as a dipole source is used to replace the absorption layer in the same structure. The dipole is placed 2nm below surface of the nanowire and oriented perpendicular to the metal surfaces radiating at a wavelength range of 550-650nm. Three quantities were recorded as a function of gap spacing: the total power radiated by the dipole, the power escaped from the cavity and power collected by a 0.9NA objective. We can then calculate the collection efficiency based these parameters.

As the gap spacing is as small as 5nm, the total power radiated by the dipole is ~2000 times higher than a dipole in bulk dielectric with a refractive index of 1.6. Among all the power radiated, ~10% at 550nm and ~ 35% at 650nm can escape from the cavity. Only another factor of 30% of this power is collected by the objective. For a larger gap of 25nm, the total power radiated is roughly one order of magnitude lower. The fraction of power escaping is ~20% at 550nm and ~35% at 660nm. The percentage of escaping power collected by the objective is roughly the same. These results give us a photon capture efficiency of ~7-10% and this number is not sensitive to the gap spacing. Both simulations on absorption and collection suggest that the intensity variation observed in Figure 3-7 is from the change in radiative decay rate.

3.4 Conclusions and Outlooks

In conclusion, this work provides clear evidence for a 1000-fold enhancement of radiative emission rate into gap plasmon modes relative to the same emitter in bulk dielectric film radiating into propagation photon modes. This large enhancement is provided by the highly concentrated field squeezed into a small gap between two smooth silver surfaces. The capability to accurately control the gap spacing in our design enables all the quantitative analysis of the emitter dynamics in the structure, ultimately yielding a detailed understanding of the contributions of radiative rate enhancement and loss in the cavities.

However, there are three major shortcomings for these devices. The first one is the low external quantum efficiency. The ultimate goal for enhancement of spontaneous emission is to acquire more useable optical signals from the emitter. Therefore, even if we can greatly increase the efficiency of emitting into gap mode plasmons, it won't be useful unless we can improve the extraction efficiency of these plasmons. One solution to this problem is to replace the nanowire with a well designed metal patch to make radiation more efficient. Another possible route is to combine these plasmonic cavities with waveguides and antennas to form integrated plasmonic circuits. This strategy allows us to couple out emitted plasmons before they are scattered or absorbed.

The second problem is that the lateral confinement of the cavity failed to enable

demonstration of higher enhancement and spectral selectivity in these cavities. According to the formulation of Purcell amount introduced in Chapter 1, the enhancement should be inversely proportional to mode volume, which should be scaled with nanowire length. To verify this idea, we can plot the dependence of peak intensity on both gap spacing and wire length as in Figure 3-9. No obvious correlation between wire-length and peak intensity is found in the figure. This is owing to the fact that the emission bandwidth of the organic dye Alq3 is much broader than the free spectral range of the cavities. As a result, overall emission enhancement onto the emitter is an average over the whole emission spectrum, including both constructive and destructive interfered frequencies. Therefore, resonances produced by lateral confinement have no effect on the dynamics of the dyes. Even stronger enhancement with spectral selectivity can only be realized with a narrow band emitter interacting with a cavity with well controlled frequency response.

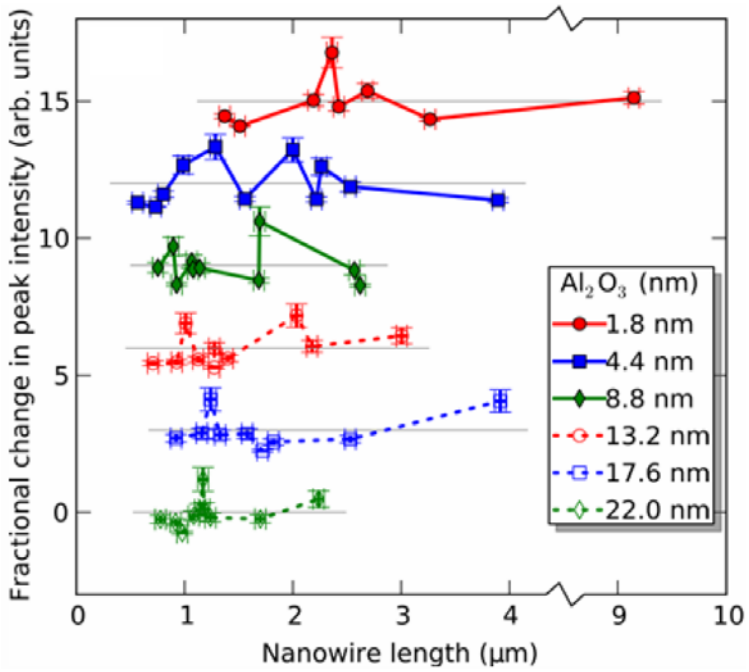

Fig. 3-9: Peak intensity versus nanowire length measured from all cavities used to produce data in Figure 3-6 and 3-7. The peak intensity is normalized to the average of cavities with 25nm gap spacing.

Possible solution for the previous two problems relies on overcoming the last disadvantage of the cavity design which is that since this geometry relies on the atomically smooth surface of those chemically synthesized nanowires, precise control over the length and orientation of those wires seems to be impossible. This significantly reduces our control over the frequency response and radiation direction of the cavity. Moreover, the difficulty in placing the cavities eliminates the possibility of building an integrated system with these devices. Therefore, new cavity designs which allow precise control over orientation and dimension are important for further improving the

project. Several cavity geometries designed for this purpose will be demonstrated in the following chapters.

Chapter 4
Deterministically Defined Metallic Trench Cavities

4.1 Introduction

In previous chapters, we discussed how large spontaneous emission enhancement can be realized by strongly concentrated fields in plasmonic cavities. In addition to simply concentrating optical fields, the creation of well-defined resonant modes should provide us with selective control over light-matter interactions both spatially and spectrally. Such selective enhancement allows deterministic observation of phenomena like enhanced spontaneous emission, ultra-low threshold lasing and strong coupling between photonic and electronic states [Ref. 2, 31]. Some of these phenomena have also been demonstrated with plasmonic cavities [Ref. 32, 33].

However, in the formation of these plasmonic cavities, there is much room for improving the cavity geometry and structure to ensure well controlled dimension and orientation. For example, the cavity we demonstrated in Chapter 3 relies on the atomically smooth surface of the synthesized silver nanowires, which have diverse

lengths and widths that cannot be well controlled. Moreover, dispersing them onto the silver substrate with precise positions and orientations is nearly impossible. Thus, the inaccuracy of the final cavity structure due to difficulties in fabrication affects the Q of these cavities. As high Q cavities require well designed reflectors to confine optical fields, the challenges in fabricating the reflecting interface as-designed significantly reduce their performance.

Techniques developed for fabricating integrated circuits on surfaces of semiconductor wafers provides us with the inspirations and designs to solve these problems. Fabrication strategies based on various lithographical methods allow us to accurately define the geometries. Therefore, in this chapter, we present two fabrication methods, focused ion beam (FIB) milling and revered image mold (RIM) defined by electron beam (Ebeam) lithography, to create precisely controlled and defined metallic trench cavities We then present both simulation and experimental results of these trench cavities. .

4.2 Focused Ion Beam (FIB) Milling for Fabrication of Metallic Trench Cavities

Narrow trench structures have been previously identified as excellent candidates for plasmonic waveguides with highly concentrated fields [Ref. 34, 35]. Similar to how

dielectric cavities can be created out of dielectric waveguides, various design of plasmonic cavities have been presented by different ways of terminating metallic trench waveguides. In dielectric systems, this design strategy allows us to couple cavities with waveguides and other optical devices for integrated optical systems. However, such designs are relatively difficult for plasmonic cavities since evanescent coupling is ineffective for the highly concentrated field of surface plasmons.

In this work, we propose to use size modulation of metallic trenches as Bragg reflectors to form plasmonic cavities. This design allows us to tune the cavity confinement by adjusting the number of layers of modulators or reflectors, hence enabling cavity-waveguide and cavity-cavity coupling.

A schematic view of the proposed structure is shown in Figure 4-1. The devices used to produce the simulation and measurement results presented later in this chapter have periods/lattice constants ranging from a = 400nm to 500nm, a cavity length L = 2a and a narrower modulation length of d = 150nm. The definition of all these parameters can be found in Figure 4-1 (a). The control of trench depths for the thicker part, h_1, and for the thinner part, h_2, will be discussed during the fabrication process in subsequent paragraphs.

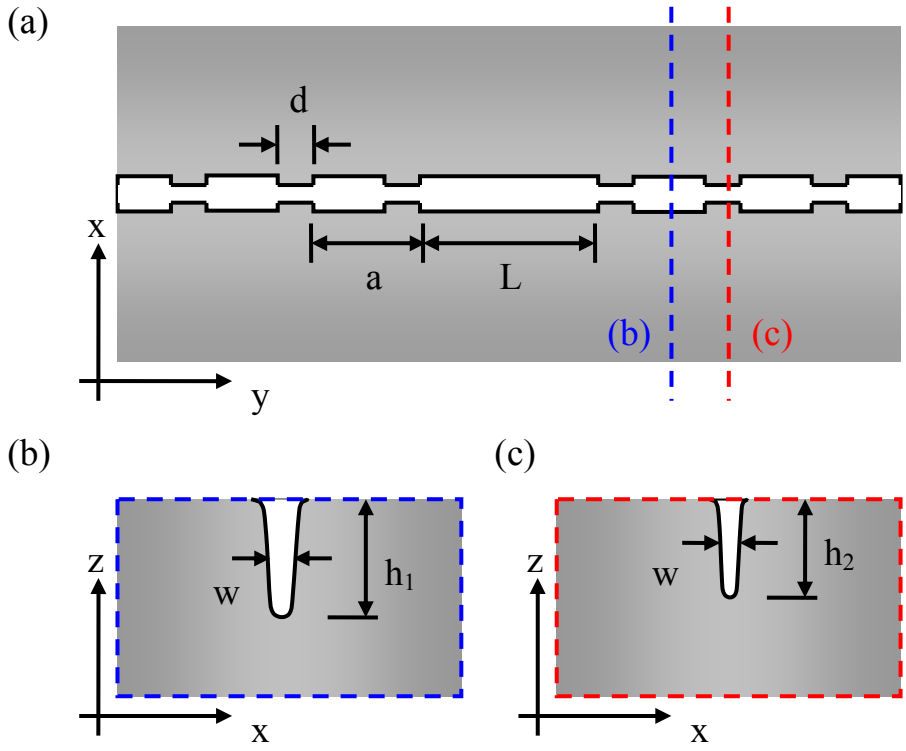

Fig. 4-1: Schematic cartoon of the trench cavity: (a) a top-down view, (b) a cross-section view of the wider part of the trench (blue dashed line in (a)) and (c) a cross-section view of the narrower part of the trench (red dashed line in (a))

A straightforward way of fabricating such structures is to use focused ion beam (FIB) milling to create the trenches directly into metal substrates [Ref. 35]. The metallic material chosen in this work is silver, which has been demonstrated to be a good plasmonic material for most of the visible frequency range. As discussed previously, the smoothness of the metal in these plasmonic devices is of upmost importance. In our experiment, the silver substrate on which the trenches were drawn is epitaxially grown

on the (111) surface of single crystal gold plates. These gold plates were synthesized by heating to 130˚C a precursor containing $(AuCl4)^-$ stabilized in hydrogen tetrachloroaurate(III) hydrate, tetraoctylammonium bromide (ToABr) on a flat substrate [Ref. 36]. The gold ions in the solution then precipitate into crystallized plates over a period of time roughly 72 hours. The grown plates were rinsed in toluene and treated with oxygen plasma to further remove residual organic contaminants from the surface.

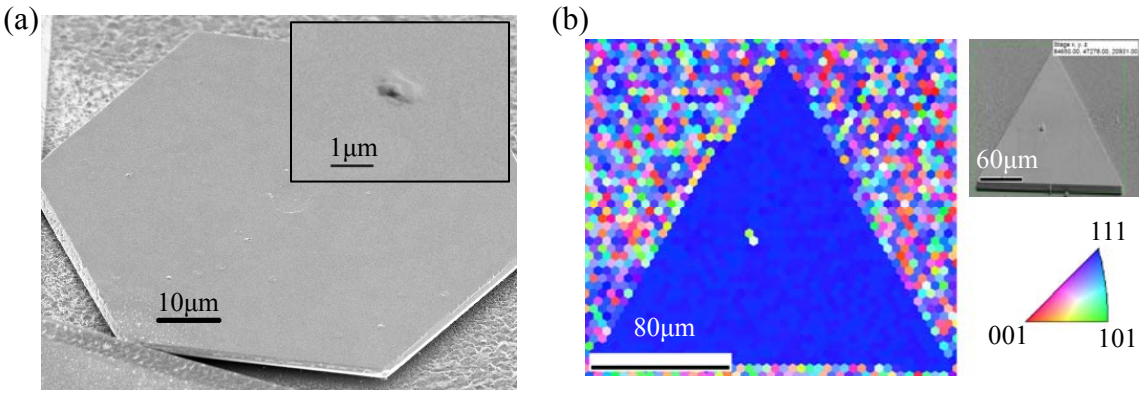

Fig. 4-2: (a) SEM images of a silver-on-gold plate, the inset shows a zoomed-in image of the plate. (b) EBSD results of a silver-on-gold plate.

An epitaxial layer of silver is grown via sputter deposition in a magnetron sputtering system [Ref. 37]. A silver target was bombarded with argon plasma under a pressure of 2milli-Torr and the silver atoms were deposited onto the gold plates with a substrate temperature of 170˚C at a rate of ~3nm/min. No clear grain boundaries on the grown silver layer were observed with SEM (4-2 (a)). Electron backscatter diffraction

(EBSD) was used to identify the orientation of the silver lattice, as shown in Figure 4-2 (b). The silver lattice grown on the gold plates are well arranged with (111) plane on top, agreeing with the orientation of the gold crystalline structure.

To fabricate the cavity, immediately following the sputtering silver on gold plates, a 5nm SiO_2 layer was sputtered onto surface of the silver. The trench cavities were then etched into surface of the silver substrate with a Zeiss cross-beam FIB system. A gallium ion beam with an accelerating voltage of 30kV and a charge current of 10pA were used for the etch. The narrower and wider parts were defined by varying line doses of the ion milling from 1000μC/cm to 2000μC/cm. The dosages were chosen to provide trenches with $h_1 \sim 200$nm and $h_2 \sim 100$nm. However, depth of the fabricated device is strongly dependent to spot size of the ion beam. SEM images of the fabricated trenches are shown in Figure 4-3.

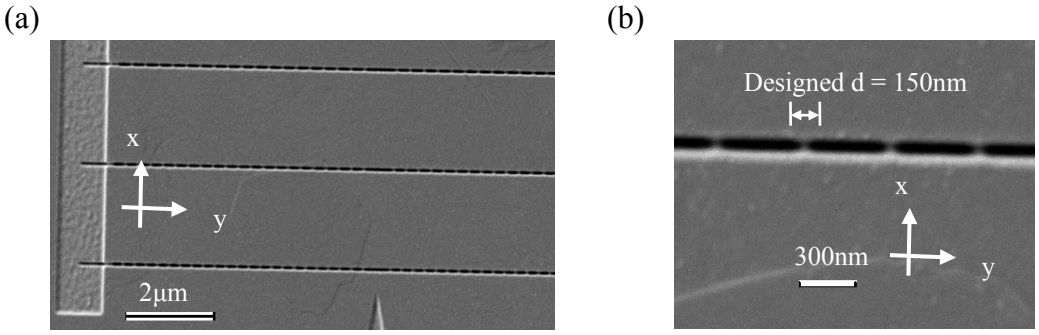

Fig. 4-3: (a) A SEM image of fabricated trench cavities and (b) a zoomed in view of the width-modulated trench with a = 500nm. The labeled length is the designed length of the thinner part of the trench.

A zoomed view of a fabricated trench with a = 500nm is shown in Figure 4-3 (b). The image clearly shows the difficulty in precisely defining the trenches with FIB. First, the width of the trenches was defined by the finite spot size of the ion beam (15 – 50 nm, depending on the FIB current) and the metal sputtering process. The thinnest trench we achieved with FIB had a width of ~ 70nm. Second, the length of each section was deformed from the original design with the FIB process. Because a higher electron beam dose was used to create the wider parts of the trench, the milling resulted in expansion in both x and y directions. As a result, length of each section is different than the designed length and the boundaries between sections are not clearly defined.

Another unavoidable source which may degrade the cavity performance is the Ga implantation from the FIB ion beam. To verify possible Ga implantation, electron-dispersive X-ray spectroscopy (EDX) was performed to measure material composition of the FIB-etched structures.

Figure 4-4 shows EDX spectra on areas with and without FIB milling on the same silver-on-gold plate detected with an electron accelerating voltage of 5kV. Without milling, a few peaks correspond to silver, aluminum and oxygen can be found. The oxygen could be either from surface oxidization or the SiO_2 protective layer. It is still unclear what the source for aluminum signal on surface could be. In contrast, both the oxygen and the aluminum peaks disappeared in the etched area and a gallium peak was

observed instead. The implanted gallium atoms serve as impurities in the silver and may cause reduction of its conductivity.

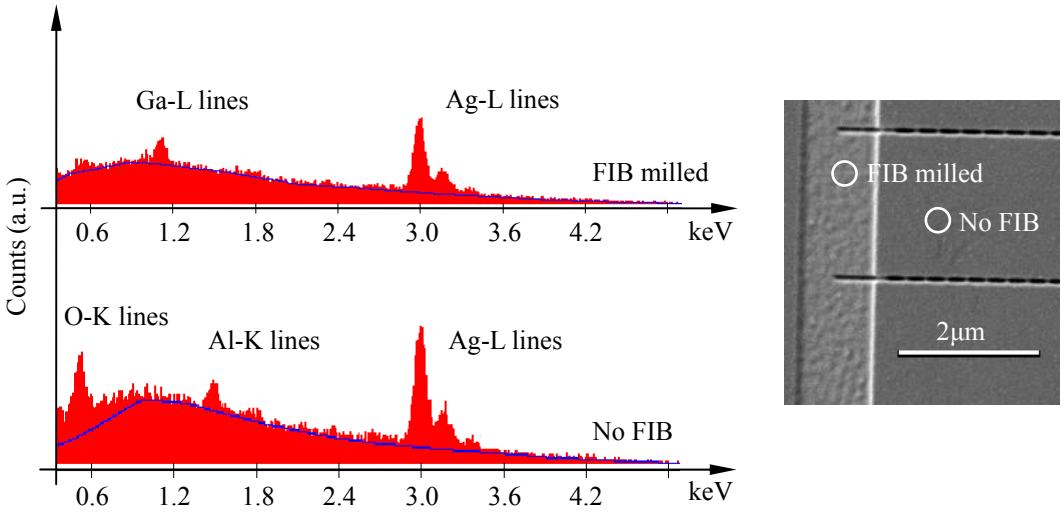

Fig. 4-4: EDX spectra for FIB milled silver trenches.

As a short summary for using FIB to fabricate the trench cavities, the width of the trench and the smoothness of the metallic sidewalls defined by FIB are limited by the finite ion beam size and the metal sputtering process. Also, the unavoidable ion implantation by the ion beam degrades the quality of the metal. In addition to these limitations in the FIB fabrication, there are challenges in placing optically-active materials at the bottom of a very narrow metal trench, where the intensity of the cavity modes is highest. A different fabrication method to overcome these problems is required.

4.3 Reverse Image Mold (RIM) Method for Fabrication of Metallic Trench Cavities

Since the consequences of the FIB process may limit performance of our cavities, we have adopted the a different fabrication approach that both deterministically placing and orienting cavities while placing optical emitters at locations high field confinement. A high-spatial resolution ‘reverse image mold’ was first formed using electron beam lithography, and then the metal cavity was formed around the mold using a version of template-stripping. A schematic diagram of the process is shown in Figure 4-5. A layer of XR 1541 electron-beam (E-beam) resist, 150 nm thick, was deposited on top of an oxidized Si wafer. XR 1541 is a high resolution negative resist that is converted into a silicon-oxide containing dielectric material under electron beam irradiation with a 100kV Elionix F-7000 e-beam lithography system [Ref. 38]. The result of this lithography step is a set of 150nm tall, 30nm wide dielectric ridges, as shown in Figure 4-6 (a) and (b). These dimensions will define the width and depth of the trench cavities. These dielectric ridges serve as the ‘reverse image molds’ or templates for our metallic trench cavities.

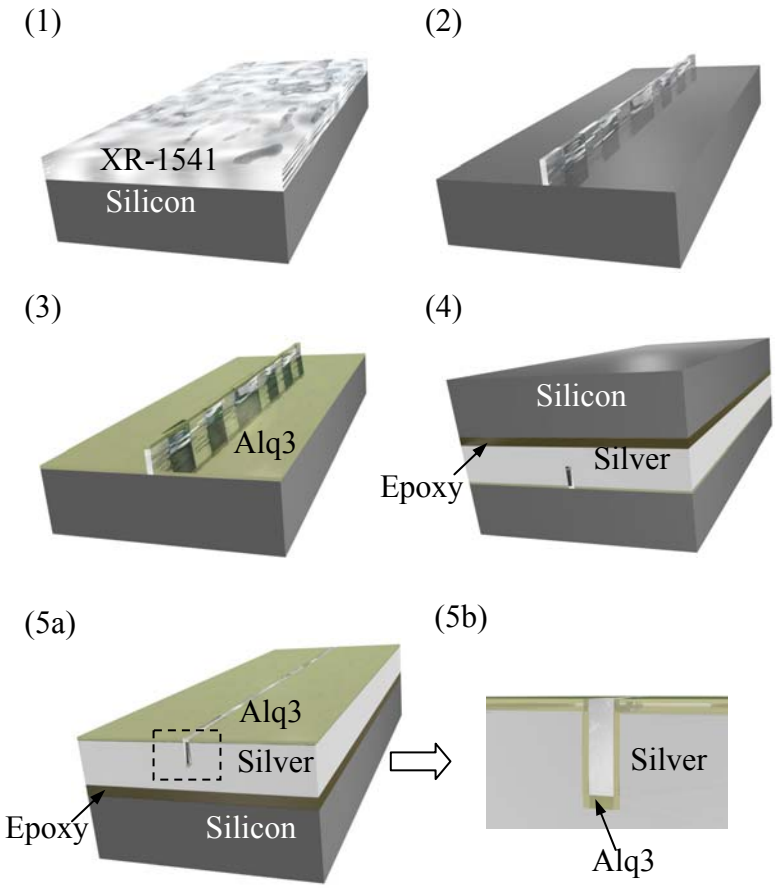

Fig. 4-5: Process flow for fabricating template stripped trench cavities. Step (1): spin coat XR-1541 onto a clean, smooth silicon wafer. Step (2): pattern XR with e-beam lithography. Step (3): evaporate 5nm of Alq3 upon the template. Step (4): sputter coat 500nm of silver onto the template, and attach exposed surface of the silver layer to a wafer piece using epoxy. Step (5a): peel off the original silicon substrate and flip the chip over. Step (5b) cross-section view of the final trench. (Region enclosed by a dashed line in step (5a)).

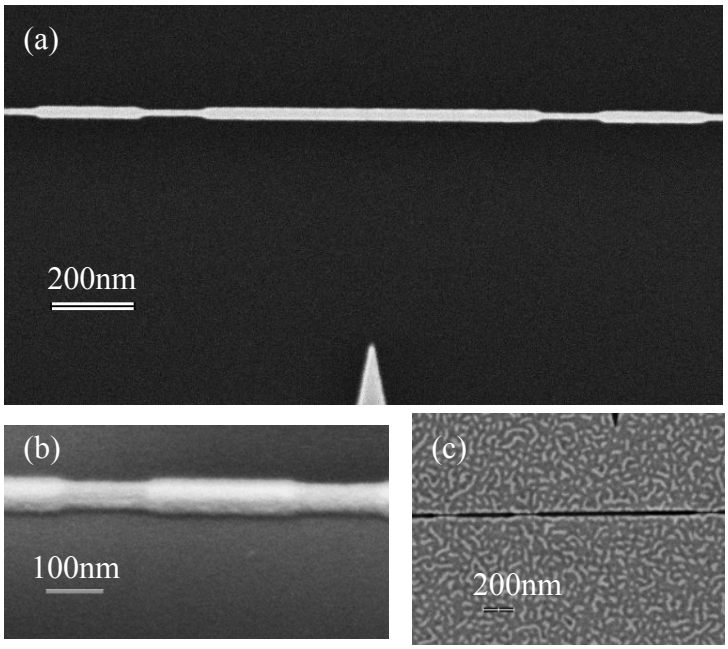

Fig. 4-6: SEM images of: (a) top-down view of the RIM, (b) 40° angled view of the RIM and (c) top-down view of the fabricated trench

We subsequently deposited 5nm of organic molecular emitter tris(8-hydroxyquinolinato) -aluminum (Alq_3) onto the template by thermal evaporation followed by sputter-coating a 2 nm Al_2O_3 protective layer and 500 nm of silver. The silver layer will serve as the actual cavity. Similar to the template stripping method introduced in Chapter 3, silicon "handles" were then anchored onto the silver surface with epoxy (EPO-TEK 377, Epoxy Technologies) which was cured at 150°C for 3 hours. The fabricated metallic cavities were removed from the templates by sliding the blade of a razor under the edge of the silicon handle. This modification of the template stripping process ensures that the interior walls of the silver trench have sub-nanometer

roughness. A top-down scanning electron microscope (SEM) image of a fabricated trench cavity is shown in Figure 4-6 (c). An important feature of this process is apparent from the schematic view of the cavity cross-section, shown in Figure 4-5 (5b), the organic emitter, Alq_3, is embedded deep into the trench, co-located with the high field region of the cavity. This ensures good overlap of the emitters with the cavity modes as we will show the simulated field distribution later in this article.

With this method, a series of devices with various dimensions in the trench axis (y axis in Figure 4-1) were fabricated. Trench cavities with lattice constant a = 425, 450, 475 and 500nm was made within one round of process and located nearby on the substrate. The devices which produce the data below have a lithography dose of 4200μC/cm^2, and the typical width and depth are as described in former paragraphs.

4.4 Simulation and PL Measurement Results for RIM Trench Cavities

To verify the performance of these fabricated cavities, finite difference time domain (FDTD) simulations were carried out. According to the SEM and ellipsometer measurements, the RIM has a rounded square shape with a refractive index of ~1.4. The wider part of the RIM is ~30nm wide at the bottom of the RIM and the height is ~150nm defined by the thickness of the spun resist. However, the thinner part, which is

about 15nm wide, has a height of ~110nm, lower than the original resist thickness. This indicates a great drawback of this process; as the dimension of the geometry is close to the resolution of the lithography technique, the resist profile is strongly dependent on the dose and other exposure conditions. All the dimensions we provide here are based on the ones that worked the best among all the devices fabricated with various electron dosages.

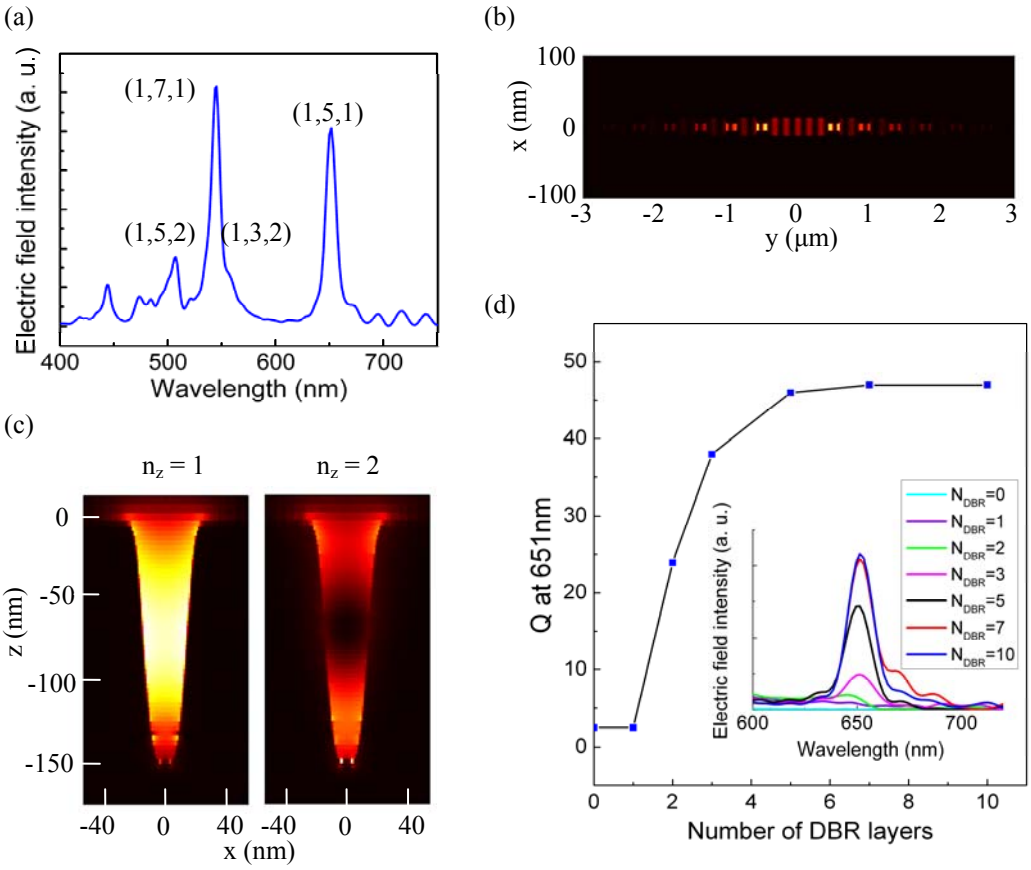

Fig. 4-7: FDTD simulation on trench cavities including: (a) the simulated spectrum of a cavity with a = 425nm, (b) in-plane electric field distribution recorded by a monitor 70nm below the top metal surface, (c) cross-section

Fig. 4-7 (Continued): electric field distribution for modes with $n_z = 1$ and $n_z = 2$ and (d) Q and mode spectra dependence on number of DBR layers for the (1,1,5) mode.

The simulated structure was built based on all the parameters provided above. In the simulation, an electric dipole source with a broadband radiation of 500-700nm was placed into the center of the trench, 30nm above bottom of the trench and polarized across the trench (x-direction in Figure 4-1(a)) with a 15 degree clockwise tilt in the x-y plane. The simulation calculates field response to the dipole emitted electric pulse (~15fs long in time) for 300fs. The electric field intensity was then recorded and the frequency response of the device can be analyzed by the Fourier transform of the time dependent electric field intensity.

The simulated spectrum is shown in Figure 4-7. (a). A few resonances can be seen in the figure. The quality factors (Qs) of these resonances can be estimated from the line-widths of these peaks to be ~30-50. Comparing the spectrum with the frequency-dependent electric field distribution allows us to identify these transitions in turns of their quantum numbers in each dimension. These numbers are labeled in Figure 4-7 (a) above each peak in a (n_x, n_y, n_z) form; the axes are defined as previously shown in Figure 4-1 (a). Since the width of the trench is much less than half of the operational

wavelength (vacuum wavelength ~600nm), only the fundamental mode in the x directions is supported. In the z axis, limited by the trench depth, only two orders of modes are observed. The electric field distributions of the two modes are shown in Figure 4-7 (b) (similar to mode number n=1,2 in [Ref. 35]).

Figure 4-7 (b)-left and (c) shows top-down and cross-sectional views of the field distribution of the (1,5,1) mode at 651nm. A few observations should be made. First, the cross-section view shows strong field density at the bottom of the trench, as discussed in previous paragraphs. This geometry is capable of concentrating the field into a 10^{-4} $(\lambda)^2$ cross-area. Second, the major electric field component is polarized in the x (cross-trench) direction. This is not shown in the figure but will be used to compare with the measurement results later in this article. Last, the field travels in the trench waveguides and gets reflected by the DBRs showing a Fabry-Perot like interference pattern in the y axis.

In order to understand the effect of the DBRs on the cavity, a series of simulations were performed. We varied the number of DBR layers on each side and monitored the corresponding change of cavity Q. The dependence of Q on the (1,5,1) mode on numbers of DBR layers (N_{DBR}) is shown in Figure 4-7 (d). The quality factor of the mode plateaus at Q ~ 50 from when n is greater than 5. When n decreases, a clear decrease in Q can be seen and the resonance is not well defined when $N_{DBR} < 1$. These

results demonstrate that the DBRs do help in confining the field and we can control the confinement of the cavity by adjusting the number of DBR layers, but the effect is much weaker than is observed for dielectric DBRs [Ref. 39]. First, the strong propagation loss in a plasmonic waveguides prevents long distance interference between the reflected waves. This fact in a great sense limits the performance of the device. Second, the same observation indicates that we need enough reflection from each layer to provide enough confinement over the field. But the propagation loss will at the same time lead to a higher mode mismatch and greater scattering loss at each reflective interface, hence limiting the Q of the cavities.

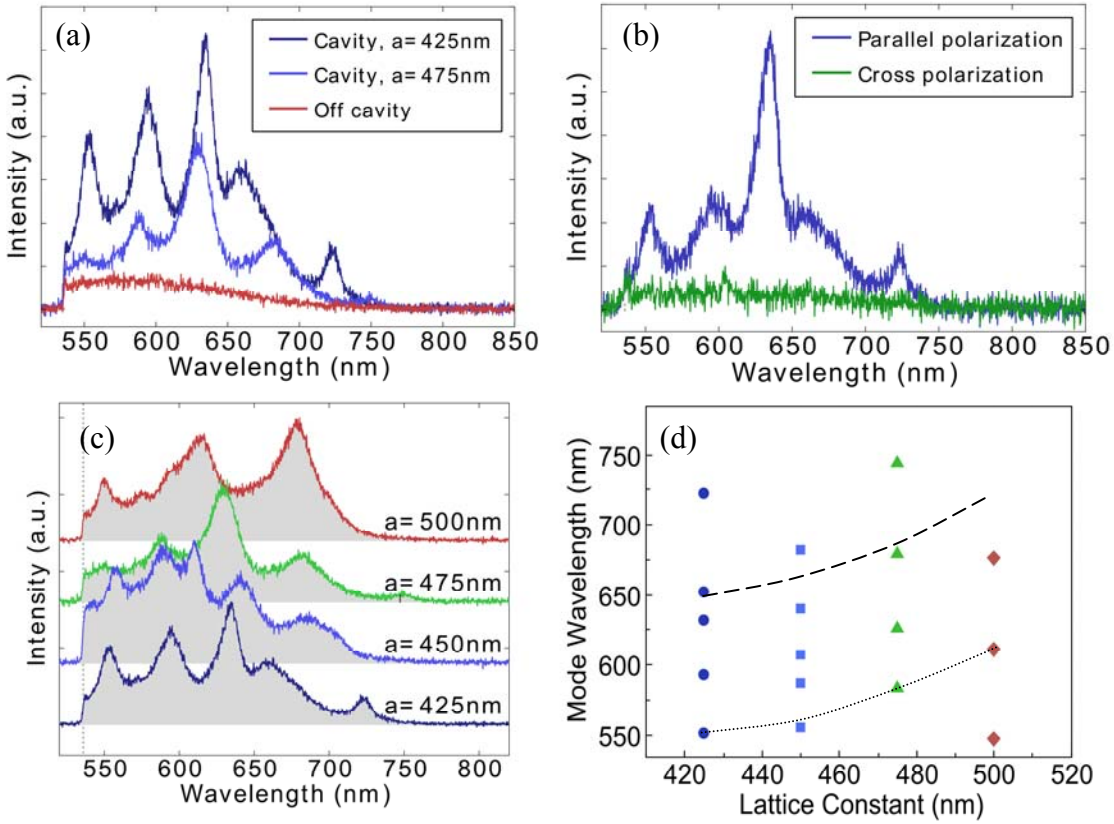

Fig. 4-8: (a) PL spectra measured on and off cavities. (b) Polarization

Fig. 4-8 (Continued): dependence of PL spectrum of a trench cavity. (c) Normalized PL spectra of trench cavities with various grating pitches and (d) dependence of resonant wavelengths on lattice constant. The dashed line indicates simulated peak wavelength of the (1,5,1) mode and the doted line indicates the (1,7,1) mode.

The "RIM"-fabricated structure was characterized with micro-photoluminescence measurements. A temporally pulsed beam at 455nm wavelength from a frequency-doubled Ti:sapphire laser system was directed through a 100x, 0.9 numerical aperture objective onto the trench cavities containing Alq_3. Luminescence from the excited molecules was then collected by the same objective. The collected signal was analyzed by a grating spectrometer with liquid-nitrogen cooled CCD array.

As shown in Figure 4-8 (a), the excited Alq_3 on the un-patterned metal surface gives a broad band fluorescence spectrum over 500-700nm (off-cavity trace of the figure). By comparison, the fluorescence spectrum of Alq_3 embedded in the trench cavity is strongly modified by the cavity structure (on-cavity trace in Figure 4-8 (a)). Distinct cavity modes with quality factors ranging from 40 to 50 are observed. These resonant modes are polarized in the y direction, perpendicular to the trench direction, and so is the far field scattering toward positive z direction which is collected by the

objective. Therefore, as shown in Figure 4-8 (b), we can isolate the emission associated with molecules coupled to the trench plasmonic modes from random spontaneous emission using the polarization of the PL spectrum. By comparing the integrated intensity of the parallel and cross polarized signals, we conclude that over 90 percent of the total signal is from photons coupled to the guiding modes in the trench. Figure 4-8 (c) shows PL spectra from trench cavities with various lattice constants (a = 425 nm – 500 nm). A clear shift of the cavity modes is observed for different cavity dimensions. Tracking the mode wavelength with the pitch of the plasmonic cavity, as shown in Figure 4-8 (d), indicates that the resonant condition scales with the pitch of the cavities. This shift can be characterized by comparing the experimental and simulated data. The capability to deterministically shift the cavity mode enables spectrally selective enhancement of the emission of the organic dye. This would be useful, for example, to study the difference in plasmon-matter interaction of molecules in and out of resonance with the cavity mode, as has been demonstrated in dielectric optical microcavities [Ref. 31]. In plasmonic structures, such deterministic control over low Q (broadband) resonances has been shown, and continuous tuning of non-deterministic high Q resonances has been achieved [Ref. 40]. However, the low Q and/or non-deterministic nature of these previous works limited their application to cQED studies [Ref. 41]. In addition, since the cavity design presented here builds upon a trench waveguide, there

is a natural way to join cavities to waveguides to couple together spatially separate cavities.

4.5 Conclusions

In summary, we demonstrated a cavity design which can be lithographically patterned to provide relatively high Q for plasmonic resonators. Simulations show promising resonance with Q of around 30-50 which can be altered by the geometry of the cavity. In order to overcome all the drawbacks in using FIB to fabricate these cavities, we developed a reversed image mold (RIM) to fabricate these cavities. This technique allows us to have great control over the orientation and dimension of the device. The method also enables incorporation of evaporated organic dyes being inserted into the hot spot of the cavities, allowing us to probe the cavity characteristics by the luminescence spectrum of the dye. Photo-luminescence measurements show distinct cavity modes with relatively high Q among lithographic plasmonic cavities which the resonant frequencies can be altered by patterning.

The limitations of the RIM technique include the fact that the mold profile is highly dependent on the electron beam dose; hence the profile may be very different if one tries to alter the geometry of the trench (e.g. varied width, or curvature of the waveguide, etc.) The method also somewhat limits the type of emitter that can be

applied and possibly inflicts fabrication damage onto organic emitters. Despite these drawbacks, the reverse-image-mold technique can be applied to similar trench waveguide based plasmonic devices or inspire similar geometries.

Chapter 5
Metal-dielectric Hybrid Plasmonic Cavities

5.1 Introduction

In the previous chapter, we discussed cavities formed by periodically modified trench waveguides. However, this trench structure cannot take full advantage of the distributed Bragg reflectors (DBRs), because 1. strong field penetration into the metal in trench waveguides reduces the propagation length in the waveguides, 2. strong scattering losses by the shaped metal structures introduces extra loss at each reflection interfaces, and 3. the performance of the structure is very sensitive to the detailed profile of the metal surfaces, which is not well controlled.

All these shortcomings can be attributed to two facts: first, most state-of-the-art nano-fabrication techniques cannot be directly applied to noble metals. For instance, there are no efficient reactive ion etch processes for metals. Additionally, metals cannot be processed at elevated temperatures, which are necessary for all types of lithography, due to grain formation. Second, the plasmonic resonances are very sensitive to

variations of metal surface morphology. A slight change of metal geometry and smoothness may produce very different resonance behavior.

A possible solution for the problems above is to combine nanofabricated dielectric structures with ultra-smooth metals surfaces, and to control the plasmonic resonances by shaping the dielectrics. A nice way to combine these two was presented in Xiang Zhang's group at the University of California, Berkley, which demonstrated the idea of hybridizing metal surface with dielectric structures to form high quality plasmonic cavities [Ref. 22]. This work opened up the possibility of combining dielectric photonic structures with surface plasmon resonances to design and fabricate high quality plasmonic cavities, plasmonic waveguides and integrated plasmonic circuits [Ref. 33, 42].

This idea of creating "hybrid" plasmons by mode mixing between photonic modes in dielectric structures and surface plasmon polaritons enables us to apply well-developed dielectric fabrication techniques and photonic device designs to plasmonic cavities. Furthermore, it is also possible to couple bulk or quantum-confined semiconductor emitters to plasmonic devices. To demonstrate these advantages, we looked into two commonly found photonic cavity geometries: photonic crystals and optical microdisks. In Section 5.2-5.5, I will present simulation results on forming a high Q plasmonic crystal cavity by combining dielectric photonic crystals with a metal

surface. I will discuss how to use a developed photonic band-gap device to create plasmonic band-gap. In Section 5.6-5.9, I will demonstrate plasmonic cavities designed to couple to self-assembled quantum dots (SAQD) embedded in epitaxial grown semiconductors.

5.2 2-D Plasmonic Crystals

The photonic energy gap generated by the periodic variation of refractive index in structures known as photonic crystals has been applied for the design of various photonic devices [Ref. 43, 44]. Among all these applications, high quality, low mode volume nanocavities formed by intentionally introduced defects in photonic band gap structures have enabled many cavity quantum electro-dynamics (cQED) studies [Ref. 31, 45]. By hybridizing dielectric modes with surface plasmon polaritons, we can take advantage of the well studied photonic crystals formed by dielectric structures and try to combine them with metallic surfaces.

Several works on creating plasmonic crystals by coupling dielectric photonic crystals to surface plasmon have been presented [Ref. 46, 47].However, devices based on 2D plasmonic band gap have not been demonstrated for the following reasons. First, most photonic crystals made in semiconductor slabs create a large band gap for transverse electric (TE) polarized field but not for the transverse magnetic (TM) modes,

which have a similar polarization to the surface plasmons. Second, fabricating nano-scaled structures upon a metal surface without damaging the surface is challenging.

In this work, we studied how a 2-D plasmonic crystal can be formed and the performance of a plasmonic cavity based the structure. A schematic drawing of the structure is shown in Figure 5-1. The photonic crystal (consider $d = \infty$ in Figure 5-1) used in geometry is formed by hexagonally arranged high index circular rods embedded within low index matrix; such a structure has been shown to provide sufficient TM band gaps [Ref. 48]. The finite difference time domain (FDTD) calculated photonic band structure is shown in Figure 5-2. The simulated structure contains high index dielectric rods with a refractive index of 2.5 embedded in an air matrix. The material parameters are chosen to be close to the refractive index of high index transparent dielectrics such as GaN, TiO2 or diamond. These dielectric rods are arranged into a hexagonal crystalline structure with a lattice constant (a) of 250nm. The radius of these rods (r) is 70nm (r=0.28a) and the length (h) is 250nm to eliminate higher order guiding modes around the frequency of interest.

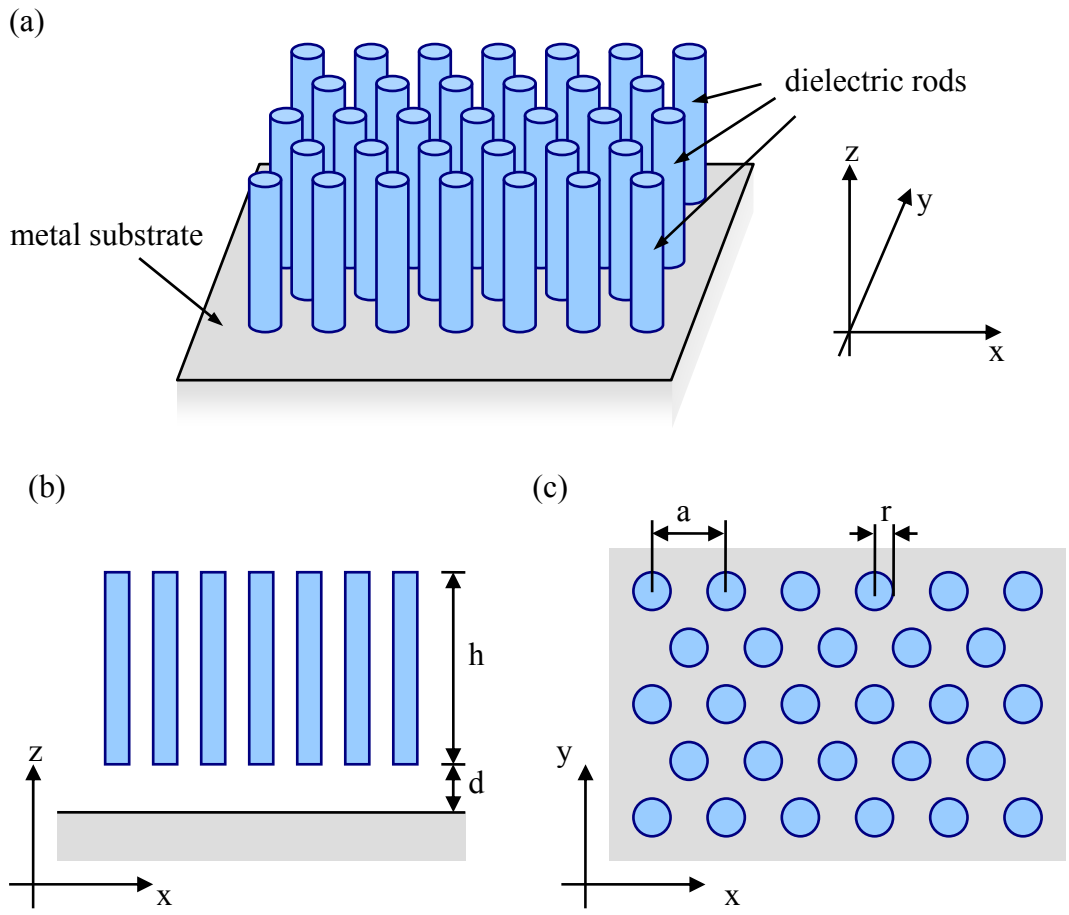

Fig. 5-1: Schematic view of the plasmonic crystal studied in this work including (a) an angled view, (b) a cross-section view and (c) a top-down view. The blue rods are dielectric structures and the gray square is made of metal.

A few photonic bands are shown in the simulated spectra within the frequency range of interest in Figure 5-2. By analyzing the magnitude of the out-of-plane electric field component, one can distinguish between TE and TM modes, as labeled in Figure 5-2. A clear TM band gap from 511THz to 557THz is can be found in the figure. Further investigation into the electric field distribution of the two TM modes defining

the fundamental band gap, labeled as TM_1 and TM_2 in Figure 5-2, one can find signatures similar to how an electronic band gap is formed in atomic crystals. As the cross-sectional field distribution of both TM_1 and TM_2 modes, show in Figure 5-3, agrees with that of a fundamental TM waveguide mode, the in-plane field distributions act as standing waves scattered by the rods. At the band edges, periods of the standing waves equal the lattice plane distances of the photonic crystal. The two-fold degeneracy of the standing wave is then broken by the periodic structures as the lower energy band tends to concentrate in the high index rods and the higher energy one tends to stay in air. These simulated electric field distributions are shown in Figure 5-3.

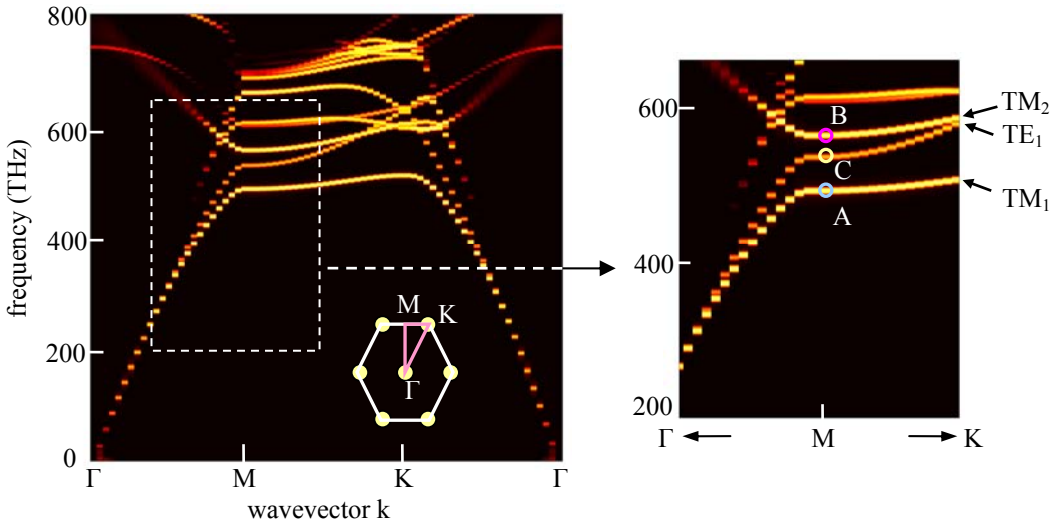

Fig. 5-2: Simulated band structure of the photonic crystal structure used in this work with a = 250nm, r = 70nm and h = 250nm. A zoomed in view of the plot (area enclosed in white dashed lines) is shown in the right. Three lowest energy

Fig. 5-2 (Continued): bands are identified and labeled as TM or TE bands on the right of the figure. Three points labeled as A, B and C are the conditions used to create field distributions shown in Figure 4-8.

(a)

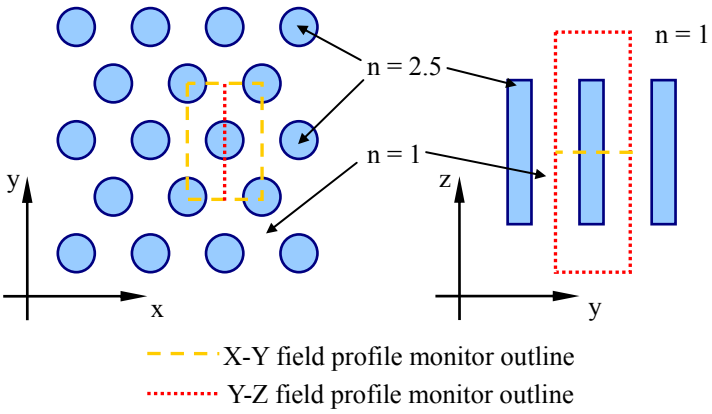

(b)

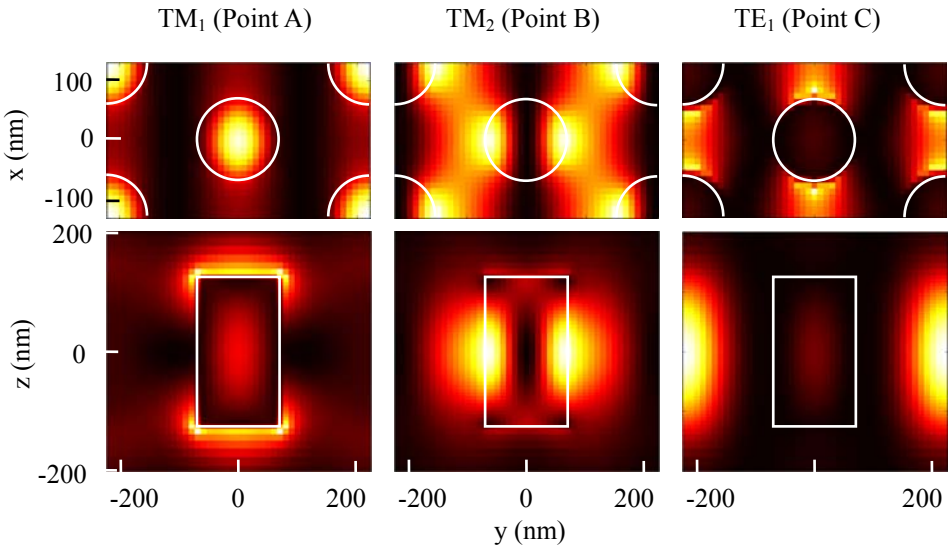

Fig. 5-3: (a) A schematic view of orientations of the field profile monitor placed in the photonic crystal structures. (b) X-Y and Y-Z electric field distribution of TM_1, TM_2 and TE_1 bands near the M point (A, B and C points in Figure 5-2). The white lines shown material outline. Definition of the axis is the same as in Figure 5-1.

As a metal substrate (silver, modeled with optical parameters measured by Johnson and Christy) approaches one side of the photonic crystal (d in Figure 5-1 decreases), the TM modes start to hybridize with surface plasmon modes, hence the effective index of the modes increases. As a result, the frequencies of all TM modes decrease as the metal nears the crystal (Figure 5-4.) A similar effect has been demonstrated in studies on 1D hybrid plasmonic crystals [Ref. 47]. The exact frequency shift can be estimated by the wave number difference between the waveguiding mode in the original dielectric plate and the surface plasmon mode in the metallic structure. Because the electric field in TM_1 is more concentrated in the high index rods, it experiences a stronger effective index increase with the presence of the metal layer, and hence the amount of mode shifting in TM_1 is larger than in TM_2. This effect increases the TM band gap as the metal approaches.

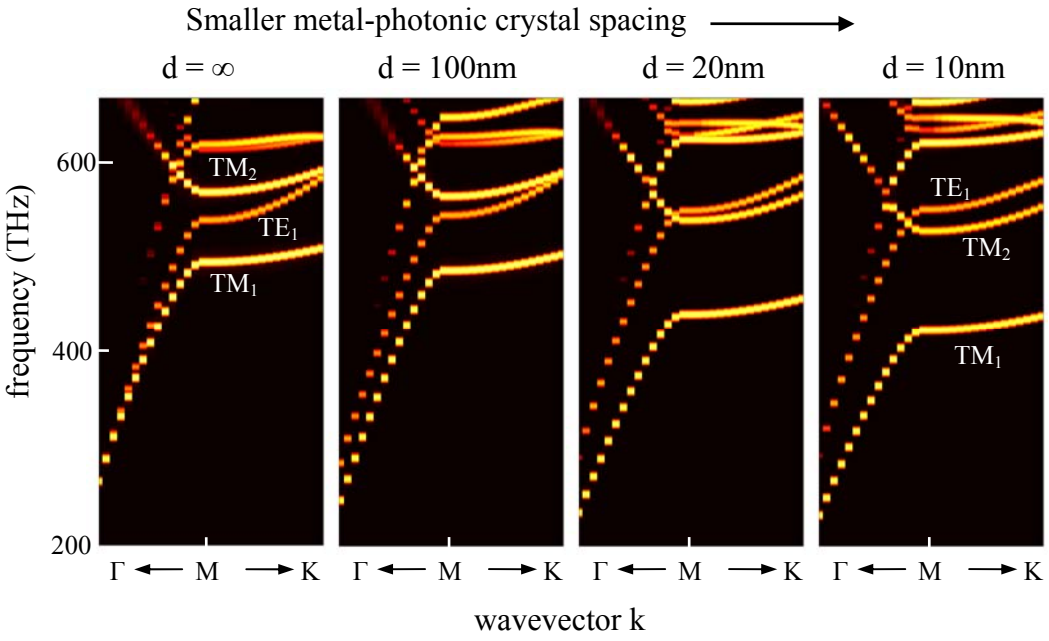

Fig. 5-4: Changing of the photonic band structure as a metal surface approaches the photonic crystal.

A plasmonic crystal is formed when the metal-dielectric spacing is significantly smaller than inverse of the exponential decay constant of the surface plasmon mode (tens to 100 nm in our case, wavelength dependent). The plasmonic band-gap in the simulated structure with d =10 nm ranges around 441THz to 516THz (581nm to 680nm in wavelength). The full band structure of the plasmonic crystal is shown in Figure 5-5 (a).

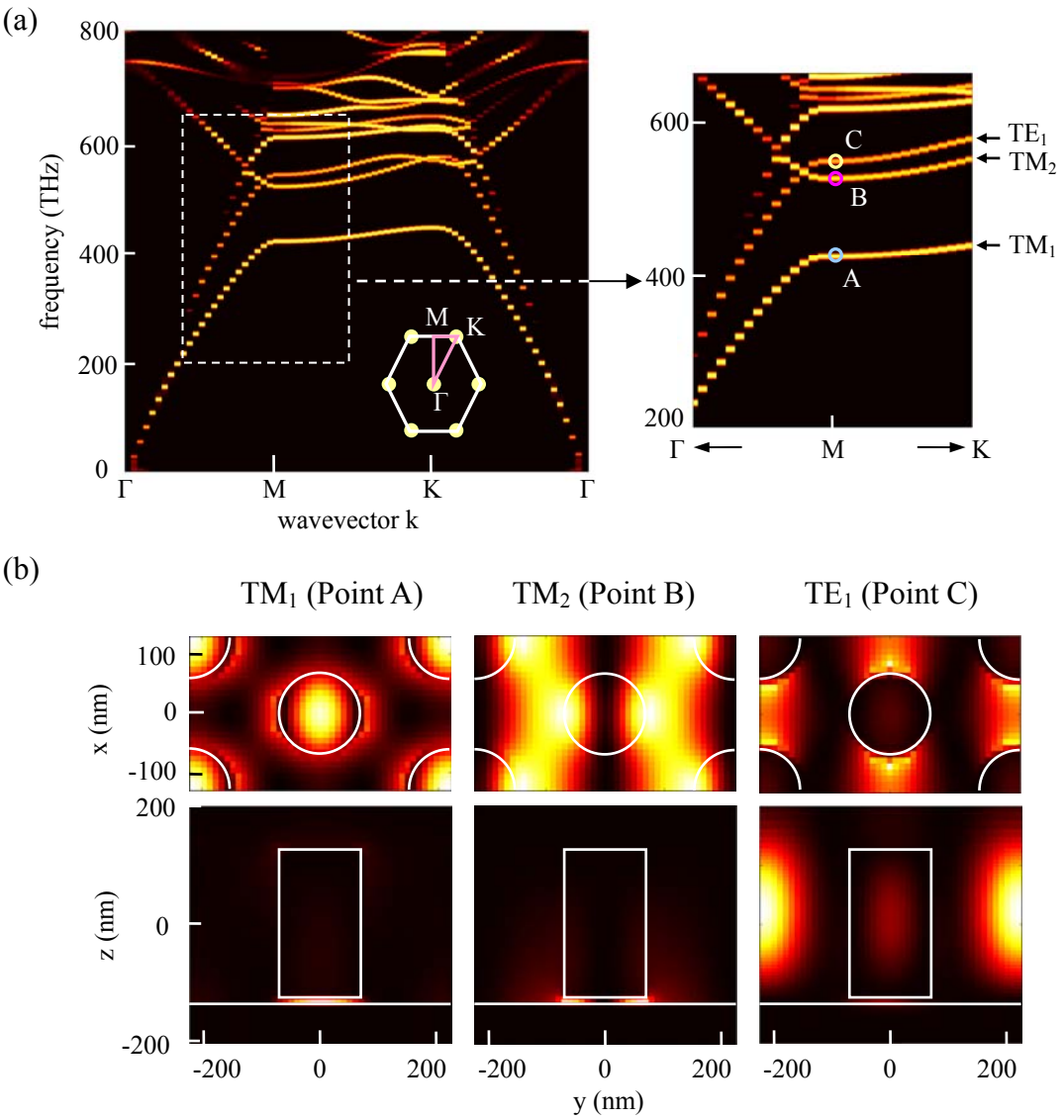

Fig. 5-5: (a) Simulated band structure of the plasmonic crystal structure used in this work with a = 250nm, r = 70nm, h = 250nm and d = 10nm. A zoomed in view of the plot (area enclosed in white dashed lines) is shown in the right. (b) X-Y and Y-Z electric field distribution of TM_1, TM_2 and TE_1 bands near the M point (A, B and C points in (a)).

This hybridization between TM modes and surface plasmons can be further

explored by comparing the field distribution of the hybrid plasmonic crystal to the original photonic crystal. Although the x-y field distributions shown in Figure 5-5 (b) remain similar to those without metal in Figure 5-3, the z field profiles of the TM modes are strongly altered. The hybridization draws the field onto surface of the metal and concentrates the field into the small gap between metal and the high index material. However, the TE mode cannot hybridize with surface plasmon polaritons owing to the mismatch in polarization. Therefore, the field distribution of the TE mode is not significantly modified.

5.3 2-D Plasmonic Crystal Cavities

To create a cavity from a plasmonic band gap structure, we introduced a defect into the center of the plasmonic crystal. In previous photonic crystal cavities made of dielectric rods, the defect is often induced by modifying only one lattice site to achieve a small mode volume [Ref. 48, 49]. A confined mode needs to fulfill two conditions: 1.the frequency of the mode needs to lie within the band-gap of the photonic crystal and 2. the confined field must form constructive interference while traveling within the defect (the resonance condition of the defect). However, very few modes can fulfill the resonant condition in a small defect like a single dielectric rod with a diameter of ~200nm. In order to simplify this design criterion and more effectively make use of the

band gap, a linear 3 (L3) defect-like cavity design is used in this structure. The defect in this cavity is formed by connecting three enlarged dielectric rods, as shown in Figure 5-6 (a).

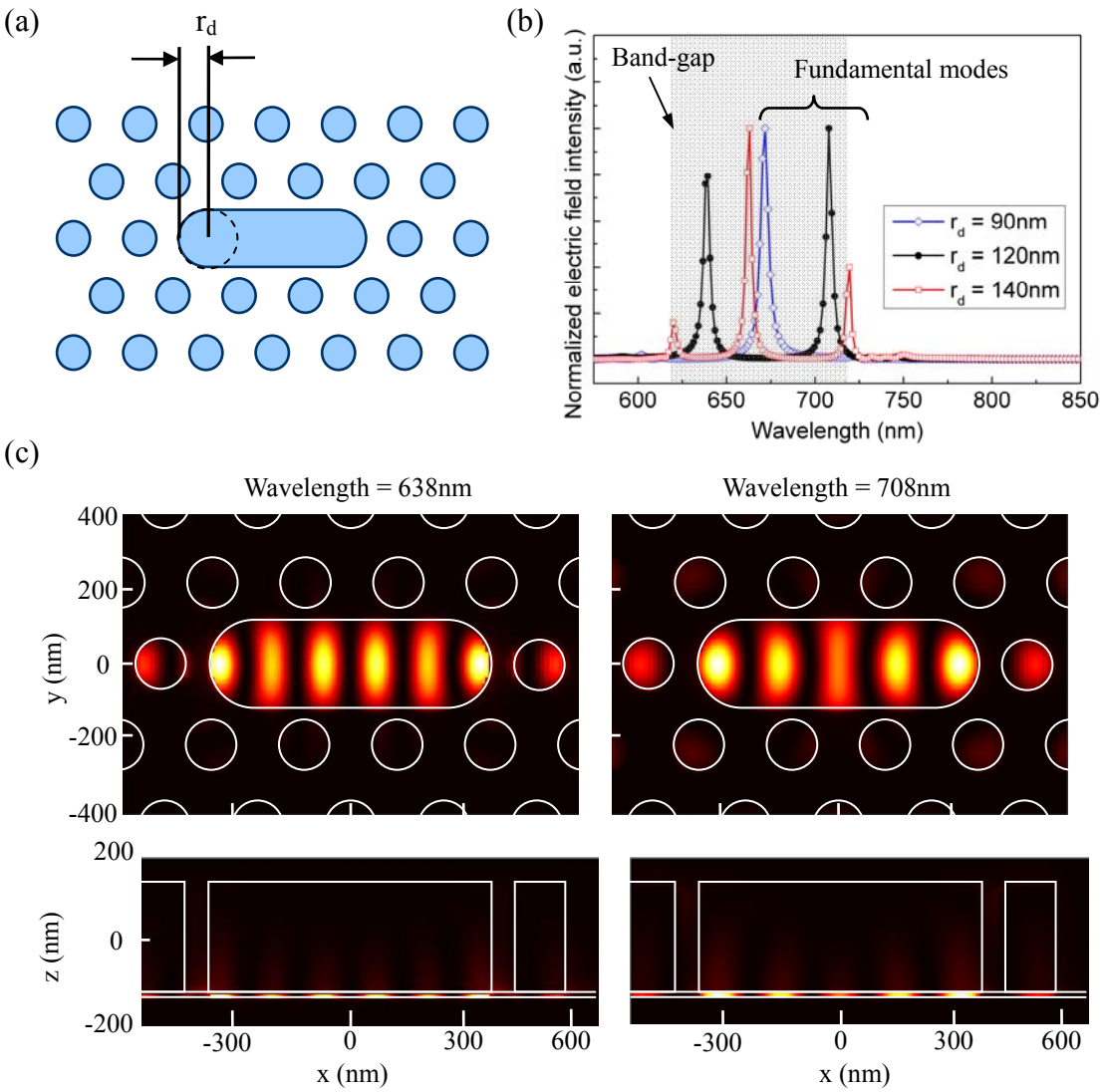

Fig. 5-6: (a) A schematic top-down view of the plasmonic crystal cavity. The defect is formed by connecting three rods with increased radius r_d and the defect is enclosed by n layers of rods on each side. (b) Simulated spectra of cavities with r_d = 100, 120 and 140nm. (c) Electric field distribution of the two modes

Fig. 5-6 (Continued): for the cavity with r_d = 120nm. The white lines show material outlines.

The defect is surrounded by 5 layers of dielectric rods with radius r on each side to form the photonic crystal barriers. The whole structure forms a 13 by 11 hexagonal rod array. Below this photonic crystal is a low index spacer/emitter layer with a refractive index of 1.4. Adding this spacer layer into the plasmonic crystal shifted the band-gap to 417-483THz (621-719nm in wavelength). Under the spacer layer is the silver substrate modeled by optical parameters measured by Johnson and Christy [Ref. 28]. A few electric dipoles polarized perpendicularly to the metal surface are embedded near the center of the low index spacer layer. The simulated spectrum is shown in Figure 5-6 (b). For the cavity with r_d = 120nm, two distinct cavity modes with Q = 207 and 197 located at 708 nm (fundamental) and 638 nm (2^{nd} order) can be observed. Peak wavelengths of these modes can be shifted by changing r_d. The position of the band-gap can be demonstrated with this mode shifting. As the defect size r_d increases from 120nm to 140nm (see Figure 5-6b), both modes shift toward high wavelengths and a higher order resonance can be observed on the left of the spectrum as it shifts into the band-gap. However, as the defect size decreases from 120nm to 90nm, the 2^{nd} order mode shifts significantly out of the range of the band-gap and can no longer be observed in the

spectrum.

Electric field distributions of both modes of the cavity with r_d = 120nm are plotted as Figure 5-6 (c), showing highly a concentrated field within the low index spacer layer. The mode volume of the fundamental mode at 708nm can then be estimated by the formula shown in equation 1-3, Chapter 1, as ~2.4×10^{-3} μm^3, which is roughly 1.9×10^{-2} $(\lambda/n)^3$. The Q/V ratio of such a cavity is comparable to a cavity with Q ~ 32000 and V ~ 1 λ^3.

How much can we enhance emission from a dipole embedded in this cavity? The answer can be estimated by further calculations. Figure 5-7 (a) shows the power radiation spectrum of a dipole located near the field maximum of the cavity mode (labeled near-field). The z-position of dipole is located at the center of the spacer layer and the x-y position is as shown in Figure 5-7 (a). The spectrum is normalized to the power radiation from the same dipole embedded in a bulk dielectric with a refractive index of 1.4. The Purcell factor of the cavity mode can be extracted as the peak value of a power spectrum to be ~ 410 at 708nm, which is the peak of the fundamental mode.

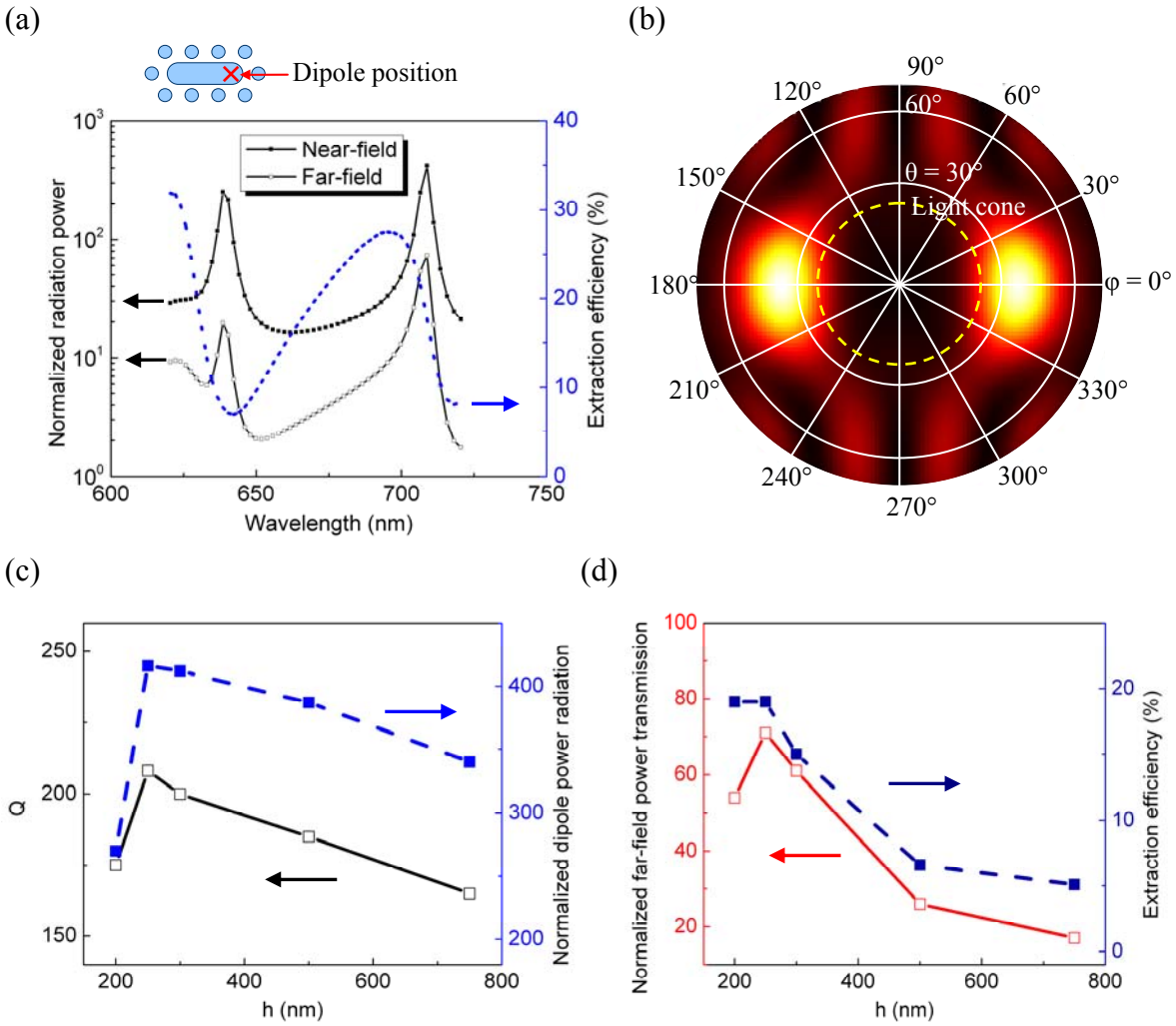

Fig. 5-7: (a) Near-field and far-field power spectrum from a dipole located near the high intensity field of the mode at 708nm for a plasmonic crystal cavity with rd = 120nm and h = 250nm. The blue dotted line shows the extraction efficiency spectrum which is a result of dividing the far-field spectrum by the near-field spectrum. (b) Far-field transformation pattern of the mode at 708nm. (c) Q and peak near-field power radiation versus h. (d) Far-field peak power radiation and extraction efficiency versus h.

In addition to enhancing the dipole radiation rate, another important function for a cavity is to increase directional photon extraction for various purposes. In this case, we study the far-field extraction efficiency within a numerical aperture of 0.9 from such a device by simulating power transmission through a plane roughly one wavelength (700nm) above the cavity, the power transmission spectrum which is normalized the same way as the dipole radiation power is also shown in Figure 5-7(a) (labeled as far-field). Dividing the transmission power by the dipole radiation power leads to the extraction efficiency spectrum, as the blue dotted curve in Figure 5-7 (a). Field components which lead to this radiation can be analyzed by the far-field transformation of the mode profile shown in Figure 5-7 (b). The light-cone, labeled as the yellow dashed circle in Figure 5-7 (b), determines the fields that can leave the high-index rods/air interface and contribute to far-field transmission. One can find a significant amount of the field located within the light-cone in the plot. Radiation loss caused by these components is one of the mechanisms which reduce Q of the cavity. Therefore, one of the most important design criteria for dielectric photonic crystal cavities is to minimize far-field radiation within the light cone [Ref. 50]. However, in a plasmonic cavity which has inherently high absorption loss, this radiation is essential for sufficient external quantum efficiency.

We can further explore this behavior by comparing the power radiation rate and

extraction efficiency for various geometries. Figure 5-7 (c) shows the dependence of Q and dipole power radiation at the peak of the modes on the height of the dielectric rods (h). For different geometries, Q varies between 160 and 200 and this minor change in Q reflects the change in the radiation rate enhancement of the cavity modes. However, the far-field power transmission follows a different trend. Figure 5-7 (d) shows far-field power transmission and extraction efficiency at the peak of the modes with the same variation in h. Although high radiation enhancement ranging from 250 to 400 can be found in all cavities shown in the plot, the extraction efficiency is relatively low. This low efficiency strongly determines the intensity of far-field radiation power. Compare cavities with h = 200nm and 750nm: the dipole radiation power is slightly higher in the 750nm cavity but the extraction efficiency drops from ~20% to ~5%. The normalized far-field power transmission therefore drops from ~54 to ~17. The maximum far-field power transmission occurs at h~250nm and the extraction efficiency is ~20%. This number is greatly improved from the nanowire cavities described in Chapter 3 but still relatively low compared to well-designed dielectric cavities.

5.4 2-D Plasmonic Crystal Cavities - Conclusions and Outlooks

In Section 5.2 and 5.3, we demonstrated the idea of forming high quality

plasmonic cavities with 2-D plasmonic crystals. FDTD simulations demonstrated that the plasmonic band-gap formed by the plasmonic crystals can be used to enhance field confinement at the metal surface. Resonance modes with Q ~200 and V on the order of $10^{-3}\ \lambda^3$ were observed in the simulated results.

Studying radiation from a dipole embedded in such a structure provides insights on the capability and design criteria for plasmonic cavities. A Purcell factor over 400 is estimated by the calculation and the spectral tolerance for maintaining high enhancement is over a few nano-meters due to the relatively low Q compared to dielectric cavities. However, performance of the cavities is limited by metal-caused high absorption loss. The total photon emission from the cavity can be strongly constrained by the low extraction efficiency. Therefore, instead of pursuing high Q, balancing the enhancement and extraction efficiency is the key to optimizing the performance of these cavities.

In this work, we have only discussed using the band-gap of the plasmonic crystals to confine fields. Further studies on the scattering behavior and the band structure in plasmonic crystals can give us more insight into how the performance of the cavities can be modified by altering structural parameters. These concepts may also help in designing plasmonic waveguides or antennas with plasmonic crystals. Integration of multiple devices within a wide area of plasmonic crystal arrays may also be realized to

enable new applications with plasmonics.

Further work on developing a fabrication method to realize these designs is also important. Fabrication techniques using either GaN or diamond on silver surface is currently under development. Some discussion regarding these methods will be discussed in appendix D.

5.5 Introduction to Plasmonic Microdisks for Coupling to Self-assembled Quantum Dots

In previous sections, we presented hybrid plasmonic cavity design that allows us precise control over cavity characteristics. However, the types of emitters applied into these cavities are limited by the fabrication process and field distribution within the cavity. In the following work, we introduce a cavity design based on a specific kind of emitter – self-assembled quantum dots (SAQDs).

A quantum dot (QD) is a heterostructure which can confine carriers in all three spatial dimensions with length scales comparable to or less than the de Broglie wavelength of the carriers. This confinement breaks continuous electronic states into discrete states. These quantized states can be used as a trap for single electron or as a source for single photons [Ref. 51].

In principle, all quantum dots are self-assembled. However, the term

self-assembled quantum dot (SAQD) used here is specific to quantum dots which are formed by strain-induced local variation in epitaxial grown semiconductor stacks [Ref. 12]. Owing to their narrow line width, long term stability, and compatibility with semiconductor fabrication techniques, these quantum dots have played an important role in the demonstration of many quantum optical phenomena [Ref. 33, 52].

Here we explore the possibility of coupling SAQDs to plasmonic cavities. Similar work to enhance photon collection from SAQDs with plasmonic antennas has been published [Ref. 53]. However, these low Q antennas provide limited spectral selectivity over quantum dot transitions. Therefore, our work focuses on designing plasmonic cavities with sufficient Q for better control over the frequency response of this interaction.

5.6 InP SAQDs in Microdisk Cavities

As mentioned in the previous section, a major advantage of SAQDs is that the epitaxially grown semiconductor substrate can be designed to match fabrication requirements for high quality photonic devices. In this work, the substrate can be grown as a modified structure that is good for fabricating suspended cavity structures including microdisk cavities with high Q whispering gallery modes (WGMs) which will be introduced in this chapter. These high Q cavities are good candidates for

modifying emission from SAQDs and could be inspiring for design plasmonic cavities for the same purpose.

WGMs were first introduced by Lord Rayleigh in 1910 to describe how sound waves propagate around circular buildings [Ref. 54]. In this case, sound waves reflected by walls travel along the concaved surface, self-interfere and are resonant under certain conditions. This idea was then applied to the propagation of electro-magnetic (EM) waves in spherical dielectrics [Ref. 55]. The observation of WGMs in EM waves provides an opportunity to produce high Q optical cavities and such a device was realized in semiconductors in 1991, by fabricating a microdisk made of GaAs based alloys with InGaAs quantum wells as the active medium [Ref. 56]. Owing to the relatively easy processing and the high Q WGMs over a broad spectral range, microdisks soon became great candidates for exploring light-matter interaction in semiconductors.

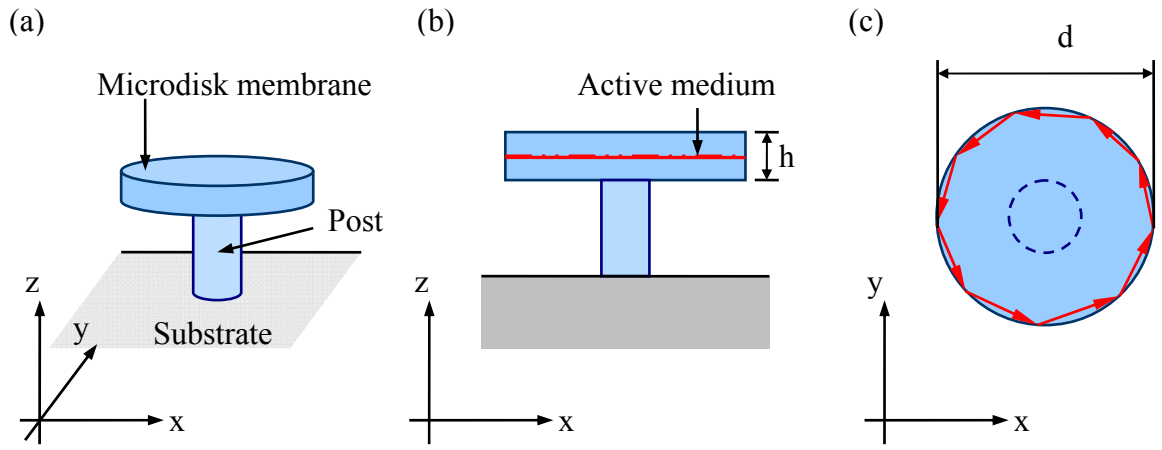

Fig. 5-8: Schematic views of a microdisk cavity including: (a) an angled view, (b) cross-section view and (c) Top-down view. Red arrows in (c) show possible light propagation path to form WGMs.

Figure 5-8 shows schematic views of a microdisk cavity. The cavity body is the circular disk labeled microdisk membrane in Figure 5-8 (a). The active medium is usually placed at the center of the membrane for maximum coupling to the confined EM fields, as shown in Figure 5-8 (b). The microdisk is connected to the substrate with a thin post, ensuring sufficient optical isolation between the disk and the substrate. Optical fields radiated by the active material can be confined by total internal reflection along the side-wall, forming WGMs, as shown in Figure 5-8 (c).

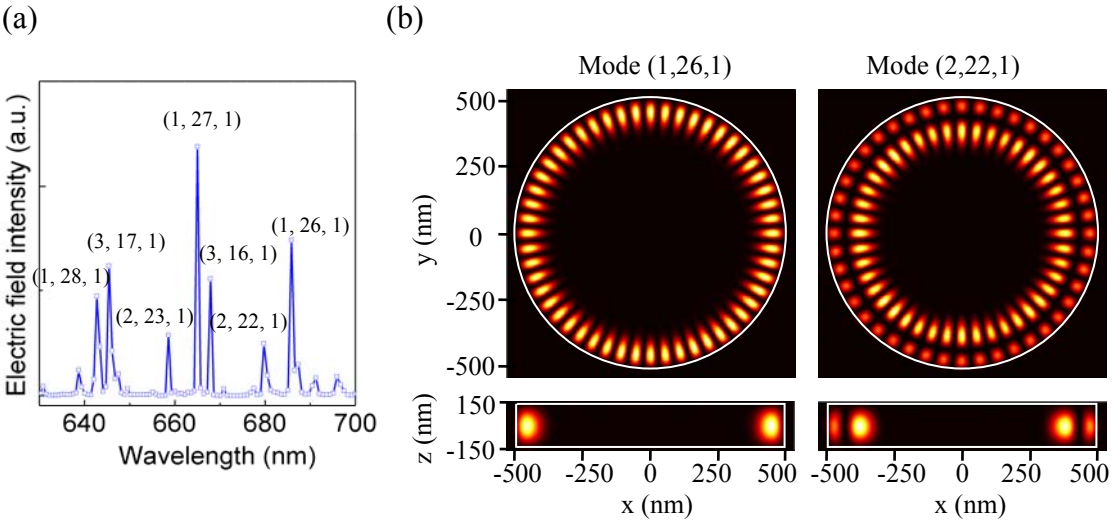

Fig. 5-9: (a) FDTD simulated spectrum of a microdisk with h = 290nm, d = 2um and n =3.6. WGMs are labeled in (n_r, n_φ, n_z) form. (b) Field distribution of WGMs (1,26,1) and (2,22,1)

Performance of such a cavity can be evaluated through FDTD simulations. In this simulation, a magnetic dipole polarized in the z direction located in the middle of the membrane near the edge of the microdisk is used to represent all possible in-plane electric field polarizations in SAQDs. A simulated spectrum of a microdisk with thickness of h = 290nm, diameter d = 2μm and refractive index n = 3.6 is shown in Figure 5-9 (a). A few sharp peaks can be identified in the spectrum as resonant WGMs. For such a structure with cylindrical symmetry, these WGMs could be identified with quantum numbers in cylindrical coordinates, as shown in Figure 5-9 (a). Figure 5-9 (b) shows examples of the field distribution of the first and second order WGMs with

different mode numbers.

How do we fabricate this geometry and use it to enhance emission from SAQDs? The microdisks are made experimentally with InP SAQDs grown by metal-organic vapor-phase epitaxy (MOVPE) [Ref. 57]. The sample was grown on a (100) GaAs substrate initially covered with 100nm GaAs/427nm GaAs-$Al_{0.5}Ga_{0.5}As$ superlattice/400nm GaAs buffer layers for better surface smoothness and lower defect density. On top of the buffer layer, 1μm of $Al_{0.5}Ga_{0.5}As$ was grown as a sacrificial layer for later processing. The QDs are embedded in a separate-confinement heterostructure (SCH) to optimize both electronic and optical confinement. The SCH is formed by two sequences of 10nm $(Ga_{0.51}In_{0.49})P$ / 59nm $((Al_{0.5}Ga_{0.5})_{0.51}In_{0.49})P$ / 35nm $((Al_{0.2}Ga_{0.8})_{0.51}In_{0.49})P$ / 40nm $(Ga_{0.51}In_{0.49})P$ layer and all lattice matched to GaAs and symmetrically arranged around the QD layer. The QDs were formed with 2.1 monolayers of InP deposited at 710°C leading to an area density of ~$1.5x10^{10}cm^{-2}$. SAQDs grown under such a condition have height of ~5.5nm in the z direction and a diameter ~30nm in the x-y plane. The significantly larger size in the x-y direction leads to in-plane electron–hole separation and hence an in-plane exciton dipole moment. A small fraction of the InP layer does not fully deform into QDs but acts like quantum wells. This thin layer is referred to as the "wetting layer." A schematic view of the material structure is shown in Figure 5-10.

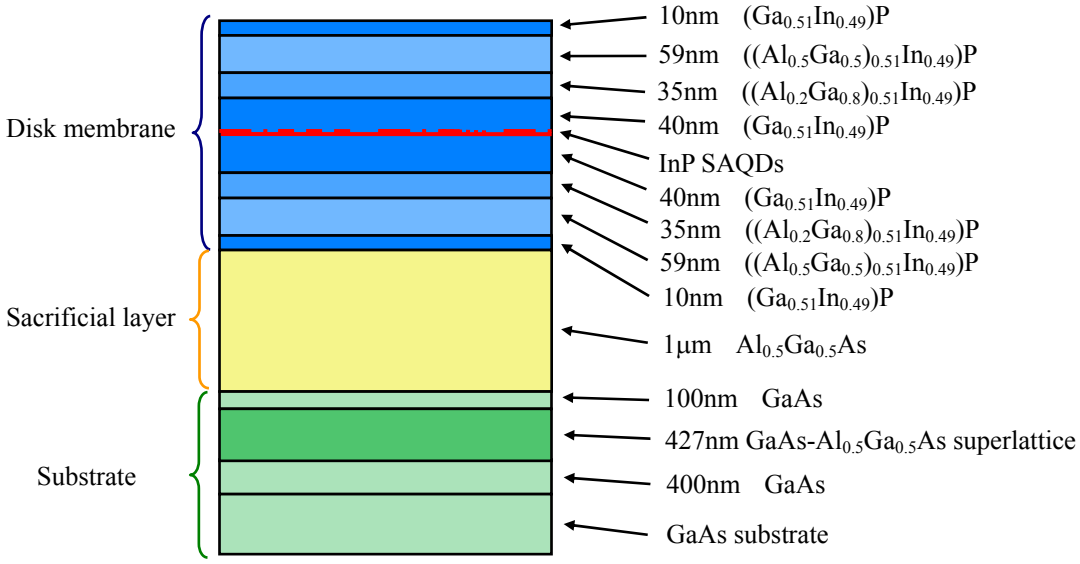

Fig. 5-10: Layered structure of the as-grown material for fabricating microdisk cavities for coupling to InP SAQDs. The figure is not drawn to scale.

To fabricate high-quality microdisks, electron beam (Ebeam) lithography was used to define the patterned mask for the subsequent etch. A hydrogen silsesquioxane-based Ebeam resist XR-1541 by Dow Corning Co. was exposed to a high-energy (125 kV) electron flux in an Elionix Ebeam lithography system. The exposed area formed amorphous silicon oxide and served as an etch mask in the subsequent inductively coupled plasma reactive ion etch. In the etch system, a hydrogen bromine (HBr)-based plasma was generated and directed toward the patterned wafer piece, using a bias to directionally etch the non-masked region, forming circular pillars with very smooth and vertical side walls. The etch depth was chosen to be approximately 1μm to ensure sufficient exposure of the sacrificial material

to the following wet chemical etch. After dry etching and removal of the exposed resist, an undercut etch was performed by soaking the sample in Transene aluminum etchant type A (a solution of phosphoric, nitric, and acetic acid) which dissolves only the high-aluminum-content sacrificial material, creating a post to optically isolate the microdisk from and the substrate. A SEM image of a fabricated microdisk is shown in Figure 5-11 (a).

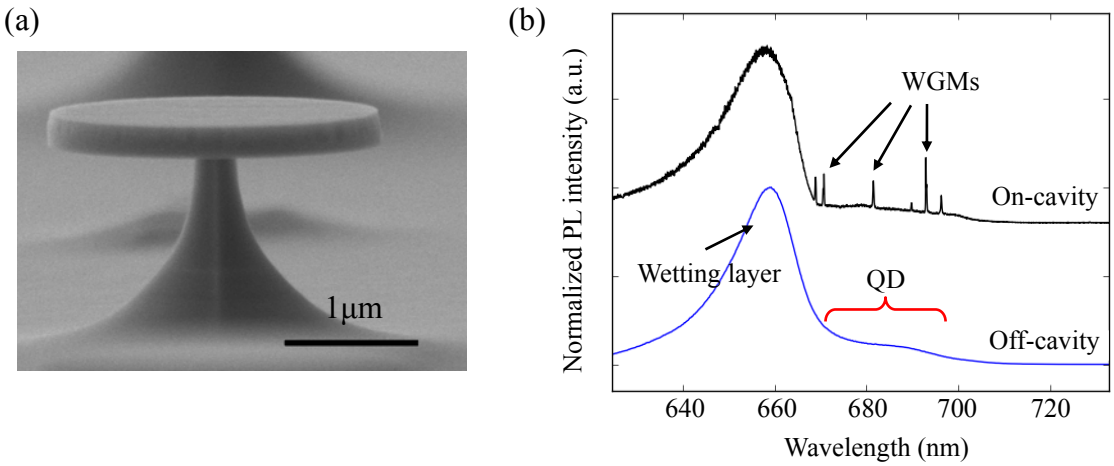

Fig. 5-11: (a) SEM image of a microdisk containing InP SAQDs. (b) Measured PL spectra of the as-grown SAQDs and a microdisk cavity made of the same material.

The fabricated microdisks were characterized with our PL measurement system (see Appendix B). At room temperature, a 532 nm solid state laser was focused onto the device with a 100x, 0.9 NA objective. The laser energy was above the band-gap of all

materials composing the microdisk. Therefore, the whole structure absorbed the incident light and the excited electron-hole pairs diffused into the QDs, where they radiatively recombined to be captured by the same objective and analyzed with a spectrometer.

The measured spectra are shown in Figure 5-11 (b). At room temperature, these InP SAQDs suffer from both homogeneous broadening caused by thermal fluctuation and in-homogeneous broadening caused by size and compositional distribution of the QDs. These broadenings result in a broad-band emission centered at ~685nm, as shown in the off-cavity spectrum in Figure 5-11 (b) (labeled QD in the spectrum). The strong peak centered at 660nm is the emission from the InP wetting layer.

A few sharp peaks, overlapping with the off-cavity broadband QD emission, were observed when pumping on the microdisk cavity. These peaks are representative of the WGMs interacting with the QDs. The Q of the WGMs range from 3000 to 5000 and is calculated by dividing the full-width half-maximum of the measured peaks by their peak wavelength (equation 1-2 in Chapter 1.) No WGMs are observed on the wetting layer emission because the quantum-wells have a significantly stronger re-absorption cross-section than QDs, thus eliminating the resonances.

Further experiments on studying lasing properties of these microdisks [Ref. 58] and creating photonic molecules composed of two couple microdisk cavities have also

been published by our collaborators [Ref. 59]. In this thesis, we focus on how to make plasmonic cavities out of these structures.

5.7 Plasmonic Microdisks for Coupling to InP SAQDs

As discussed in previous chapters, a significant loss mechanism for plasmonic cavities is the strong scattering at the reflective termination of the cavities. Such a termination can be avoided by creating the resonance by circulating the field in a closed loop like a microdisk cavity. Plasmonic WGM cavities for high Q resonances have been demonstrated in literature [Ref. 35, 60]. Here we combine this idea with our experiences in making SAQD containing photonic microdisks to produce plasmonic microdisks to interact with InP SAQDs.

As a dielectric structure gets close to a metal surface, the confined modes in the dielectric may hybridize with surface plasmon polaritons and be drawn toward the metal surface [Ref. 22]. This phenomenon has been well discussed in Chapter 4. The hybridized field is highly concentrated in the gap between the metal and the dielectric structure and the polarization direction of the electric field is nearly normal to the metal surface.

Controlling the polarization direction of the hybridized modes is critical for coupling to SAQDs. As mentioned in previous sections, the dipole moment of an

excited quantum dot is polarized nearly parallel to the dielectric surface. Therefore, to make a hybridized plasmonic WGM interact strongly with SAQDs, the metal needs to be aligned along the sides of the microdisks, as shown in Figure 5-12 (a) and (b). A thin dielectric spacer is required to control the field distribution and to prevent metal diffusion into disk membranes during metal evaporation. It is important to leave at least one "top" surface without any metal in order to collect light from the device. However, there are significant challenges to depositing metal only onto side of a microdisk without covering the top. Therefore, an adapted geometry, Figure 5-12 (c), and a fabrication method was developed to construct our plasmonic microdisks.

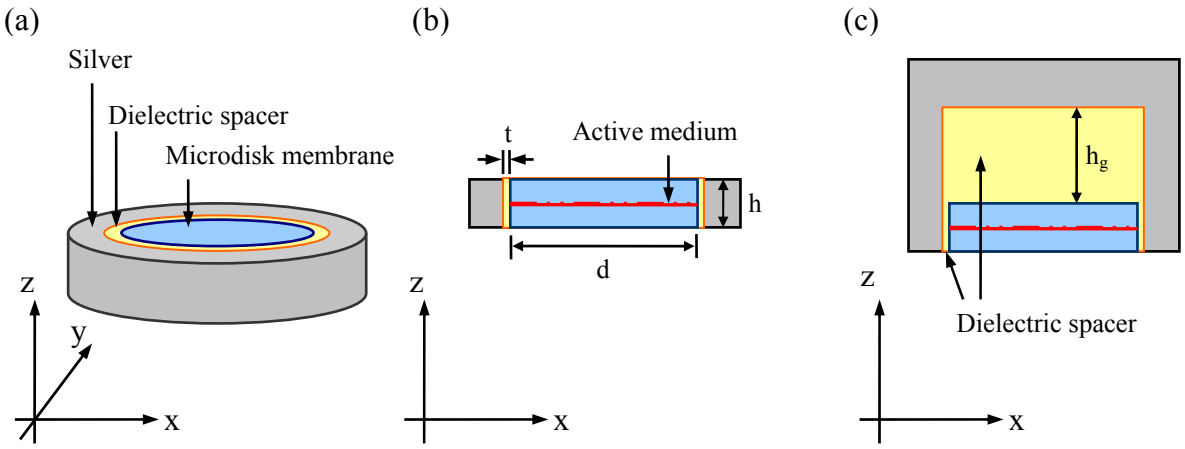

Fig. 5-12: Schematic views of a plasmonic microdisk including (a) an angled view and (b) a cross-section view. (c) A cross-section view of an adapted structure where a thick layer of dielectric spacer and silver layer is added on top of the microdisk.

Optical response of the adapted geometry in Fig 5-12 (c) can be evaluated by FDTD simulations. Figure 5-13 (a) shows a simulated spectrum and field distribution of a plasmonic disk with h = 290nm, d = 1um, t = 10nm and h_g = 500nm. The refractive index of the semiconductor disk and dielectric spacer are 3.6 and 1.4, respectively. The metal used is silver, modeled by optical parameters measurements from Johnson and Christy [Ref. 28].

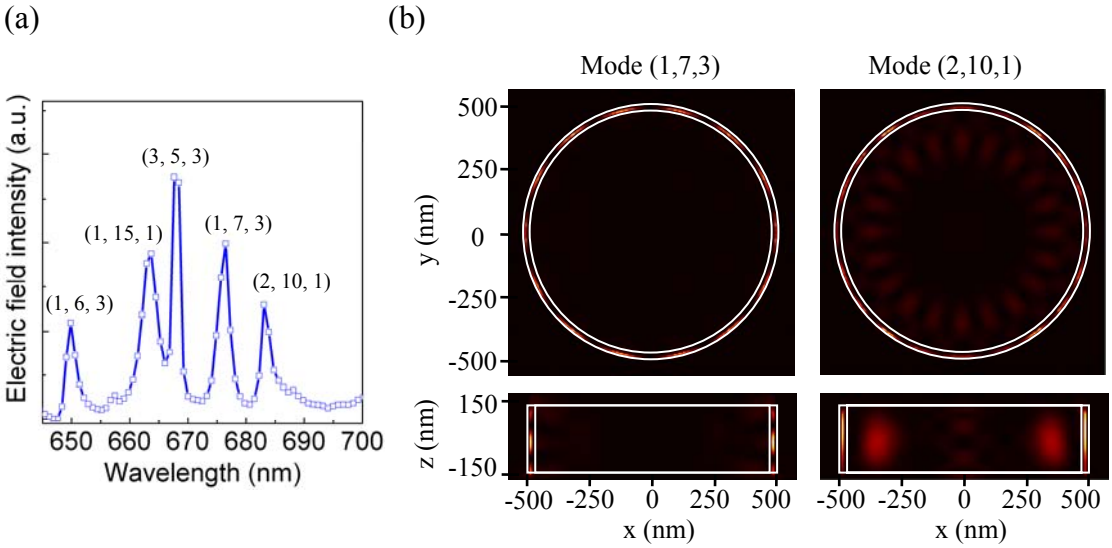

Fig. 5-13: FDTD simulated (a) spectrum with mode number labeled in (n_r, n_φ, n_z) form and (b) field distribution of the (1, 7, 3) and (2, 10, 1) modes from a plasmonic microdisk with h = 290nm, d = 1um, t = 10nm and h_g = 500nm. White lines show material outlines.

Several peaks can be found in the simulated spectrum as resonant modes and these

modes were identified with their quantum numbers by the field distributions. Examples of the electric field distribution of these plasmonic WGMs are demonstrated in Figure 5-13 (b). These distributions are similar to those of the photonic microdisks shown in Figure 5-9 with a major difference: the fields are highly concentrated into the small low index gap between the microdisk and the silver surface. There are two consequences of this field concentration: one, the mode volume of the WGMs is reduced from ~4 $(\lambda/n)^3$ in d=1μm photonic microdisks to ~0.2 $(\lambda/n)^3$ in plasmonic microdisks, and two, the Q is also reduced from ~3000-6000 to ~200-500.

The process flow used to fabricate these plasmonic microdisks is shown in Figure 5-14. Similar to how we fabricated the semiconductor microdisks, electron beam lithography with hydrogen silsesquioxane-based Ebeam resist was used to define the patterned mask. The resist used here is Fox-16 by Dow Corning Co. which has a thicker resist layer (~500nm) than XR-1541 (~110nm) spun at 300 R.P.M. The amorphous silicon oxide formed by exposed resist now serves not only as an etch mask in the subsequent inductively coupled plasma reactive ion etch but is also used as a spacer in the final structure. The same hydrogen bromine (HBr)-based plasma was used to etch the non-masked region, forming circular pillars with smooth and vertical side walls. After the dry etch, an undercut etch was performed again by soaking the sample into Transene aluminum etchant type A to create suspended disk structure. Until this step,

the process is almost the same as the method we used to fabricate microdisks shown in the previous section besides that we did not remove the exposed hydrogen silsesquioxane-based Ebeam resist from top of the microdisks.

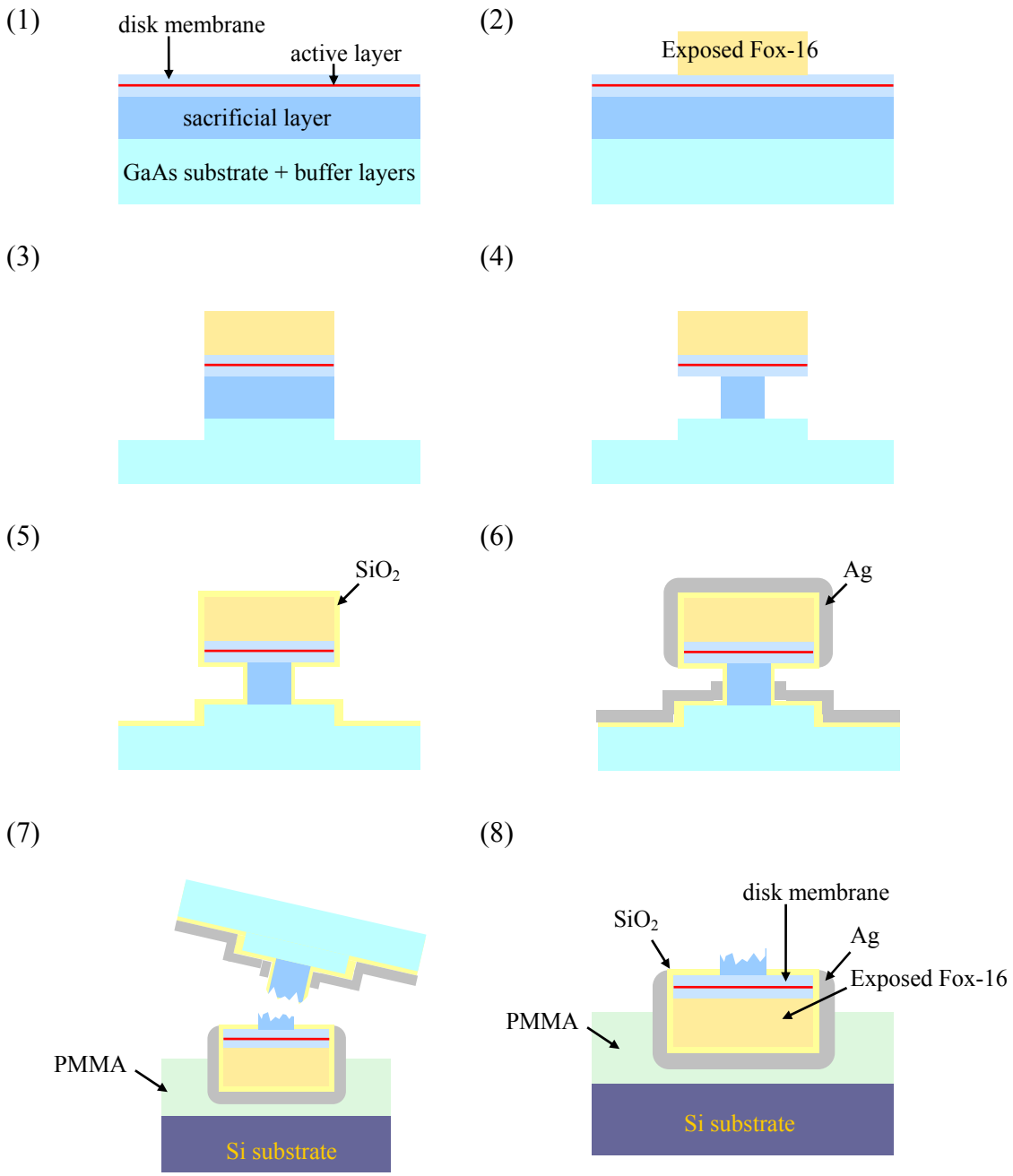

Fig. 5-14: Fabrication process flow for the plasmonic microdisks including: step

Fig. 5-14 (Continued): (1): the as-grown sample, step (2): e-beam lithography defined mask, step (3): HBr-based reactive ion etch, step (4): wet-chemical undercut etch, step (5): conformal deposition of SiO_2 by ALD, step (6): angled evaporation of Ag, step (7): transfer disks to a PMMA coated substrate and step (8): the final structure.

These fabricated microdisks have a thick layer of amorphous silicon oxide on top, as shown in the SEM image in Figure 5-15 (a), and were subsequently coated with a layer of 10nm SiO_2 by atomic layer deposition (ALD) as the spacer layer. ALD is a technique that produces a conformal coating around the structures. Around 100nm of silver is then thermally evaporated on the sample at a pressure of $4.2x10^{-7}$ Torr, a rate of ~3Å /s, and with the sample tilted at ~60 degrees. A SEM image of a silver coated microdisk is shown in Figure 5-15 (b) and an image for a FIB cut cross-section view is shown in Figure 5-15 (c).

At this stage, the plasmonic microdisk is formed, but optical measurements are difficult since top surface of the disks are covered with an opaque silver layer. Therefore, we flipped these microdisks upside-down onto a silicon substrate coated with PMMA. As the wafer piece containing the microdisks was pushed onto the PMMA coated surface, the disks stuck onto the soft PMMA and each of the fragile

posts broke off. This step resulted in flipped plasmonic microdisks sitting on the PMMA coated substrate. A SEM image of a flipped plasmonic microdisk is shown in Figure 5-15 (d). The "flipped" geometry allows optical measurements on the microdisk not covered by silver.

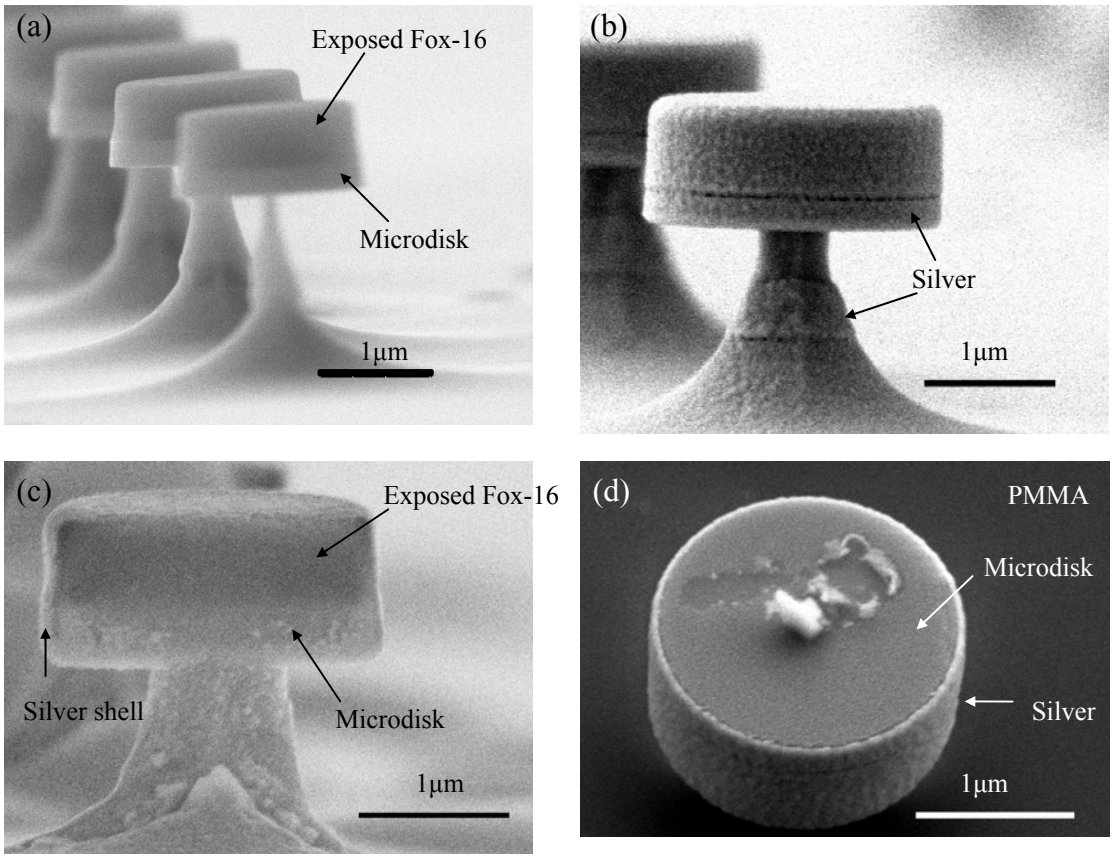

Fig. 5-15: SEM images of (a) microdisks with exposed Fox-16 on top, (b) plasmonic microdisks staying on original posts, (c) FIB cross-section of a plasmonic microdisk and (d) a flipped plasmonic microdisk on a PMMA coated substrate.

The plasmonic disks were characterized by the same PL set up as the microdisks shown in Section 5-6 and the measured spectra are shown in Figure 5-16. Comparing the on-cavity and off-cavity traces in Figure 5-16 (a), a resonant mode located at 676nm with Q ~300 is observed. Note that for hybrid WGMs with small mode volumes, only a small portion of SAQDs can couple to the WGMs. One way to increase this coupling ratio is to fabricate devices with smaller diameters. Figure 5-16 (b) shows similar measurements performed on plasmonic microdisks with a designed diameter near 1μm with small intentional diameter variation between the disks.

As the QD emission couples to WGMs in these plasmonic microdisks, mode peaks correspond to resonances having Q ranging from 250 to 460 were observed and the relative QD emission intensity compare to emission from the wetting layer greatly increased. The Q = 460 measured on the disk with the largest diameter is the highest reported Q for plasmonic modes probed by coupling to emitters to the best of our knowledge. In addition to the high Q and increased relative intensity, the resonant wavelengths of the modes are well controlled by slightly tuning of the disk diameter. As the designed diameter increased/decreased by 1%, the peak wavelength of the modes also shifted by ~1% (6.5nm). This is a demonstration of how dimension of a hybrid plasmonic cavity can be well controlled by precise fabrication techniques developed for semiconductor processes.

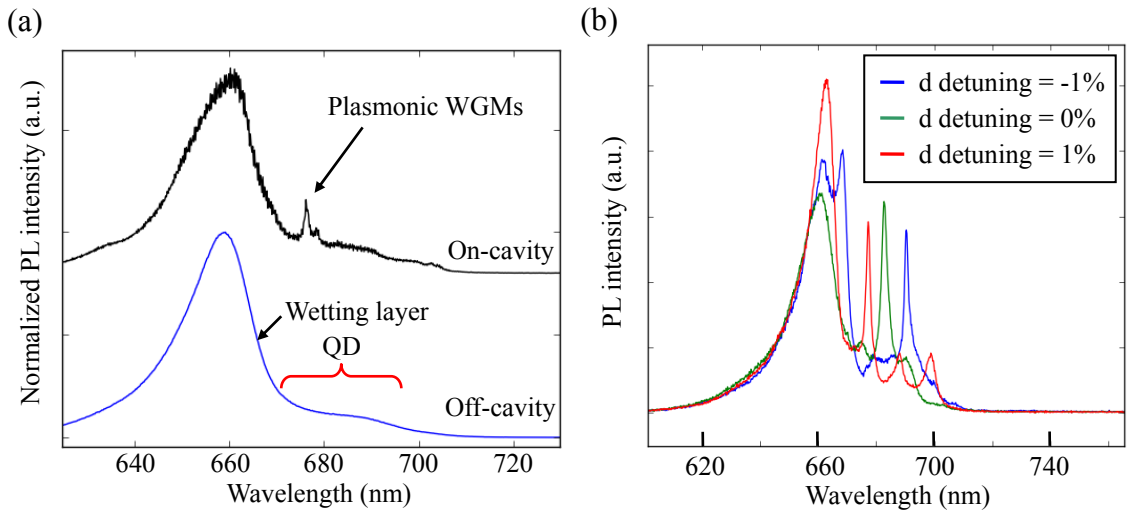

Fig. 5-16: Measured PL spectra of (a) the as-grown SAQDs and a plasmonic microdisk cavity made of the same material with d = 2μm and (b) a series of plasmonic microdisks with d slightly detuned from 1μm.

However, further work on how the emission characteristics of the SAQDs can be modified by the plasmonic WGMs is required. Such experiments include comparing the emission characteristics of QDs in cavities which are spectrally on and off resonance with the modes, measuring time transient and collection efficiency of the SAQDs coupled to WGMs, and studying single QD interaction with plasmonic WGMs.

The major challenge for using our plasmonic microdisks for these measurements is the poor overlap between the modal electric field intensity and our active medium in the cavity. Only a small portion of SAQDs, which lie near the edge of the microdisks,

can couple strongly to the plasmonic WGMs. It is difficult to evaluate the effect of the WGMs on the QDs with the diverted properties among the SAQDs. Cavities with a lower QD density or reduced active area may be required for further verification of the possible emission enhancement by these plasmonic cavities.

5.8 Conclusions to Plasmonic Microdisks

As a conclusion, we adapted our experiences in making photonic microdisks to make plasmonic microdisks for coupling to InP SAQDs. The plasmonic WGMs in these cavities are designed to match the polarization direction of the SAQDs. To fulfill this purpose, we developed a fabrication method to apply silver onto the side of the microdisks. SEM images of the fabricated devices show good coverage of silver onto the disks.

FDTD simulations of such a microdisk show strongly concentrated plasmonic WGMs with Q ~ 200-500 and mode volumes of less than a cubic wavelength. The PL measurement show cavity resonances coupled to QD emission with Q as high as 460 and a strong increased intensity at the mode wavelength. In addition, the cavity resonances are well controlled by size variation of the microdisks. Designing plasmonic cavities with modes overlapping better with the active areas is desired for further improving coupling between plasmonic cavities and SAQDs.

Chapter 6
Conclusions and Recommendations

6.1 Conclusions

Since the early demonstration of cavity enhanced spontaneous emission in 1983 [Ref. 2], there has been a tremendous advance in applying dielectric microcavities for enhanced light matter interaction for quantum optics. Recently, more attention has been drawn to the development of plasmonic nanocavities for their ability to confine light within sub-wavelength dimensions and thereby achieve significant enhancement of spontaneous emission.

In this thesis, we demonstrated the design and fabrication of four different types of plasmonic cavities. Each cavity geometry was created for a different purpose but serves the same goal: to explore the possibility of controlling resonances of plasmonic structures for manipulating spontaneous emission from various emitters. As a summary of all the cavities used in this thesis, a modified Figure 1-1 with the plasmonic cavities described is shown in Figure 6-1.

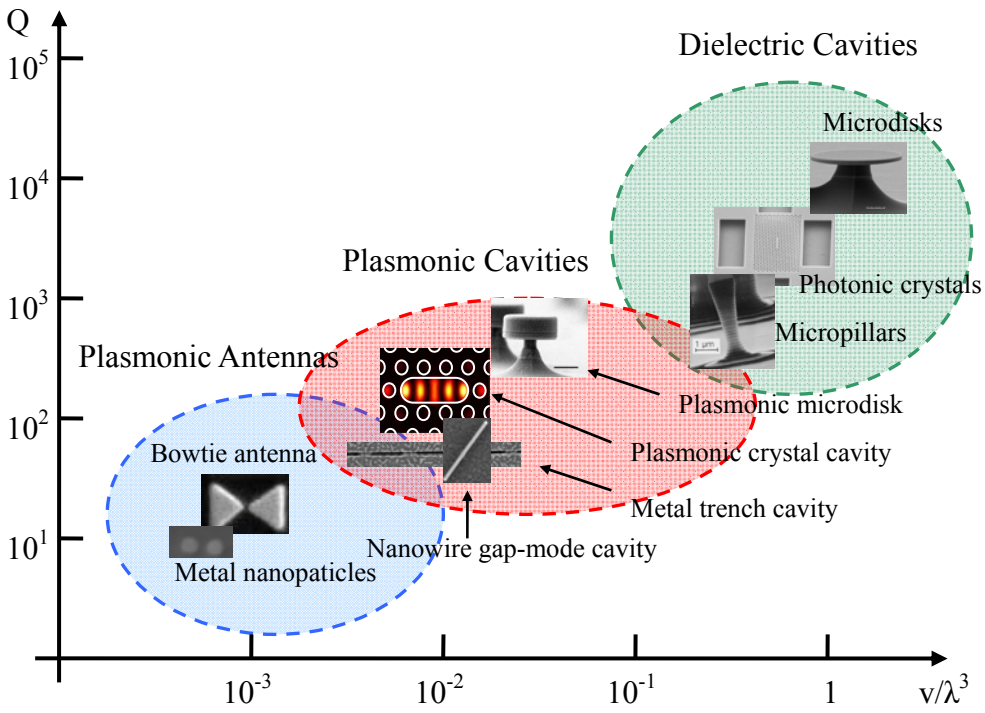

Fig. 6-1: Typical Q and v values for various kinds of optical resonators including the plasmonic cavities described in this thesis.

A few important points I learned from these experiments which could be widely applicable to researches on plasmonic resonant devices are the following:

1. Although metals are inherent lossy materials, performance of the current plasmonic cavities is most strongly limited by fabrication. Developing methods to precisely shape metallic structures or define cavities with dielectric structures is essential for making high quality plasmonic cavities.

2. Metal-induced quenching effects, finite absorption loss in metal, and the alteration of collection and excitation efficiency (i.e. antenna effects) together make it difficult to

precisely measure emitter dynamics. All these effects must be considered while trying to demonstrate modification of emitter characteristics by plasmonic resonators.

3. Despite evaluating a plasmonic cavity with the degree of enhancement on spontaneous emission rate it can achieve by measuring Q and V of a mode, performance of such a device is strongly affected by the extraction efficiency of the cavity. A figure of merit other than the Q/V ratio should be considered. Applications for mid-high Q plasmonic cavities could be strongly limited by metal loss because of their low external quantum efficiency. As the metal loss dominates the Q of a cavity, it also becomes the dominant energy flow pathway. Therefore, designing extremely high Q plasmonic cavities may be meaningless unless the extraction efficiency can be guaranteed.

6.2 Recommendations

With the ability of concentrating light within the sub-wavelength scale, plasmonic cavities are capable of exploring light-matter interactions in a regime that cannot be achieved with dielectric structures. However, applications of these plasmonic cavities are strongly limited by the lossy nature of metals and the metal-induced quenching effect. Therefore, a plasmonic cavity must be designed and modified with a clear purpose for the application.

Here I have two suggestions of possible applications for plasmonic cavities based on the experience gained from works described in this thesis:

1. Ultra-small electrically-driven light source which can be integrated with on-chip circuits: the fact that metals are good conductors that can be deposited onto almost any substrate makes plasmonic cavities good candidates for optical sources driven by on-chip electronic circuits. Plasmonic cavities designed for this purpose may not need high Q and require only a relatively simple structure which can be lithographically defined. Geometries similar to our nanowire cavities but with well controlled cavity positions or hybrid plasmonic cavities in which the cavities are defined by shaping the semiconductor substrate may serve this purpose. Studies on maximizing the external quantum efficiency are necessary for this application.

2. Integrated plasmonic circuits for monitoring inter-device plasmonic coupling: besides increasing far-field radiation efficiency, a good way to use the strongly enhanced plasmons is to couple through plasmonic waveguides. Compared to integrated optical systems, an integrated plasmonic system may occupy a much smaller area and may be operated at a higher speed with its shorter photon and emitter lifetimes. A 2-D plasmonic crystal may serve this purpose but further studies on the properties of plasmonic crystal waveguides and coupling between the devices are required. Fabrication methods to precisely construct such a system are also necessary. In

addition to research at the device and application level, understanding material properties of metals is essential for driving progress in plasmonics. Methods to grow high quality or even single crystal metals on different substrates may fundamentally change the way we design plasmonic devices. Further studies on techniques to define metallic structures are also necessary for fabricating more complicated plasmonic systems.

References

1. E. M. Purcell, *Phys. Rev.* 69, 681 (1946).
2. P. Goy, J. M. Raimond, M. Gross, and S. Haroche,“Observation of cavity-enhanced single-atom spontaneous emission,” *Phys. Rev. Lett.* 50, 1903–1906 (1983).
3. K. J. Vahala, "Optical Microcavities", *Nature*, 424, 839-846, 2003.
4. J. M. G´erard and B. Gayral, "Strong Purcell Effect for InAs Quantum Boxes in Three-Dimensional Solid-State Microcavities", *Journal of Lightwave Technology*, 17, No. 11, 2089-2095 (1999).
5. J. M. Ge´rard, D. Barrier, J. Y. Marzin, R. Kuszelewicz, L. Manin, E. Costard, V. Thierry-Mieg and T. Rivera, "Quantum boxes as active probes for photonic microstructures: The pillar microcavity case", *Appl. Phys. Lett.* 69, 449 (1996).
6. J.-H. Huang, V. Callegari, P. Geisler, C. Brüning, J. Kern, J. C. Prangsma, X. Wu, T. Feichtner, J. Ziegler, P. Weinmann, M. Kamp, A. Forchel, P. Biagioni, U. Sennhauser and B. Hecht, "Atomically flat single-crystalline gold nanostructures for plasmonic nanocircuitry", *Nature Communications*, 1, Article number: 150 (2010).
7. S. Zenga, X. Yuc, W.-C. Lawd, Y. Zhangc, R. Hua, X.-Q. Dinhb, H.-P. Hoe, K.-T. Yong, "Size dependence of Au NP-enhanced surface plasmon resonance based on differential

phase measurement", *Sensors and Actuators B: Chemical*, 176, 1128–1133, (2013).

8. D. K. Gramotnev and S. I. Bozhevolnyi, “Plasmonics beyond the diffraction limit”, *Nature Photonics* 4, 83 - 91 (2010)
9. AG. Curto, G. Volpe, TH. Taminiau, MP. Kreuzer, R. Quidant, NF. van Hulst, "Unidirectional emission of a quantum dot coupled to a nanoantenna", *Science*, 329 No. 5994, 930-933, (2010).
10. Y. Chu, M. G. Banaee and K. B. Crozier, "Double-Resonance Plasmon Substrates for Surface-Enhanced Raman Scattering with Enhancement at Excitation and Stokes Frequencies", *ACS Nano*, vol. 4, 2804 (2010).
11. K. J. Russell, and E. L. Hu, "Gap-mode plasmonic nanocavity", *Appl. Phys. Lett.* 97, 163115 (2010).
12. J. Y. Marzin, J. M. Gérard, A. Izraël, and D. Barrier, "Photoluminescence of Single InAs Quantum Dots Obtained by Self-Organized Growth on GaAs", *Phys. Rev. Lett.* 73, 716–719 (1994).
13. K. H. Drexhage, "Influence of a dielectric interface on fluorescence decay time." *Journal of Luminescence*, 1-2, 693–701 (1970).
14. A. Yariv and P. Yeh, "Photonics", Chapter 4.
15. N. W. Ashcroft and N. D. Mermin, "Solid State Physics", Thomson Learning, Chapter 1.

16. M. A. Ordal, R. J. Bell, R. W. Alexander,Jr, L. L. Long, and M. R. Querry, "Optical properties of fourteen metals in the infrared and far infrared: Al, Co, Cu, Au, Fe, Pb, Mo, Ni, Pd, Pt, Ag, Ti, V, and W.", *Applied Optics*, 24, pp. 4493-4499 (1985).

17. S. A. Maier, "Plasmonics: Fundamentals and Applications", Springer,Chapter 2.

18. G. V. Naik, J. Kim, and A. Boltasseva, "Oxides and nitrides as alternative plasmonic materials in the optical range", *Optical Materials Express*, 1. No. 6, 1090-1099, (2011).

19. E. Kretschmann and H. Raether, "Radiative decay of non-radiative surface plasmons excited by light", *Z. Naturforschung A*, 23, 2135-2136 (1968).

20. S. Park, G. Lee, S. H. Song, C. H. Oh, and P. S. Kim, "Resonant coupling of surface plasmons to radiation modes by use of dielectric gratings", *Optics Letters*, 28, Issue 20, 1870-1872 (2003).

21. R. D. Averitt, S. L. Westcott, and N. J. Halas, "Linear optical properties of gold nanoshells", *JOSA B*, 16, Issue 10, 1824-1832 (1999).

22. R. Oulton, V. Sorger, D. A. Genov, D. F. P. Pile, X. Zhang, "A hybrid plasmonic waveguide for subwavelength confinement and long range propagation", *Nature Photonics*, 2, 496-500 (2008).

23. R.R. Chance, A. Prock and R. Silbey, "Molecular Fluorescence and Energy Transfer near Interfaces", *Advance in Chemical Physics*, 37, 1-65 (1978).

24. G.W. Ford and W.H. Weber, "Electromagnetic Interactions of Molecules with Metal

Surfaces", *Physics Reports*, 113, No.4 195-287 (1984).

25. J. R. Lakowicz, "Radiative decay engineering 5: metal-enhanced fluorescence and plasmon emission", *Anal Biochem.,* 337 (2), 171-94, (2005).

26. J. M. McMahon, S. K. Gray, and G. C. Schatz, "Nonlocal Optical Response of Metal Nanostructures with Arbitrary Shape", *Phys. Rev. Lett.* 103, 097403 (2009).

27. S. Noda, M. Fujita and T. Asano, "Spontaneous emission control by photonic crystals and nanocavities", *Nature Photonics*, 1, 449-458 (2007).

28. P. B. Johnson and R.W. Christy, "Optical Constants of the Noble Metals", *Phys. Rev. B.* 6, 4370 (1972).

29. P. Nagpal, N. C. Lindquist, S.-H. Oh, and D. J.Norris, "Ultrasmooth patterned metals for plasmonics and metamaterials." *Science*, 325, 594–597 (2009).

30. D. Z. Garbuzov, V. Bulović, P E. Burrows and S. R. Forrest, "Photoluminescence efficiency and absorption of aluminum-tris-quinolate (Alq3) thin films", Chemical *Physics Letters*, 249, 433–437 (1996).

31. K. Hennessy, A. Badolato, M. Winger, D. Gerace, M. Atatüre, S. Gulde, S. Fält, E. L. Hu and A. Imamoglu, “Quantum nature of a strongly coupled single quantum dot–cavity system,” *Nature*, 445, 896-899, (2007).

32. S. Ku¨hn, U. Ha°kanson, L. Rogobete, and V. Sandoghdar, ” Enhancement of Single-Molecule Fluorescence Using a Gold Nanoparticle as an Optical Nanoantenna,”

Phys. Rev. Lett. 97, 017402 (2006)

33. R. F. Oulton, V. J. Sorger, T. Zentgraf, R.-M. Ma, C. Gladden, L. Dai, G. Bartal and X. Zhang, “Plasmon lasers at deep subwavelength scale,” *Nature*, 461, 629-632 (2009).

34. S. I. Bozhevolnyi, V. S. Volkov, E. Devaux, and T. W. Ebbesen, “Channel plasmon-polariton guiding by subwavelength metal grooves,” *Phys. Rev. Lett.*, 95, 046802 (2005).

35. E. Jan, R. Vesseur, F. Javier, G. de Abajo, and A. Polman, “Modal Decomposition of Surface-Plasmon Whispering Gallery Resonators,” *Nano Lett.*, 9(9), 3147-3350 (2009).

36. B. Radha and G. U. Kulkarni, "A Real Time Microscopy Study of the Growth of Giant Au Microplates," *Crystal Growth & Design*, 11, No. 1, 320–327 (2011).

37. M. R. Khan, I. K. Schuller and CH. M. Falco, "Sputter Epitaxy of Ag and Ni Films", *phys. stat. sol. (a),* 73, 1, 23-29 (1982).

38. M. J. Loboda, G. A. Toskey, “Understanding hydrogen silsesquioxane-based dielectric films processing”, *Solid State Technology*, 41, 5, (1998).

39. S. Reitzenstein, C. Hofmann, A. Gorbunov, M. Strauß, S. H. Kwon, C. Schneider, A. Löffler, S. Höfling, M. Kamp, and A. Forchel, “AlAs/GaAs micropillar cavities with quality factors exceeding 150,000”, *Appl. Phys. Lett.*, 90, 251109 (2007).

40. K. J. Russell, K. Y.-M. Yeung, and E. L. Hu. “Measuring the Mode Volume of

Plasmonic Nanocavities Using Coupled Optical Emitters." *Physical Review B*, 85, No. 24: 245445 (2012).

41. S. Zhang, Y.-S. Park, Y.-M. Liu, T. Zentgraf, and X. Zhang. "Far-field Measurement of Ultra-small Plasmonic Mode Volume." *Optics Express*,18, 6048-6055 (2010).
42. Y. Su, Z. Zheng, Y. Bian, L. Liu, X. Zhao, J. Liu, T. Zhou, S. Guo, W. Niu, Y. Liu and J. Zhu, "Metal-coated hollow nanowires for low-loss transportation of plasmonic modes with nanoscale mode confinement", *J. Opt.*, 14, 095501 (2012).
43. E. Yablonovitch, "Inhibited Spontaneous Emission in Solid-State Physics and Electronics," *Phys. Rev. Lett.,* 58 (20): 2059–2062, (1987).
44. J. D. Joannopoulos, S. G. Johnson, J. N. Winn, and R. D. Meade, "Photonic Crystals: Molding the Flow of Light," Princeton NJ: Princeton University Press.
45. J. Vuckovic and Y. Yamamoto, "Photonic crystal microcavities for cavity quantum electrodynamics with a single quantum dot" *App. Phys. Lett*., 82, No. 15, 2374-2376, (2003).
46. X. Yang, A. Ishikawa, X. Yin, and X. Zhang, "Hybrid photonic-plasmonic crystal nanocavities," *ACS Nano*, 5, 2831-2838 (2011).
47. A. M. Lakhani, M.-K. Kim, E. K. Lau, and M. C. Wu, "Plasmonic crystal defect nanolaser", *Optics Express*, 19, 19, 18237-18245 (2011).
48. S. G. Johnson and J. D. Joannopoulos, "Photonic Crystals: The Road from Theory to

Practice", Kluwer, (2002).

49. A. C. Scofield, J. N. Shapiro, A. Lin, A. D. Williams, P. S. Wong, B. L. Liang and D. L. Huffaker, "Bottom-up photonic crystal cavities formed by patterned III-V nanopillars", *Nano Lett.*, 11, 6, 2242-2246 (2011).

50. Y. Akahane, T. Asano, B.-S. Song and S. Noda, "High-Q photonic nanocavity in a two-dimensional photonic crystal", *Nature*, 425, 944-947 (2003).

51. B. J. Riel, "An introduction to self-assembled quantum dots", *Am. J. Phys.*, 76, 8, 750 (2008).

52. D. Press, T. D. Ladd, B.-Y. Zhang and Y. Yamamoto, "Complete quantum control of a single quantum dot spin using ultrafast optical pulses", *Nature*, 456, 218-221 (2008).

53. M. Pfeiffer, K. Lindfors, C. Wolpert, P. Atkinson, M. Benyoucef, A. Rastelli, O.G. Schmidt, H. Giessen, and M. Lippitz, "Enhancing the Optical Excitation Efficiency of a Single Self-Assembled Quantum Dot with a Plasmonic Nanoantenna", *Nano Lett.*, 10, 11, 4555–4558 (2010).

54. Lord Rayleigh," CXII. The problem of thewhispering gallery", *Philosophical Magazine*, Series 6, 1001-1004 (1910).

55. C. Garrett, W. Kaiser, and W. Bond, "Stimulated Emission into Optical Whispering Modes of Spheres," *Phys. Rev.* 124, 1807 (1961)..

56. S. L.McCall, A. F. J. Levi, R. E. Slusher, S. J. Pearton, and R. A. Logan,

"Whispering-gallery mode microdisk lasers ", Appl. Phys. Lett. 60, 289 (1992).

57. W.-M. Schulz, R. Roßbach, M. Reischle, G. Beirne, M. Bommer, M. Jetter and P. Michler, “Optical and structural properties of InP quantum dots embedded in $(Al_xGa_{1-x})_{0.51}In_{0.49}P$”, *Phys. Rev. B*, 79, 35329 (2009).

58. M. Witzany, R. Roßbach, W.-M. Schulz, M. Jetter, P. Michler, T.-L. Liu, E. Hu, J. Wiersig and F. Jahnke, Lasing properties of InP/$(Ga_{0.51}In_{0.49})$P quantum dots in microdisk cavities, *Phys. Rev. B*, 83, 205305 (2011).

59. M. Witzany, T.-L. Liu, J.-B. Shim, F. Hargart, E. Koroknay, W.-M. Schulz, M. Jetter, E. L. Hu, J. Wiersig and P. Michler, "Strong mode coupling in InP quantum dot-based GaInP microdisk cavity dimers", *New Journal of Physics*, 15, 013060 (2013).

60. B. Min, E. Ostby, V. Sorger, E. Ulin-Avila, L. Yang, X. Zhang, K. Vahala, “High-Q surface-plasmon-polariton whispering-gallery microcavity”, *Nature*, 457(7228), 455-458 (2009).

Appendices

Appendix A: Optical Properties of Drude Metals

Metals are materials with a high density of free electrons. The existence of these electrons strongly determines the optical and electrical properties of these materials. In this appendix I introduce how the optical properties of metals can be derived from the Drude model [Ref. 15].

To calculate how a metal responds to a time-dependent electric field, let's first look at the equation of motion of electrons under such a field:

$$m_e \frac{d\vec{v}}{dt} = \vec{F} - m_e \frac{\vec{v}}{\tau_e} = -e\vec{E} - m_e \frac{\vec{v}}{\tau_e} \quad \text{(A-1)}$$

where m_e is the electron mass, **v** is the electron velocity, **F** is the driving force, e is the electron charge, **E** is the electric field intensity and τ_e is the average scattering time of electrons. For a time-varying field, it is convenient to write the field as:

$$\vec{E}(t) = \mathrm{Re}(\vec{E}(\omega)e^{-i\omega t}) \quad \text{(A-2).}$$

We can use the same method for all time-varying components in equation 2-8 and remove all the sinusoidal time dependence:

$$-i\omega\vec{v}(\omega) = -e\frac{\vec{E}(\omega)}{m_e} - \frac{\vec{v}(\omega)}{\tau_e} \quad \text{(A-3).}$$

We can express the current density (**j**) as:

$$\vec{j} = -en\vec{v} \tag{A-4}$$

where n is the electron volume density. Rearranging equation A-4 and then replacing the electron velocity in equation A-3 gives:

$$\vec{j}(\omega) = -en\vec{v}(\omega) = \frac{ne^2 / m_e}{1/\tau_e - i\omega}\vec{E}(\omega) = \sigma(\omega)\vec{E}(\omega) \tag{A-5}.$$

From this equation we can define a frequency-dependent conductivity σ(ω), where:

$$\sigma(\omega) = \frac{\sigma_0}{1 - i\omega\tau_e} \;\; ; \;\; \sigma_0 = \frac{ne^2\tau_e}{m_e} \tag{A-6}$$

and the parameter σ_0 is simply the DC conductivity of the metal.

Now let's look at the optical properties of the material by analyzing Maxell's equation in phasor form:

$$\nabla \cdot \vec{E} = \frac{\rho}{\varepsilon} \;\; ; \;\; \nabla \cdot \vec{H} = 0 \tag{A-7}$$

$$\nabla \times \vec{E} = -\mu\frac{\partial \vec{H}}{\partial t} = i\omega\mu\vec{H} \tag{A-8}$$

$$\nabla \times \vec{H} = \varepsilon\frac{\partial \vec{E}}{\partial t} + j = -i\omega\varepsilon\vec{E} + j = (\sigma - i\omega\varepsilon)\vec{E} \tag{A-9}$$

where ε is the permittivity and μ is the permeability. Taking the curl of both sides of equation A-8 and replacing the curl of the magnetic field by the right hand side of equation A-9 leads to the wave equation of the electric field as:

$$-\nabla^2\vec{E} = i\omega\mu_0(\sigma - i\omega\varepsilon_0)\vec{E} = \omega^2\varepsilon_0\mu_0(1 + \frac{i\sigma}{\omega})\vec{E}$$

(A-10).

Equation A-10 describes a propagating wave in a material with permittivity:

$$\varepsilon = \varepsilon_0(1 + \frac{i\sigma}{\omega})$$

(A-11).

Then we can define the frequency dependent relative permittivity (dielectric constant) as:

$$\varepsilon_r(\omega) = (1 + \frac{i\sigma}{\omega})$$

(A-12).

Replacing the conductivity in equation A-12 with the frequency dependent conductivity derived in equation A-6, we can get:

$$\varepsilon_r(\omega) = 1 + \frac{i\frac{\sigma_0}{1 - i\omega\tau_e}}{\omega} = 1 - \frac{\sigma_0\tau_e}{1 + \omega^2\tau_e^2} + \frac{i\sigma_0/\omega}{1 + \omega^2\tau_e^2}$$

(A-13).

The relation looks complicated but can be reduced if we ignore the scattering loss of the electrons under the conditions that the operating frequency is much higher than the electron scattering rate. This means that if $\omega\tau_e >> 1$, equation A-13 reduces to:

$$\varepsilon_r(\omega) = 1 - \frac{\sigma_0/\tau_e}{\omega^2} + i\frac{\sigma_0/\tau_e^2}{\omega^3} = 1 - \frac{ne^2/m_e}{\omega^2} + i\frac{ne^2/m_e\tau_e}{\omega^3}$$

(A-14).

Now we can define a parameter ω_p called the plasma frequency as:

$$\mathrm{Re}\{\varepsilon_r(\omega)\} = 1 - \frac{\omega_p^2}{\omega^2}\text{; where } \omega_p^2 = \frac{ne^2}{m_e}$$

(A-15).

Similarly, the imaginary part of the dielectric constant can be written as:

$$\mathrm{Im}\{\varepsilon_r(\omega)\} = \frac{\omega_p^2 \frac{1}{\tau_e}}{\omega^3}$$

(A-16).

The total dielectric constant then becomes:

$$\varepsilon_r(\omega) = 1 - \frac{\omega_p^2}{\omega^2} + i\frac{\omega_p^2 \frac{1}{\tau_e}}{\omega^3}$$

(A-17)

where the plasmonic frequency ω_p is defined as in equation A-15 and τ_e is the average scattering time of the free electrons.

Appendix B: Photoluminescence (PL) Measurement

Most measurements in this thesis were done with a custom micro photo-luminescence measurement system in our lab. A schematic view of the system is shown in figure B-1.

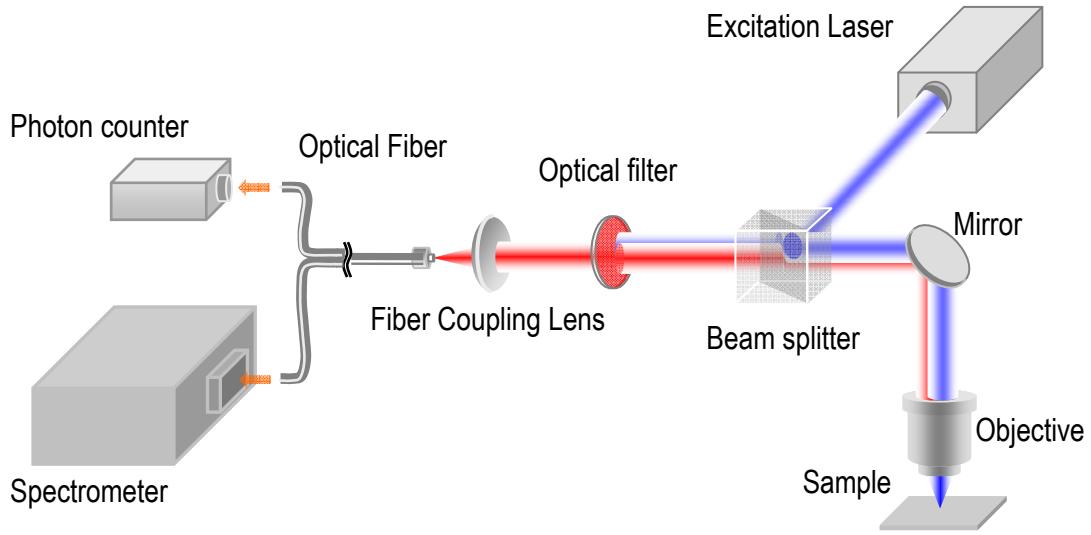

Fig. B-1: A schematic view of our microphotoluminescence measurement system.

In our system, the excitation source could be one of several different lasers. In most of the results demonstrated in this thesis, the laser source was a continuous-wave (CW) green laser with 532nm wavelength. In the time-resolved PL measurements shown in chapter 3, a frequency-doubled, pulsed Ti:sapphire laser of 450nm wavelength was used.

The excitation laser was sent through a high numerical aperture objective (NA = 0.9) to be focused onto the sample of interest. The sample absorbed some of this incident laser and then re-emitted light of a different (longer) wavelength characteristic of the emitter. Some of the emitted photons were captured by the objective and ultimately directed through an optical fiber to the detection system.

To identify the frequency response of the measured devices, the collected signal was sent into a grating-coupled monochrometer and with a silicon charge-coupled device (CCD) camera. This gives a spectrum of the emission. For time-resolved measurements, the signal was sent into a fast photon counter (MPD Micro Photon Devices). Comparing the time difference between the laser pulse and the collected signal gives the excited-state lifetime of the emitter.

Appendix C: Emission Properties of Alq3

The organic dye Alq3 was used in multiple works in this thesis. Especially in Chapter 3, the numerical modeling and overall enhancement are calculated based on the emission rate and efficiency of the Alq3 films. However, one problem for organic molecules like Alq3 is that the radiation properties are easily affected by the film quality, including deposition condition, material purity and post-deposition process damage. Therefore, it is important to precisely measure the radiative transition rate and efficiency of the Alq3 film prepared for our devices. Both the non-radiative transition rate and total lifetime can be derived from these two parameters.

The experiment we used to measure these two parameters is based on Drexhage's model introduced in Section 2.1 [Ref. 13]. Emission properties of Alq3 were measured with various distances to a metal surface to compare with the model. For this purpose, 14 samples of Alq3/Al_2O_3/Ag with varying thicknesses of atomic layer deposition (ALD) deposited Al_2O_3 were fabricated. These samples were divided into two batches and the same thickness (2.6nm) of Alq3 was evaporated onto each batch separately. PL measurements similar to what we did in for nanowire cavities shown in chapter 3 were performed, and the lifetime and fitted peak intensity versus spacer thickness were plotted in Figure C-1.

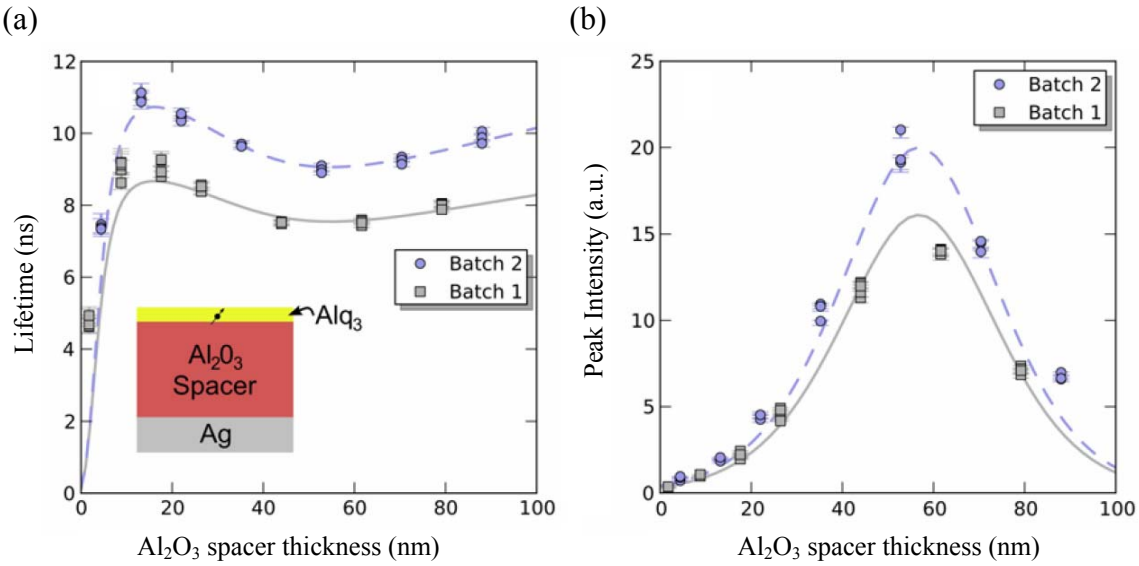

Fig. C-1: Measured (a) lifetime and (b) peak intensity versus spacer thickness of the 14 Alq3/Al_2O_3/Ag samples. Fitting results for batch 1 (gray solid curve) and batch 2 (blue dashed curve) are also shown in both figures.

The data shown in Figure C-1 (a) was fitted with the theoretical model for a free-space wavelength of 550nm. Two fitting parameters were used in the analysis: the radiative lifetime v_r^0 and the internal quantum efficiency η_{int}. The resulting curves were shown in the same figure and the parameters were determined to be $v_r^0 = 46$ns for both batches, $\eta_{int} = 0.18$ for batch 1 and $\eta_{int} = 0.22$ for batch 2.

Further verifying the fitting results, the calculated peak intensities based on the same parameters were also compared with measured data. However, the peak intensity is related to not only the emission efficiency but also the excitation and collection efficiency of the measurement process. The dependence of excitation efficiency on

spacer thickness was determined by calculating the emission rate at the laser wavelength (460 nm) into photon states of wavevector less than the numerical aperture of the microscope objective (0.9 NA). We assume that the absorption rate is proportional to the spontaneous emission rate base on the Einstein A and B coefficients. To enable comparison with cavity data, the absorption is normalized to its value at 25 nm spacer thickness. To model emission and collection, the rate into photon states of wavevector less than the numerical aperture of the microscope objective was calculated at a free-space wavelength of 550 nm. Multiplying calculated absorption and emission data generates the gray solid curve and blue dashed curve in Figure C-1 (b) for different batches. The curves show good agreement with measured results.

Appendix D: Fabrication of Plasmonic Crystals

In this section we provide an idea and initial attempt on fabricating plasmonic crystals like those described in chapter 5. The process flow of this method is shown in Figure D-1.

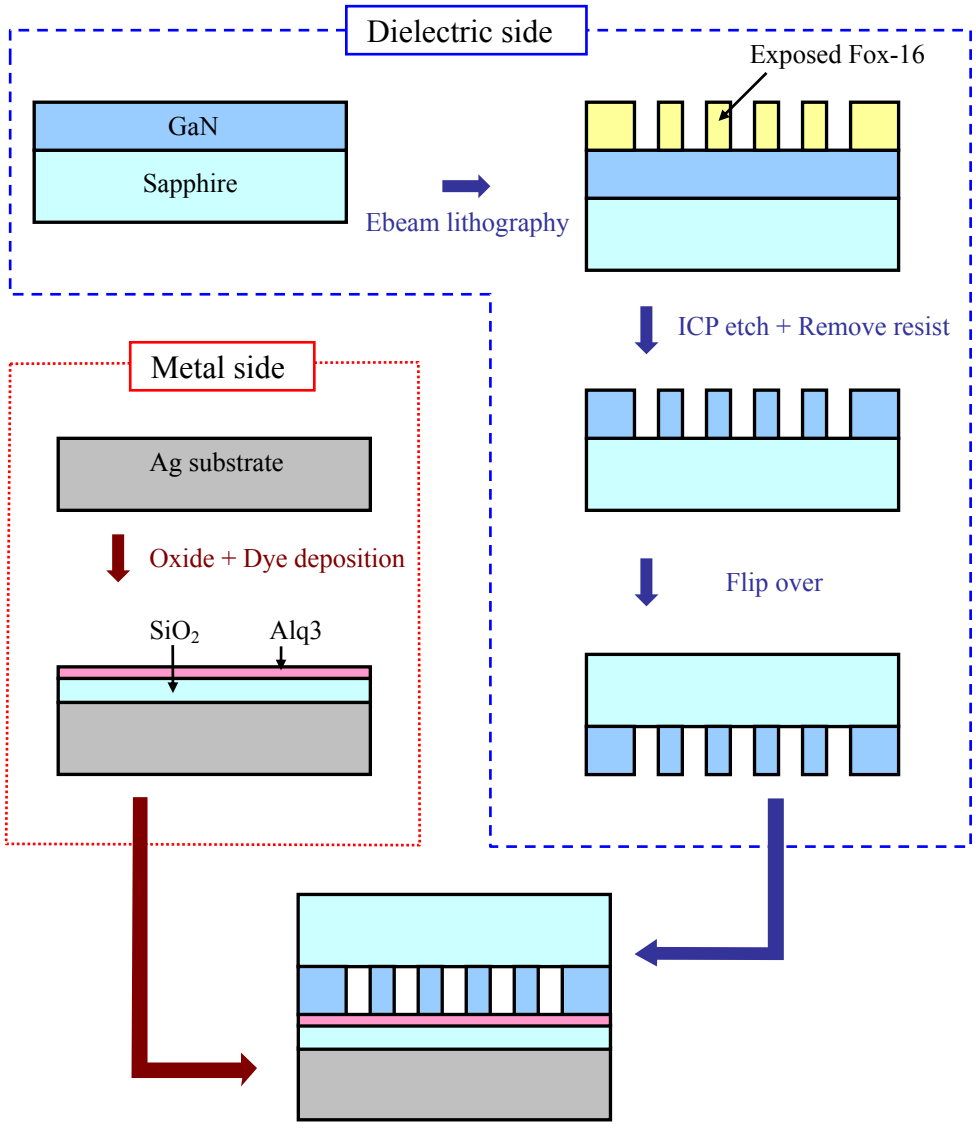

Fig. D-1: Proposed process flow for fabricating plasmonic crystal cavities.

In this method, the dielectric side was made of 3.5um thick GaN grown on a sapphire wafer purchased from University Wafers. This GaN wafer was first polished down to a GaN thickness of ~500nm. Then the photonic crystal pattern was defined with a 125 kV Ebeam lithography system on the GaN surface. A hydrogen silsesquioxane-based Ebeam resist XR-1541 by Dow Corning Co. was used, such that the area exposed to the electron beam was converted into an amorphous silicon oxide that serves as an etch mask in the subsequent inductively coupled plasma reactive ion etch. The unprotected area was etched with an Ar-Cl_2 based plasma in a reactive ion etch. Following the etch, the XR mask was removed in buffered oxide etch solution. SEM images of the fabricated dielectric rod array are shown in Figure D-2.

(a) (b)

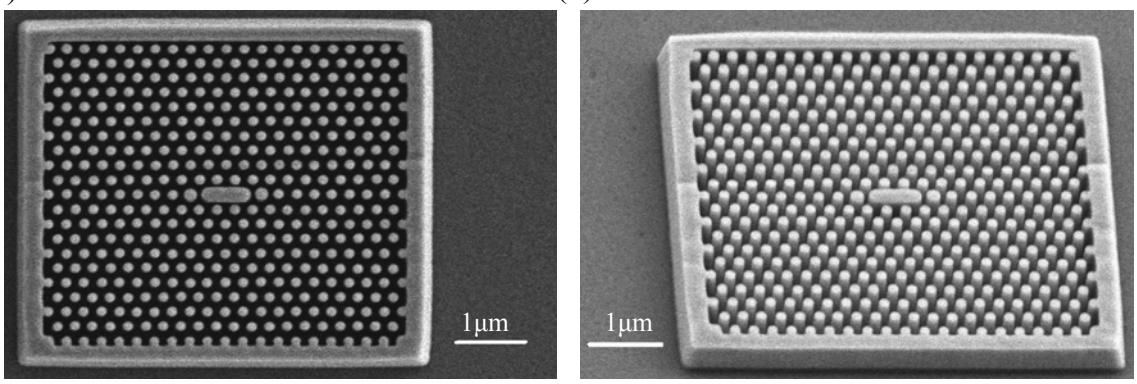

Fig. D-2: SEM images of the dielectric side of a plasmonic crystal made of GaN on sapphire including (a) a top-down view and (b) a 40 degree angled view.

To form the silver substrate comprising the metal side, we have tried to use both a

template tripped silver surface as introduced in Chapter 3 as well as a silver plate as shown in Appendix E. A 10nm layer of SiO_2 deposited onto the silver substrate and served as a dielectric spacer. The emitter layer was 8nm of Alq3 thermally evaporated on top of the SiO_2 spacer layer. However, combining these two parts with perfect contact remains challenging and requires further development.